VISUAL EXPERIENCE ENHANCED FEATURE SELECTIVITY IN PRIMARY VISUAL CORTEX

by

Mang Gao

A Dissertation

Submitted to the Faculty of Purdue University

In Partial Fulfillment of the Requirements for the degree of

Doctor of Philosophy

Department of Biological Sciences

West Lafayette, Indiana

May 2022

THE PURDUE UNIVERSITY GRADUATE SCHOOL

STATEMENT OF COMMITTEE APPROVAL

Dr. Alexander Chubykin, Chair

Department of Biological Sciences

Dr. Edward Bartlett

Department of Biological Sciences

Dr. Donald Ready

Department of Biological Sciences

Dr. Estuardo Robles

Department of Biological Sciences

Approved by:

Dr. Janice Evans

Dedicated to my dear parents, Jianguo Gao and Xiaohong Duan

ACKNOWLEDGMENTS

I would like to specially acknowledge and thank Dr. Alexander Chubykin, who is my advisor, for providing guidance, advice, resources, opportunities and other helps. He taught me a lot in neurophysiology, data analysis, computer programming, scientific writing, experiment techniques, and many others. Most importantly, he trusted me and my audacious projects with exceptional patience and continuously supported everything I needed. I would not be able to achieve any of the works I had done without him.

I would like to specially thank Dr. Edward Bartlett, Dr. Donald Ready, and Dr. Estuardo Robles, who are on my research committee. They generously shared their knowledge, opinions, and advice over the years, which greatly helped my works and was essential for my achievement.

I would like to thank Dr.Gong Chen, Dr. Sukbin Lim, Dr.Yu-Chen Chen, Yu Tang, Dr. Rachel Wu, Dr. Samuel Kissinger, and other collaborators. The collaboration with them expanded the scope of my works and led to new heights of accomplishments. I would like to thank Dr. Alexandr Pak. His thoughts and opinions greatly helped my work. He generously shared his open-source code, some of which was used for my works. I would like to thank Michael Zimmerman, who provided valuable comments and opinions that helped improve my publications.

I would like to thank Dr. Scout Pluta for providing the design of the mouse head-plate, which greatly reduced the difficulty of my work. He also provided important opinions on my works that helped me for improvements. I would like to thank Dr. Andy Schaber for providing the training on microscopy and the necessary help for imaging works.

I would like to thank Dr. Yuk Fai Leung and Dr. Daniel Suter, who introduced me to neuroscience and physiology. They were the first people who showed me how intriguing and exciting neuroscience is. I would not be pursuing research in neuroscience without them.

I would like to thank Benjamin Cryer and Edward Tourney, who provided valuable help with my experiments.

Finally, I would like to thank everyone who provided help and support during my graduate education. I would not be able to achieve the success that I had without them.

TABLE OF CONTENTS

LIST OF FIGURES

ABSTRACT

The primary visual cortex (V1) is a center in the visual pathway that receives the converging information and sends diverging information to multiple visual areas. It is essential for the normal functioning of the visual system. While processing the input from the outside world, it is also continually modified by the sensory experience. This thesis is dedicated to studying the plasticity in the visual cortex that is associated with experience and brain damage recovery. In this thesis, we discovered that the visual experience induces 5 Hz oscillations that recruit inhibition in V1, sharpening the feature selectivity. We have also demonstrated that gene therapy to convert astrocytes into neurons induces neuronal circuit plasticity and functional recovery in mouse V1 following ischemia.

CHAPTER 1. INTRODUCTION

1.1 The diversity of cell types and organization of mouse primary visual cortex

Primary visual cortex (V1) is the first area that receives thalamocortical input in the neocortex. It is inter-connected with both cortical and sub-cortical visual areas, acting as a center of the visual pathway (Figure 1.1A). The neurons in V1 can be grossly divided into excitatory neurons that are glutamatergic and inhibitory interneurons that are GABAergic. The excitatory neurons make up the ~80% of all neurons and the inhibitory interneurons make up about 20% of the population (Gabbott et al., 1986; Markram et al., 2004). Both excitatory neurons and interneurons can be divided into groups that differ in molecular expression profile, morphology, cellular property, laminar location, and functional roles in the circuits. Continuous efforts have been made to achieve a comprehensive and objective classification of the cortical neurons (DeFelipe and Farinas, 1992; Markram et al., 2004; Migliore and Shepherd, 2005; Petilla Interneuron Nomenclature et al., 2008; DeFelipe et al., 2013). In the last decade, with the development of the single-cell transcriptomic (Pollen et al., 2014; Zeisel et al., 2015), high-throughput morphology reconstruction (Kasthuri et al., 2015; Markram et al., 2015; Economo et al., 2016; Winnubst et al., 2019; Berg et al., 2021), the categorization of cortical neurons had achieved great progress (Tasic et al., 2016; Tasic et al., 2018; Yuste et al., 2020; Network, 2021). A cell-type database that includes the expression profile, morphology, and electrophysiological properties was established for mouse V1 (Tasic et al., 2016).

Although the cortical neurons are diverse, most of them can be divided into a small number of sub-classes (Harris and Shepherd, 2015; Zeng and Sanes, 2017; Matho et al., 2021). The majority of excitatory cells fall into five groups. Intratelencephalic (IT) neurons are commonly found in layer 2/3, layer 5, and layer 6. These thick-tufted neurons form cortical-cortical projections. Layer 4 excitatory neurons are the major thalamocortical input from the dorsal lateral geniculate nucleus (dLGN) in mouse V1. They are mostly pyramidal cells that have apical dendrites like IT cells in layer 2/3 and layer 5, except they usually do not have prominent dendritic arborization in layer 1(Scala et al., 2019). The pyramidal tract neurons (PT) are located in layer 5b, projecting to subcortical areas. The corticothalamic neurons (CT) are found in layer 6, projecting to the thalamus. The last group is the layer 6b subplate neurons. These neurons mostly

receive input from and project to V1 locally and in other cortical areas. They also receive relatively weak input from the thalamus and project to the higher-order thalamus (Zolnik et al., 2020).

The inhibitory interneurons in the neocortex can be divided into four distinct, largely non-overlapped types: Neuron-Derived Neurotrophic Factor (NDNF) expressing layer 1 interneurons, parvalbumin-expressing interneurons (PV), somatostatin-expressing interneurons (SOM) and vasoactive intestinal peptide expressing interneurons (VIP) (Gonchar et al., 2007; Poulin et al., 2016; Tasic et al., 2016; Tremblay et al., 2016). Each group can be further divided into sub-classes that are different in physiology and morphology properties. NDNF expressing interneurons are found in layer 1. Almost all neurons that can be found in layer 1 belong to this type of interneuron. They form unidirectional or mutual inhibitory connections with layer 2/3 interneurons. They are involved in the disinhibition of the distal dendrites of pyramidal cells. PV, SOM, and VIP cells are distributed across the whole span of the cortex layers except layer 1. They receive local inputs from excitatory cells and send inhibitory inputs to excitatory cells and interneurons of the same or different types. A basic microcircuit of excitatory cells and these three groups of cells was revealed by a study in acute brain slices using Cre-dependent optogenetics and single-cell RT-PCR (Pfeffer et al., 2013). In layer 2/3 and layer 5, the PV cells mostly provide somatic inhibition to each other and excitatory cells; the VIP cells almost only inhibit SOM cells; SOM cells inhibit PV and VIP interneurons and send both somatic and dendritic inhibitions to excitatory cells. In layer 4, SOM cells mostly inhibit the PV cells, and the PV cells inhibit excitatory cells, forming a disinhibiting circuit that acts as a gain control mechanism for V1 (Xu et al., 2013).

The various types of cortical neurons form an extremely complex network in V1. Although many attempts have been made to systematical characterize the connections between cortical cells in V1 (Thomson et al., 2002; Binzegger et al., 2004; Jiang et al., 2015), a complete connectivity map is still out of reach due to the technical difficulties and limitations (Barth et al., 2016; Zeng and Sanes, 2017). However, a general consensus on the neural circuit mediating visual information flow has been based on the strongest excitatory connections within V1 (Figure 1.1B) (Douglas and Martin, 2004; Harris and Mrsic-Flogel, 2013; Shepherd and Yamawaki, 2021).

Thalamocortical input from dLGN is primarily formed onto layer 4 pyramidal cells. From layer 4 pyramidal cells, the excitatory input is sent to layer 2/3 IT cells. Layer 2/3 IT cells form a strong recurrent network with mutual excitatory connections between them, which is the strongest type of connection in the neocortex. The information next travels from layer 2/3 to layer 5 IT cells,

while layer 5 IT cells also project to layer 2/3 IT cells, forming an inter-laminar loop. From IT cells, the excitatory information travels to Layer 6 CT cells and then goes back to thalamic nuclei, including the thalamic reticular nucleus and higher nuclei such as the lateral posterior nucleus (LP). Beyond these strong excitatory connections, there are many other connections in V1. Although these connections may be less abundant, they could have very important functional roles. For example, VIP interneurons mediate the locomotion-related gain modulation in V1 (Fu et al., 2014); layer 1 interneurons control the layer 2/3 Martinotti SST cells and therefore participate in visual learning via disinhibiting the distal dendrites of IT cells (Abs et al., 2018).

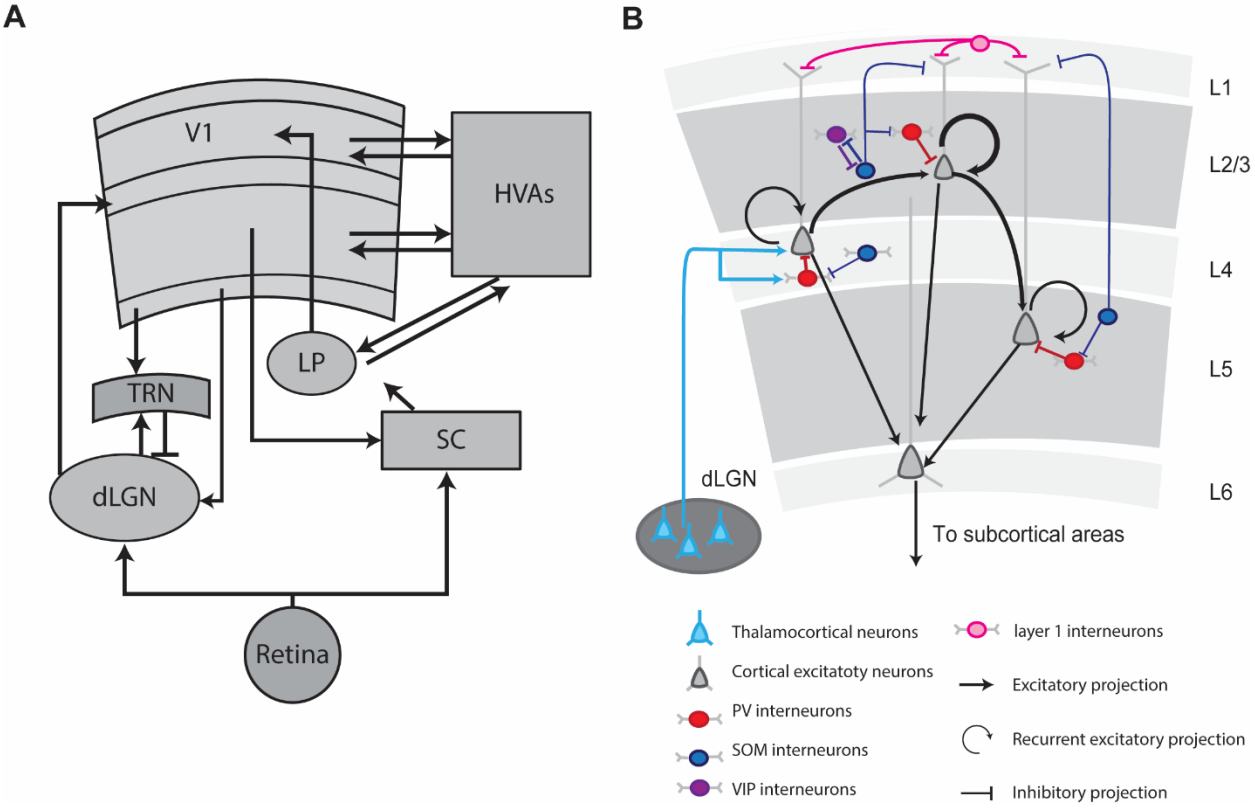

Figure 1.1 Connectivity maps of mouse visual system and V1. A. The mouse visual pathways. V1 receives inputs from the visual thalamus and higher visual areas. Projections of V1 terminate in multiple cortical and subcortical areas. Thalamus: dLGN, dorsal lateral geniculate nucleus; LP, Lateral posterior nucleus; TRN, thalamic reticular nucleus. Midbrain: SC, superior colliculus. Neocortex: V1, primary visual cortex; HVAs, higher-order visual areas (cortex). B. Major circuits in V1. The input from dLGN is mostly received at layer 4. The strongest inter-laminar connection goes through layer 4, layer 2/3, and layer 5. The corticothalamic projecting (CT) cells in deep layers receive the input from IT cells from all layers and project to subcortical areas. The recurrent connection is the strongest connection in V1. It can be found in all cortical layers and is particularly strong in layer 2/3. Interneurons in V1 are diverse in cell types and functions. They provide both dendritic/somatic inhibition and disinhibition.

1.2 Feature selectivity in the visual cortex

One of the most well-studied properties of V1 is feature selectivity. Although both retina and dLGN contain feature selective cells, their feature selectivity is not directly inherited by V1. Instead, this selectivity emerges at the cortical level. This phenomenon was first characterized 60 years ago in the cat's visual cortex (Hubel and Wiesel, 1962). The visual stimulus used at the time was a black bar that moved in different orientations. Neurons in V1 demonstrated a preference for the visual stimuli of specific orientations and moving directions. The feature selectivity of V1 is not limited to these two features. Several previous studies had revealed the V1 neurons could be selective to spatial frequency, temporal frequency, moving speed, motion coherence, etc. (De Valois et al., 1982; DeAngelis et al., 1993; Niell and Stryker, 2008; Gao et al., 2010; Palagina et al., 2017; Sit and Goard, 2020). With their feature selectivity, V1 neurons extract certain features from the visual input and send the filtered information with different visual features to higher visual areas for further processing (Sincich and Horton, 2005; Andermann et al., 2011; Glickfeld et al., 2013). This process is essential for the functioning of the visual system.

The circuitry computation that generates the selectivity has always been an interest of studies. The best-understood one is orientation selectivity. In the early study by Hubel and Wiesel (1962), the cortical neurons were divided into “simple cells” and “complex cells.” The elongated receptive field of simple cells acted as a linear filter and led to the selective orientational response (Figure 1.2A). The complex cells received the inputs from multiple simple cells and therefore had more complex tuning properties that were generated by non-linear computation. Although we now know that almost all cortical neurons are interconnected, and the majority are “complex” to a certain extent (Ringach et al., 2002; Priebe et al., 2004), the linear summation of the receptive field could largely explain the orientation selectivity, especially in layer 4 cells (Martinez et al., 2005). The intra-cortical connections also contribute to orientation selectivity. In primates and cats, neurons form columns that are orientationally specific, and the horizontal connections are far more common within the column than between the columns. In rodents, there are no orientation columns in V1. However, the horizontal connections in mouse V1 are biased to the neurons with similar orientation preferences (Figure 1.2C) (Ohki et al., 2005; Ko et al., 2011). Monosynaptic tracing from the layer 2-3 IT cells also confirmed that the presynaptic cells' tuning properties resemble the postsynaptic neurons (Wertz et al., 2015). The interneurons also contribute to the orientation selectivity of excitatory cells (Figure 1.2C and D). In rodents, the interneurons are less selective

for orientations. However, the un-tuned inhibitory input sharpens the tuning in excitatory cells at the level of individual synapses (Liu et al., 2011). The enhancement of suprathreshold tuning was also confirmed by optogenetic activation of parvalbumin-positive (PV) interneurons (Lee et al., 2012; Lee et al., 2014). Interestingly, the activation of somatostatin-positive (SST) interneurons did not change the orientation tuning.

The direction selectivity is closely associated with the orientation selectivity in V1. The preferred direction of cells is almost always orthogonal to their preferred orientation. This correlation may potentially be explained by the fact that the most efficient way to detect motion given the receptive fields of V1 neurons is the elongated receptive field (Carandini et al., 2005). A recent study directly recorded thalamocortical input from layer 4 in vivo using whole-cell recordings while optogenetically silencing the visual cortex. It revealed the synaptic mechanism that generates direction selectivity at layer 4 thalamocortical recipient (Lien and Scanziani, 2018). There are two types of dLGN inputs, a relative transient excitation that decays faster and a sustained excitation that decays slower. When a black-white alternating stimulus was displayed, the preferred spatial phases of these two types of dLGN inputs were different in direction-selective cells (Figure 1.2B). This phase difference between the two types of inputs results in an asymmetry of the phase input summations at the two sides of the spatial phase that has the strongest response. Thus, the temporal summation of these inputs from each spatial phase is stronger when the stimulus is moving in one direction than the opposite direction. This spatial-temporal asymmetry of the inputs results from the spatial-temporal profile of the dLGN cells rather than the direction selectivity of the dLGN cells. That is, the direction selectivity in layer 4 is computed by the thalamocortical recipient cells rather than inherited from the early visual pathway. The intracortical connection also contributes to the direction selectivity in V1. This is less well-understood in rodents. However, in mammals that have orientation columns, the cells that are selective to the same direction are located closer to each other and are more likely to be connected. Meanwhile, the cells between the two groups of cells that prefer the two opposite directions are usually not direction-selective, creating a discontinuity in the direction map (Ohki et al., 2005). The involvement of inhibition in direction selectivity is not completely clear. However, a study has shown that activating interneurons could improve the direction selectivity in V1 IT cells (Lee et al., 2012).

The mechanisms of other feature selectivities are less understood. However, recent studies suggest that interneurons are essential for these feature selectivities (Adesnik et al., 2012; Ayzenshtat et al., 2016; Adesnik, 2017; Millman et al., 2020). The development of genetically specific manipulation and recording methods may lead to the discovery of the mechanisms of the feature selectivities in the future.

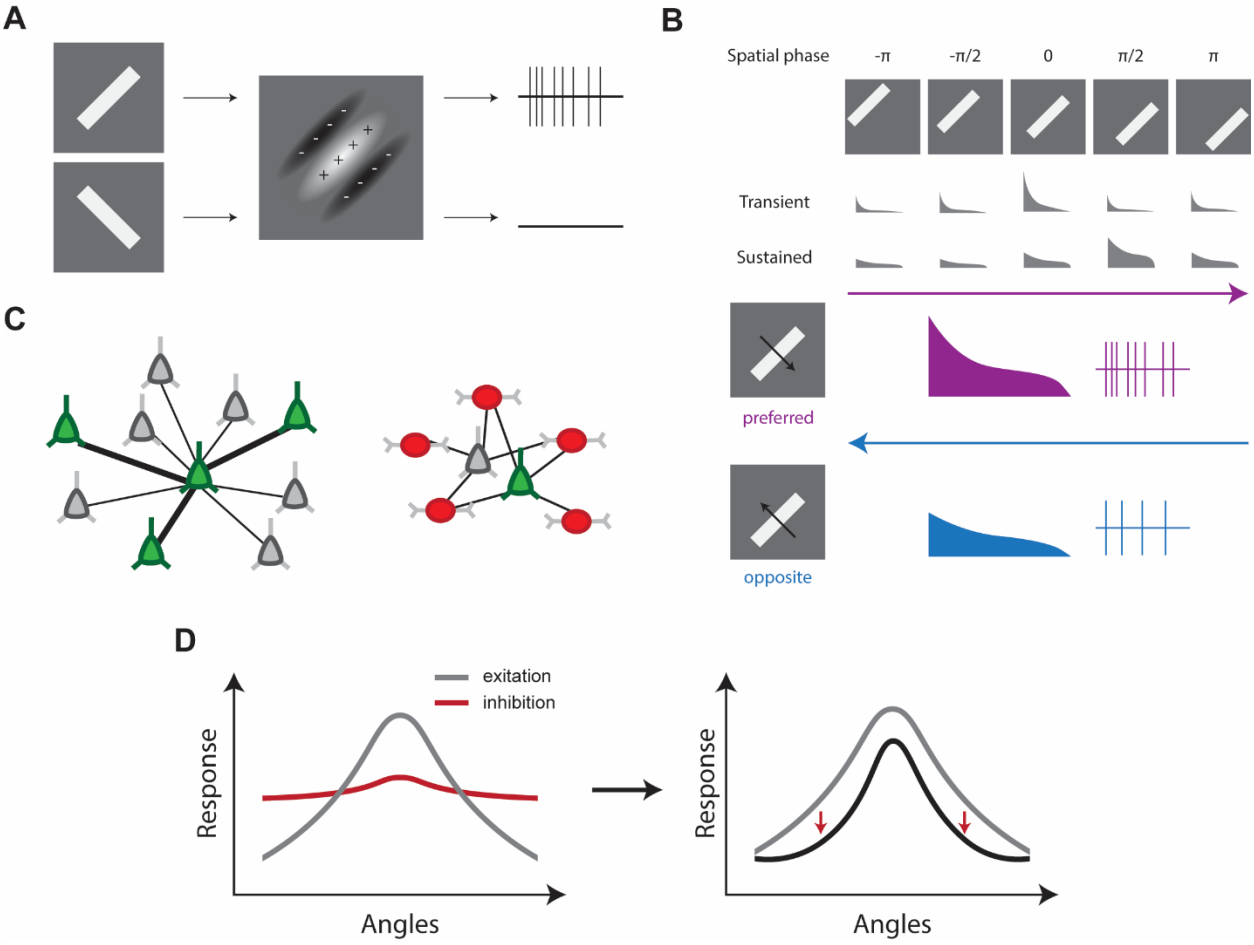

Figure 1.2 Basic mechanisms of orientation and direction selectivity in V1. A. The linear summation with elongated receptive fields generates an orientation selective response. B. The mechanism of direction selectivity in layer 4 thalamocortical recipients. In direction selective cells, there is an offset between the preferred spatial phases of the transient input and the sustained inputs. As a result, the temporal summation of the inputs at the preferred direction is stronger than in the opposite direction, generating more suprathreshold activity. C. Left, in rodent V1, the excitatory cells with similar orientation selectivity are more likely to form connections with each other. Green triangular cells represent the cells that have the same preference; grey triangular cells represent other cells. Right, the connections between excitatory cells and interneurons are less selective. Red oval cells represent inhibitory interneurons. D. Left, the excitation input is tuned, and the inhibitory input is much less tuned in rodent V1. Right, the untuned inhibition contributes to the sharpening of cell selectivity by increasing the preferred verse non-preferred response ratio.

1.3 Learning and plasticity in the visual cortex

While the visual cortex is constantly receiving the sensory inputs from the environment, it is also modified by the sensory experience even in adulthood. Perceptual learning associated changes in the visual cortex have been reported in numerous studies. The representations of the visual information in visual cortex neurons were often enhanced by the experience, usually shown as an increased feature selectivity. In a primate study (Schoups et al., 2001), the subject was trained to perform an orientation discrimination task. Neurons that were in the trained receptive field (trained) and outside the receptive field (naïve) were recorded before and after the training. Comparing trained units to the naïve, they found an increased tuning curve slope in the units with preferred orientations close to the trained orientation. The sharpening of the tuning property of these units led to an improved signal-to-noise ratio at the population level and a better neuronal discrimination performance. Similar discrimination tasks were also shown to sharpen the response profile of V4 neurons in monkeys with an increased response to the trained stimulus. Interestingly, similar neural selectivity improvement is not limited to simple features and early cortices. ITC, a higher-order visual area responsible for object recognition, was also reported to have improved selectivity to complex features following visual experience (Freedman et al., 2006).

In rodents, the repetitive exposure of the animal to square-reversing sinusoidal gratings stimulus was found to induce an increase in the amplitude of the local field potential (LFP) in V1 (Frenkel et al., 2006), which is termed stimulus-selective response potentiation (SRP). This form of plasticity was determined to occur in Layer 4 and requires NMDA receptors (Cooke and Bear, 2010; Cooke et al., 2015). Interestingly, sleep reconsolidation was found to be critical for the expression of SRP (Aton et al., 2014). The training with repetitive viewing of visual stimuli in a rewarded behavior task was also found to enhance the feature selectivity in L2/3 cells (Poort et al., 2015). The increase in the selectivity was significant both in the percentage of the selective cells and the average selectivity of the population. This effect was not only specific to the stimulus that predicted the delivery of the rewards but also presented for the non-rewarded stimulus. The improvement of the feature selectivity resulted from the suppression of the non-preferred response, while the calcium response for the preferred stimulus was not significantly increased (Poort et al., 2022). This observation was distinct from the modulation caused by attention shifting. The cell-type specificity of visual learning-induced selectivity improvement was also investigated in recent studies (Khan et al., 2018; Poort et al., 2022). The improvement was great in excitatory neurons

and PV cells but relatively weak in SOM cells. The changes in the response of VIP neurons were minimal.

Another form of experience-dependent changes in visual representation was found by using delayed reward delivery with visual cues. After the training with reward paired visual stimulus, V1 neurons were able to report the timing of the reward with sustained firing, sustained suppression, or a second peak of the firing at the time points of the expected reward deliveries. These visual response patterns that emerged with the training required input from the cholinergic system (Chubykin et al., 2013; Liu et al., 2015). The reward timing activity in V1 was also found to be accompanied by synchronized population activity in 4-8 Hz frequency range (Zold and Hussain Shuler, 2015; Levy et al., 2017). Interneurons were also found to be involved in the reward timing activity (Monk et al., 2020).

Modulations from higher-order areas were also found to be involved in the learning in V1. The top-down activity from RSC to V1 was found to be increased with visual experience, especially when paired with an avoidance task. Meanwhile, the percentage of local layer 2/3 cells that were responsive to the visual stimulus decreased with the experience (Makino and Komiyama, 2015).

Although the learning-related modulations on neuronal representations in the visual cortex were extensively studied, our understandings of the circuitry and synaptic level mechanisms are still limited. Previous studies have demonstrated that SRP requires NMDA receptors (Cooke and Bear, 2010; Cooke et al., 2015). Neuromodulation was also found to be important for visual learning (Chubykin et al., 2013; Kissinger et al., 2018). The increased L5 excitatory neuron to L4 fast-spiking neuronal synaptic connections were found in the visually experienced mice (Kissinger et al., 2020). Studies also showed that the visual experience could induce 4-8 Hz oscillations in the visual cortex in an awake animal (Zold and Hussain Shuler, 2015; Levy et al., 2017; Kissinger et al., 2018; Kissinger et al., 2020). Such oscillations could facilitate input selection via spike-timing-dependent plasticity (Buzsaki and Draguhn, 2004). However, the direct in vivo evidence for the certain types of plasticity involved in the visual learning paradigms is still scarce. It is unknown how various types of visual experience lead to the different types of synaptic plasticity. It is also largely unknown how the cortical circuits and specific cell types contribute to the induction and maintenance of the LTP and LTD that occur during learning. Due to the difficulty of the direct cellular level measurement and manipulation in vivo, it is especially challenging to

answer these questions. However, the recent technological developments have made such studies more feasible.

1.4 Reference

Abs E, Poorthuis RB, Apelblat D, Muhammad K, Pardi MB, Enke L, Kushinsky D, Pu DL, Eizinger MF, Conzelmann KK, Spiegel I, Letzkus JJ (2018) Learning-Related Plasticity in Dendrite-Targeting Layer 1 Interneurons. Neuron 100:684-699 e686.

Adesnik H (2017) Synaptic Mechanisms of Feature Coding in the Visual Cortex of Awake Mice. Neuron 95:1147-1159 e1144.

Adesnik H, Bruns W, Taniguchi H, Huang ZJ, Scanziani M (2012) A neural circuit for spatial summation in visual cortex. Nature 490:226-231.

Andermann ML, Kerlin AM, Roumis DK, Glickfeld LL, Reid RC (2011) Functional specialization of mouse higher visual cortical areas. Neuron 72:1025-1039.

Aton SJ, Suresh A, Broussard C, Frank MG (2014) Sleep promotes cortical response potentiation following visual experience. Sleep 37:1163-1170.

Ayzenshtat I, Karnani MM, Jackson J, Yuste R (2016) Cortical Control of Spatial Resolution by VIP+ Interneurons. J Neurosci 36:11498-11509.

Barth L, Burkhalter A, Callaway EM, Connors BW, Cauli B, DeFelipe J, Feldmeyer D, Freund T, Kawaguchi Y, Kisvarday Z, Kubota Y, McBain C, Oberlaender M, Rossier J, Rudy B, Staiger JF, Somogyi P, Tamas G, Yuste R (2016) Comment on "Principles of connectivity among morphologically defined cell types in adult neocortex". Science 353:1108.

Berg J et al. (2021) Human neocortical expansion involves glutamatergic neuron diversification. Nature 598:151-158.

Binzegger T, Douglas RJ, Martin KA (2004) A quantitative map of the circuit of cat primary visual cortex. J Neurosci 24:8441-8453.

Buzsaki G, Draguhn A (2004) Neuronal oscillations in cortical networks. Science 304:1926-1929.

Carandini M, Demb JB, Mante V, Tolhurst DJ, Dan Y, Olshausen BA, Gallant JL, Rust NC (2005) Do we know what the early visual system does? J Neurosci 25:10577-10597.

Chubykin AA, Roach EB, Bear MF, Shuler MG (2013) A cholinergic mechanism for reward timing within primary visual cortex. Neuron 77:723-735.

Cooke SF, Bear MF (2010) Visual experience induces long-term potentiation in the primary visual cortex. J Neurosci 30:16304-16313.

Cooke SF, Komorowski RW, Kaplan ES, Gavornik JP, Bear MF (2015) Visual recognition memory, manifested as long-term habituation, requires synaptic plasticity in V1. Nat Neurosci 18:262-271.

De Valois RL, Albrecht DG, Thorell LG (1982) Spatial frequency selectivity of cells in macaque visual cortex. Vision Res 22:545-559.

DeAngelis GC, Ohzawa I, Freeman RD (1993) Spatiotemporal organization of simple-cell receptive fields in the cat's striate cortex. II. Linearity of temporal and spatial summation. J Neurophysiol 69:1118-1135.

DeFelipe J, Farinas I (1992) The pyramidal neuron of the cerebral cortex: morphological and chemical characteristics of the synaptic inputs. Prog Neurobiol 39:563-607.

DeFelipe J et al. (2013) New insights into the classification and nomenclature of cortical GABAergic interneurons. Nat Rev Neurosci 14:202-216.

Douglas RJ, Martin KA (2004) Neuronal circuits of the neocortex. Annu Rev Neurosci 27:419-451.
Economo MN, Clack NG, Lavis LD, Gerfen CR, Svoboda K, Myers EW, Chandrashekar J (2016) A platform for brain-wide imaging and reconstruction of individual neurons. Elife 5:e10566.
Freedman DJ, Riesenhuber M, Poggio T, Miller EK (2006) Experience-dependent sharpening of visual shape selectivity in inferior temporal cortex. Cereb Cortex 16:1631-1644.
Frenkel MY, Sawtell NB, Diogo AC, Yoon B, Neve RL, Bear MF (2006) Instructive effect of visual experience in mouse visual cortex. Neuron 51:339-349.
Fu Y, Tucciarone JM, Espinosa JS, Sheng N, Darcy DP, Nicoll RA, Huang ZJ, Stryker MP (2014) A cortical circuit for gain control by behavioral state. Cell 156:1139-1152.
Gabbott PL, Somogyi J, Stewart MG, Hamori J (1986) A quantitative investigation of the neuronal composition of the rat dorsal lateral geniculate nucleus using GABA-immunocytochemistry. Neuroscience 19:101-111.
Gao E, DeAngelis GC, Burkhalter A (2010) Parallel input channels to mouse primary visual cortex. J Neurosci 30:5912-5926.
Glickfeld LL, Andermann ML, Bonin V, Reid RC (2013) Cortico-cortical projections in mouse visual cortex are functionally target specific. Nat Neurosci 16:219-226.
Gonchar Y, Wang Q, Burkhalter A (2007) Multiple Distinct Subtypes of GABAergic Neurons in Mouse Visual Cortex Identified by Triple Immunostaining. Frontiers in Neuroanatomy 1:3.
Harris KD, Mrsic-Flogel TD (2013) Cortical connectivity and sensory coding. Nature 503:51-58.
Harris KD, Shepherd GM (2015) The neocortical circuit: themes and variations. Nat Neurosci 18:170-181.
Hubel DH, Wiesel TN (1962) Receptive fields, binocular interaction and functional architecture in the cat's visual cortex. J Physiol 160:106-154.
Jiang X, Shen S, Cadwell CR, Berens P, Sinz F, Ecker AS, Patel S, Tolias AS (2015) Principles of connectivity among morphologically defined cell types in adult neocortex. Science 350:aac9462.
Kasthuri N et al. (2015) Saturated Reconstruction of a Volume of Neocortex. Cell 162:648-661.
Khan AG, Poort J, Chadwick A, Blot A, Sahani M, Mrsic-Flogel TD, Hofer SB (2018) Distinct learning-induced changes in stimulus selectivity and interactions of GABAergic interneuron classes in visual cortex. Nat Neurosci 21:851-859.
Kissinger ST, Pak A, Tang Y, Masmanidis SC, Chubykin AA (2018) Oscillatory Encoding of Visual Stimulus Familiarity. J Neurosci 38:6223-6240.
Kissinger ST, Wu Q, Quinn CJ, Anderson AK, Pak A, Chubykin AA (2020) Visual Experience-Dependent Oscillations and Underlying Circuit Connectivity Changes Are Impaired in Fmr1 KO Mice. Cell Rep 31:107486.
Ko H, Hofer SB, Pichler B, Buchanan KA, Sjostrom PJ, Mrsic-Flogel TD (2011) Functional specificity of local synaptic connections in neocortical networks. Nature 473:87-91.
Lee SH, Kwan AC, Dan Y (2014) Interneuron subtypes and orientation tuning. Nature 508:E1-2.
Lee SH, Kwan AC, Zhang S, Phoumthipphavong V, Flannery JG, Masmanidis SC, Taniguchi H, Huang ZJ, Zhang F, Boyden ES, Deisseroth K, Dan Y (2012) Activation of specific interneurons improves V1 feature selectivity and visual perception. Nature 488:379-383.
Levy JM, Zold CL, Namboodiri VMK, Hussain Shuler MG (2017) The Timing of Reward-Seeking Action Tracks Visually Cued Theta Oscillations in Primary Visual Cortex. J Neurosci 37:10408-10420.

Lien AD, Scanziani M (2018) Cortical direction selectivity emerges at convergence of thalamic synapses. Nature 558:80-86.
Liu BH, Li YT, Ma WP, Pan CJ, Zhang LI, Tao HW (2011) Broad inhibition sharpens orientation selectivity by expanding input dynamic range in mouse simple cells. Neuron 71:542-554.
Liu CH, Coleman JE, Davoudi H, Zhang K, Hussain Shuler MG (2015) Selective activation of a putative reinforcement signal conditions cued interval timing in primary visual cortex. Curr Biol 25:1551-1561.
Makino H, Komiyama T (2015) Learning enhances the relative impact of top-down processing in the visual cortex. Nat Neurosci 18:1116-1122.
Markram H, Toledo-Rodriguez M, Wang Y, Gupta A, Silberberg G, Wu C (2004) Interneurons of the neocortical inhibitory system. Nat Rev Neurosci 5:793-807.
Markram H et al. (2015) Reconstruction and Simulation of Neocortical Microcircuitry. Cell 163:456-492.
Martinez LM, Wang Q, Reid RC, Pillai C, Alonso JM, Sommer FT, Hirsch JA (2005) Receptive field structure varies with layer in the primary visual cortex. Nat Neurosci 8:372-379.
Matho KS et al. (2021) Genetic dissection of the glutamatergic neuron system in cerebral cortex. Nature 598:182-187.
Migliore M, Shepherd GM (2005) Opinion: an integrated approach to classifying neuronal phenotypes. Nat Rev Neurosci 6:810-818.
Millman DJ, Ocker GK, Caldejon S, Kato I, Larkin JD, Lee EK, Luviano J, Nayan C, Nguyen TV, North K, Seid S, White C, Lecoq J, Reid C, Buice MA, de Vries SE (2020) VIP interneurons in mouse primary visual cortex selectively enhance responses to weak but specific stimuli. Elife 9.
Monk KJ, Allard S, Hussain Shuler MG (2020) Reward Timing and Its Expression by Inhibitory Interneurons in the Mouse Primary Visual Cortex. Cereb Cortex 30:4662-4676.
Network BICC (2021) A multimodal cell census and atlas of the mammalian primary motor cortex. Nature 598:86-102.
Niell CM, Stryker MP (2008) Highly selective receptive fields in mouse visual cortex. J Neurosci 28:7520-7536.
Ohki K, Chung S, Ch'ng YH, Kara P, Reid RC (2005) Functional imaging with cellular resolution reveals precise micro-architecture in visual cortex. Nature 433:597-603.
Palagina G, Meyer JF, Smirnakis SM (2017) Complex Visual Motion Representation in Mouse Area V1. J Neurosci 37:164-183.
Petilla Interneuron Nomenclature G et al. (2008) Petilla terminology: nomenclature of features of GABAergic interneurons of the cerebral cortex. Nat Rev Neurosci 9:557-568.
Pfeffer CK, Xue M, He M, Huang ZJ, Scanziani M (2013) Inhibition of inhibition in visual cortex: the logic of connections between molecularly distinct interneurons. Nat Neurosci 16:1068-1076.
Pollen AA et al. (2014) Low-coverage single-cell mRNA sequencing reveals cellular heterogeneity and activated signaling pathways in developing cerebral cortex. Nat Biotechnol 32:1053-1058.
Poort J, Wilmes KA, Blot A, Chadwick A, Sahani M, Clopath C, Mrsic-Flogel TD, Hofer SB, Khan AG (2022) Learning and attention increase visual response selectivity through distinct mechanisms. Neuron 110:686-697 e686.

Poort J, Khan AG, Pachitariu M, Nemri A, Orsolic I, Krupic J, Bauza M, Sahani M, Keller GB, Mrsic-Flogel TD, Hofer SB (2015) Learning Enhances Sensory and Multiple Non-sensory Representations in Primary Visual Cortex. Neuron 86:1478-1490.

Poulin J-F, Tasic B, Hjerling-Leffler J, Trimarchi JM, Awatramani R (2016) Disentangling neural cell diversity using single-cell transcriptomics. Nat Neurosci 19:1131-1141.

Priebe NJ, Mechler F, Carandini M, Ferster D (2004) The contribution of spike threshold to the dichotomy of cortical simple and complex cells. Nat Neurosci 7:1113-1122.

Ringach DL, Shapley RM, Hawken MJ (2002) Orientation selectivity in macaque V1: diversity and laminar dependence. J Neurosci 22:5639-5651.

Scala F, Kobak D, Shan S, Bernaerts Y, Laturnus S, Cadwell CR, Hartmanis L, Froudarakis E, Castro JR, Tan ZH, Papadopoulos S, Patel SS, Sandberg R, Berens P, Jiang X, Tolias AS (2019) Layer 4 of mouse neocortex differs in cell types and circuit organization between sensory areas. Nat Commun 10:4174.

Schoups A, Vogels R, Qian N, Orban G (2001) Practising orientation identification improves orientation coding in V1 neurons. Nature 412:549-553.

Shepherd GMG, Yamawaki N (2021) Untangling the cortico-thalamo-cortical loop: cellular pieces of a knotty circuit puzzle. Nat Rev Neurosci 22:389-406.

Sincich LC, Horton JC (2005) The circuitry of V1 and V2: integration of color, form, and motion. Annu Rev Neurosci 28:303-326.

Sit KK, Goard MJ (2020) Distributed and retinotopically asymmetric processing of coherent motion in mouse visual cortex. Nat Commun 11:3565.

Tasic B et al. (2016) Adult mouse cortical cell taxonomy revealed by single cell transcriptomics. Nat Neurosci 19:335-346.

Tasic B et al. (2018) Shared and distinct transcriptomic cell types across neocortical areas. Nature 563:72-78.

Thomson AM, West DC, Wang Y, Bannister AP (2002) Synaptic connections and small circuits involving excitatory and inhibitory neurons in layers 2-5 of adult rat and cat neocortex: triple intracellular recordings and biocytin labelling in vitro. Cereb Cortex 12:936-953.

Tremblay R, Lee S, Rudy B (2016) GABAergic Interneurons in the Neocortex: From Cellular Properties to Circuits. Neuron 91:260-292.

Wertz A, Trenholm S, Yonehara K, Hillier D, Raics Z, Leinweber M, Szalay G, Ghanem A, Keller G, Rozsa B, Conzelmann KK, Roska B (2015) PRESYNAPTIC NETWORKS. Single-cell-initiated monosynaptic tracing reveals layer-specific cortical network modules. Science 349:70-74.

Winnubst J et al. (2019) Reconstruction of 1,000 Projection Neurons Reveals New Cell Types and Organization of Long-Range Connectivity in the Mouse Brain. Cell 179:268-281 e213.

Xu H, Jeong HY, Tremblay R, Rudy B (2013) Neocortical somatostatin-expressing GABAergic interneurons disinhibit the thalamorecipient layer 4. Neuron 77:155-167.

Yuste R et al. (2020) A community-based transcriptomics classification and nomenclature of neocortical cell types. Nat Neurosci 23:1456-1468.

Zeisel A, Munoz-Manchado AB, Codeluppi S, Lonnerberg P, La Manno G, Jureus A, Marques S, Munguba H, He L, Betsholtz C, Rolny C, Castelo-Branco G, Hjerling-Leffler J, Linnarsson S (2015) Brain structure. Cell types in the mouse cortex and hippocampus revealed by single-cell RNA-seq. Science 347:1138-1142.

Zeng H, Sanes JR (2017) Neuronal cell-type classification: challenges, opportunities and the path forward. Nat Rev Neurosci 18:530-546.

Zold CL, Hussain Shuler MG (2015) Theta Oscillations in Visual Cortex Emerge with Experience to Convey Expected Reward Time and Experienced Reward Rate. J Neurosci 35:9603-9614.

Zolnik TA, Ledderose J, Toumazou M, Trimbuch T, Oram T, Rosenmund C, Eickholt BJ, Sachdev RNS, Larkum ME (2020) Layer 6b Is Driven by Intracortical Long-Range Projection Neurons. Cell Rep 30:3492-3505 e3495.

CHAPTER 2. VISUAL FAMILIARITY INDUCED 5-HZ OSCILLATIONS AND IMPROVED ORIENTATION AND DIRECTION SELECTIVITIES IN V1

Adopted from: Gao M, Lim S, Chubykin AA. Visual Familiarity Induced 5-Hz Oscillations and Improved Orientation and Direction Selectivities in V1. J Neurosci. 2021 Mar 24;41(12):2656-2667. doi: 10.1523/JNEUROSCI.1337-20.2021. Epub 2021 Feb 9. PMID: 33563727; PMCID: PMC8018737.

2.1 Abstract

Neural oscillations play critical roles in information processing, communication between brain areas, learning, and memory. We have recently discovered that familiar visual stimuli can robustly induce 5-Hz oscillations in the primary visual cortex (V1) of awake mice after the visual experience. To gain more mechanistic insight into this phenomenon, we used in vivo patch-clamp recordings to monitor the subthreshold activity of individual neurons during these oscillations. We analyzed the visual tuning properties of V1 neurons in naive and experienced mice to assess the effect of visual experience on the orientation and direction selectivity. Using optogenetic stimulation through the patch pipette in vivo, we measured the synaptic strength of specific intracortical and thalamocortical projections in vivo in the visual cortex before and after the visual experience. We found 5-Hz oscillations in membrane potential (Vm) and firing rates evoked in single neurons in response to the familiar stimulus, consistent with previous studies. Following the visual experience, the average firing rates of visual responses were reduced while the orientation and direction selectivities were increased. Light-evoked EPSCs were significantly increased for layer 5 (L5) projections to other layers of V1 after the visual experience, while the thalamocortical synaptic strength was decreased. In addition, we developed a computational model that could reproduce 5-Hz oscillations with enhanced neuronal selectivity following synaptic plasticity within the recurrent network and decreased feedforward input.

2.2 Introduction

Neural oscillations at around 5 Hz have been observed in the neocortex in both rodents and primates. These oscillations are involved in a variety of cognitive functions. In the auditory cortex, they provide temporal windows for processing syllables (Luo and Poeppel, 2007; Peelle et al.,

2013; Fuentemilla et al., 2014). These oscillations coordinate the precuneus and medial prefrontal cortex with the medial temporal lobe during autobiographical events retrieval (Fuentemilla et al., 2014). In the visual cortex, oscillations at around 5 Hz have been observed during learning in awake animals. In primates, 4- to 8-Hz phase-locked single-unit activity was present during visual working memory tasks within V4 (Lee et al., 2005). Five-Hertz phase-locked γ synchronization has been shown to correlate with short-term memory capacity (Sauseng et al., 2009). Three- to 9-Hz phase synchrony of V4 and the lateral prefrontal cortex was shown to be predictive of the behavioral performance (Liebe et al., 2012). In rodents, 4- to 8-Hz oscillations in the primary visual cortex (V1) were shown to predict the timing of a visually cued reward (Zold and Hussain Shuler, 2015; Levy et al., 2017). In contrast to reward prediction, 3- to 5-Hz oscillations have also been reported to reduce the visual responses recorded in mouse V1 (Einstein et al., 2017). We recently discovered that familiar visual stimuli could robustly induce 4- to 8-Hz oscillations in V1 of mice that have undergone the visual experience (Kissinger et al., 2018). These familiarity-triggered oscillations were not driven by the temporal modulation of the stimuli and could be induced by a static stimulus. These studies suggest that oscillations in the visual cortex may play vital roles in visual learning and information processing. However, the exact physiological function of such oscillations in V1 and their underlying mechanisms remain unclear.

To dissect the role of 5-Hz oscillations in experience-dependent plasticity in V1 and gain more mechanistic insight into how the oscillations modify visual responses at the cellular level, we performed in vivo patch-clamp recordings in naive and experienced mice. We discovered that oscillations of the membrane potential (Vm) at around 5 Hz, and bursts of action potentials (APs), were evoked in single neurons in response to the familiar stimulus after the visual experience along with a decreased stimulus-evoked firing. To test whether the selectivity of V1 neurons was modulated, we recorded their responses to 12 directions of drifting sinusoidal gratings and measured both orientation selectivity (OS) and direction selectivity (DS). Although the firing rates of visual responses to all directions and orientations of sinusoidal drifting gratings were reduced, the OS index (OSI) and DS index (DSI) were increased. To assess the synaptic strength changes resulting from the visual experience, we used optogenetic measurements through the patch pipette in vivo to measure the synaptic strength of the thalamocortical and intracortical projections in naive mice and experienced mice. In the experienced mice, light-evoked EPSCs were significantly

increased for the intracortical projections from layer 5 (L5) to other layers of V1, while the strength of the thalamocortical synapses was decreased. Finally, we developed a computational recurrent network model describing how synaptic plasticity observed experimentally can account for the effects of visual experience on stimulus selectivity and dynamic properties.

2.3 Materials and Methods

2.3.1 Animals

All animal use was approved by the Purdue University animal care and use committee. All mice were housed in a 12/12 h light/dark cycle with full access to food and water. The mice used were: C57BL/6 (The Jackson Laboratory), Thy1-ChR2-YFP (B6.Cg-Tg(Thy1-COP4/EYFP)18Gfng/J, The Jackson Laboratory), Vglut2-ChR2-YFP(C57BL/6-Tg(Slc17a6-COP4*H134R/EYFP)2Oki/J, The Jackson Laboratory). All mice used in experiments were at postnatal days 58–62. A total of 76 mice were used, including 36 male and 40 female mice.

2.3.2 Surgical procedure

At postnatal day 53, age matched mice were selected for head-plate implantation. Anesthesia was induced by 5% isoflurane in air and maintained at 1.5% isoflurane during surgery. Animals were head-fixed in a motorized stereotaxic apparatus (Neurostar). The surgery area was shaved and sterilized with ethanol. Ophthalmic ointment was applied to the eyes. A custom-designed head-plate was fixed to the skull with adhesive cement (C&B Metabond). The recording site (from λ: anteroposterior 0.3 mm, mediolateral 3.0 mm) was marked and covered by Kwik-Cast Silicone Elastomer. Before recording, a 0.04 mm^2 square craniotomy window was made and filled with artificial CSF (ACSF; 1.25 mm NaH_2PO_4, 26 mm $NaHCO_3$, 10 mm dextrose, 124 mm NaCl, 1 mm $CaCl_2$, 0.8 mm $MgCL_2$, and 3.5 mm KCl). For recordings in awake mice, mice recovered in the air for 30 min after isoflurane removal. For recordings in anesthetized mice, mice were kept anesthetized with intraperitoneally injected ketamine (100 mg/kg)/xylazine (16 mg/kg).

2.3.3 Perfusion and histology

Mice were anesthetized with intraperitoneally injected ketamine (100 mg/kg)/xylazine (16 mg/kg). They were transcardially perfused with 1× Phosphate-buffered saline (PBS) and followed by 4% paraformaldehyde (PFA). The brain was extracted and placed in 4% PFA for 20 h before slicing. The fixed brain was sliced into 50-μm coronal sections with a vibratome (TPI 1000 Plus). The images of brain sections were acquired with a LSM 710 confocal microscope and a 20×/1.0 NA lens (Zeiss, Plan-Apochromat) in tile scan mode.

2.3.4 Electrophysiology

In vivo patch-clamp recordings were performed in awake head-fixed mice. Patch pipettes (filamented borosilicate glass (BF150-86-10, Sutter Instrument) of 4–7 MΩ were pulled (P-97, Suter Instrument) and filled with internal solution (130 mm potassium D-gluconate, 5 mm KCl, 2 mm MgCl2, 0.3 mm NaGTP, 10 mm HEPES, and 0.6 mm EGTA). Electrophysiological recordings were acquired with an amplifier (Multiclamp 700B, Molecular Devices) and a digitizer (Digitata, 1550, Molecular Devices). Acquired data were collected using Clampex (Molecular Devices) with a 10,000-Hz low-pass filter. Blind patch-clamp recordings were performed with the assistance of an open-source software, Autopatcher (Wu et al., 2016; Wu and Chubykin, 2017). Cells with access resistance >60 MΩ were excluded. Membrane capacitance was corrected and compensated once a steady patch was formed.

2.3.5 Optogenetic stimulation

A blue laser (Opto Engine, 100 mW, 473 nm) was used as the light source for optogenetic stimulation. For all optogenetic experiments, Optopatcher (AM System; Katz et al., 2013) was used to replace the standard pipette holder. The light was delivered with a custom cut and polished optical fiber (Thorlabs, 0.39 NA TECS hard-clad, multimode, step-index fibers, FT200EMT). The optical fiber was inserted into a glass pipette within 1 mm from the pipette tip and was located coaxially to the pipette. A 2-mW laser power (measured at the internal solution filled pipette tip) was used for all experiments. The laser output power was calibrated before and after experiments to make sure the same power was used for all recordings.

2.3.6 Visual stimulation

Visual stimulation was generated and controlled by custom python scripts using the open-source PsychoPy package. Visual stimulation was presented on a γ calibrated LCD monitor. The gray background that was presented before and after the stimuli had the same luminance as the stimuli. A sinusoidal grating stimulus (200 ms, 0.04 cycle/°, 2 Hz) was used for training and recording. For orientation and direction tuning recordings, the grating stimulus was rotated in 30° steps to create the stimuli with 12 drifting directions. All stimuli were presented at 100% contrast.

2.3.7 Data analysis

For the analysis of Vm, APs were removed from raw traces with a 12.5-ms median filter. The Vm power spectra over frequencies were computed with Fast Fourier transform. The magnitudes of frequency bands were computed using bandpass filters on the spike-removed traces. The time-frequency analysis was computed with complex wavelet convolution (Cohen, 2014). A total of 40 frequencies across a logarithmic range from 2 to 80 Hz and 3 to 10 cycles of the wavelet were used. The coherence of frequency bands was computed with the same complex wavelet convolution method.

To detect 5-Hz Vm oscillation, we took the traces from the stimulus onset to 0.5 s after the onset as visual responses, and the traces from 4.5 to 5 s after the stimulus onset as the baseline. The trials that the visual response had >10 times 4- to 7-Hz power of the averaged baseline was determined as oscillation trials. We also manually inspected all trials to ensure the detection was correct (Einstein et al., 2017).

To detect APs, two smoothed traces were generated by convolving the raw trace with a Hanning window of 0.5 or 500 ms, respectively. The coarsely smoothed trace was subtracted from the finely smoothed trace to remove the Vm fluctuation for spike detection. The times of the peaks exceeding 15 mV were detected as the time of APs. Peristimulus time histograms (PSTHs) were computed from AP times with a 10-ms bin size. The PSTH was convolved with a 200-ms Gaussian window with 40-ms σ and normalized for each cell to calculate the normalized firing rate. The APs fired during 50–250 ms after the stimulus onset were considered visual response for 200-ms stimulus. The APs fired from 50 to 550 ms after the stimulus onset were considered visual response for 500-ms stimulus. To compute the OSI and DSI, we randomly split the trials into two halves.

The preferred direction was computed from the one-half of the trials. The preferred direction was used together with the other half of the trials to compute the OSI and DSI. The OSI and DSI were computed as follows:

$$OSI = \frac{R_{pref} - R_{orth}}{R_{pref} + R_{orth}}$$

$$DSI = \frac{R_{pref} - R_{opp}}{R_{pref} + R_{opp}}$$

where R_{pref} is the mean firing rate of the response to the preferred direction, R_{orth} is the mean firing rate of the response to the orthogonal direction, R_{opp} is the mean firing rate of the response to the opposite direction. This procedure was repeated 2000 times to generate the averaged OSI and DSI. The repetitions that generated a negative number were disregarded, as the preferred direction was unreliable in such a case.

To extract the phase angle of APs, a bandpass filter was applied to the spike-removed traces to extract the 4- to 7-Hz Vm activities. The phase angles of every time point were computed with a Hilbert transform. The phases of APs within the visual response window were extracted.

To extract the light-evoked EPSC, a 0.2-s baseline before the onset of the stimulus was selected for each trial. The EPSP peaks were detected from 0 to 40 ms after the stimulus onset. The difference from the baseline to the EPSC peak was defined as the EPSC amplitude. The EPSC latency was defined as the time interval between center the TTL signal of the stimulus and the time of the EPSC reached 5% of the amplitude (Boudkkazi et al., 2007). We only used the cells that had <3.5-ms average EPSC latency.

All data analysis was performed in Python. The source code is available from the corresponding author on reasonable request.

2.3.8 Network simulation

In the model, the activity of, and synaptic interactions between, the neurons are parametrized by their preferred direction φ which is uniformly distributed along a ring between –π and π. To account for enhanced low-frequency oscillation with visual learning, slow negative feedback such

as firing rate adaptation was included as in the previous work (Lim, 2019). The dynamics of network activity is described by the following equations:

$$\tau_r \frac{dr(\phi,t)}{dt} = -r(\phi,t) + f\left(\int_{-\pi}^{\pi} J(\phi,\phi')r(\phi',t)d\phi' + i(\phi,t) - ka(\phi,t)\right)$$

$$\tau_a \frac{da(\phi,t)}{dt} = -a(\phi,t) + r(\phi,t)$$

where $r(\phi,t)$ and $a(\phi,t)$ represent the mean firing rate and adaptation variable of populations with the preferred feature ϕ. $r(\phi,t)$ approaches $f(x(\phi,t))$ with intrinsic time constant Embedded Image, where f(x) is the steady-state neuronal response to input current x. Here, we considered a threshold nonlinear function, that is, f(x) = x when x ≥ 0, and otherwise 0.

The input $x(\phi,t)$ to a population with the preferred feature ϕ is a sum of the recurrent synaptic currents $J(\phi,\phi')r(\phi',t)$ with the preferred feature ϕ', the feedforward current $i(\phi,t)$ minus the adaptation current $ka(\phi,t)$. We considered a linear mechanism for adaptation such that $ka(\phi,t)$ is a low-pass filtered firing rate $r(\phi,t)$ with time constant τ_a and strength *k*. In the recurrent inputs, $J(\phi,\phi')$ represents the synaptic connectivity strength, which depends only on the distance between ϕ and ϕ'. Thus, it can be written as $J(\phi-\phi')$ and we assumed that $J(\phi-\phi')$ is the sum of Gaussian functions as $J_E\, exp[-(\phi-\phi')^2/{\sigma_E}^2] - J_I\, exp[-(\phi-\phi')^2/{\sigma_I}^2]$ where the subscripts *E* and *I* represent the recurrent excitation and inhibition. The external current $i(\phi,t)$ is modeled as a product of a spatial component $i_s(\phi)$ and a temporal component $i_t(t)$ so that $i(\phi,t) = i_s(\phi)i_t(t)$. The temporal component $i_t(t)$ is a pulse of duration t_{stim} that is exponentially filtered with time constant τ_{ext}. The spatial component $i_s(\phi)$ is the sum of two Gaussian functions with the same width and centered at the stimulus direction ϕ_0 and its opposite direction with two modulation factors γ_0 and γ_1 as $i(\phi) = \gamma_0(exp[-(\phi-\phi_0)^2/{\sigma_{stim}}^2] + \gamma_1\, exp[-(\phi-\phi_0+\pi)^2/{\sigma_{stim}}^2])$.

The parameters used in the simulation are following – the time constants and parameters for the adaptation and the feedforward inputs except the overall modulation factor γ_0 did not change with learning, given as τ_r = 5 ms, τ_a = 150 ms, τ_{ext} = 50 ms, t_{stim} = 500 ms, k = 1, σ_{stim} = π/10 and γ_1 = 0.2. Learning induced changes in the recurrent connections and overall feedforward strengths such that before learning, γ_0 = 1, J_E = 0.15, σ_E = ∞, J_I = 0, and after learning, γ_0 = 0.5, J_E = 3, σ_E = π/6, J_I = 1, σ_I = ∞. Here, σ = ∞ for Gaussian functions represents a constant profile

and the parameters for adaptation currents were chosen to generate the low-theta oscillation after learning. The simulation was run with a fourth-order explicit Runge-Kutta method in MATLAB, and the source code will be available to anyone interested.

2.3.9 Statistical analysis

For recording with only single direction stimulus, we used two-sided Mann–Whitney *U* tests for comparison on band magnitude, ΔV_m, firing rate, and oscillation probability. For 12 direction tuning data, we performed mixed-design two-way ANOVA with directions as a within-subject factor and visual experience as a between-subject factor. Mixed-design two-way ANOVA was performed on firing rate, band magnitude, band coherence, and the AP phase angles. Mauchly's sphericity test was used to determine whether a Greenhouse–Geisser correction was needed. We used two-sided Mann–Whitney *U* tests for pair-wise comparison after ANOVA. Benjamini–Hochberg FDR correction was used whenever a correction on the p-value was required. Two-sided Mann–Whitney *U* tests were also used to compare OSI, DSI, and the light-evoked EPSP amplitudes of naive and experienced mice. All statistical analysis was performed using Pingouin, an open-source statistic Python package.

2.4 Results

2.4.1 Visual familiarity induced oscillations reduced visual responses in V1

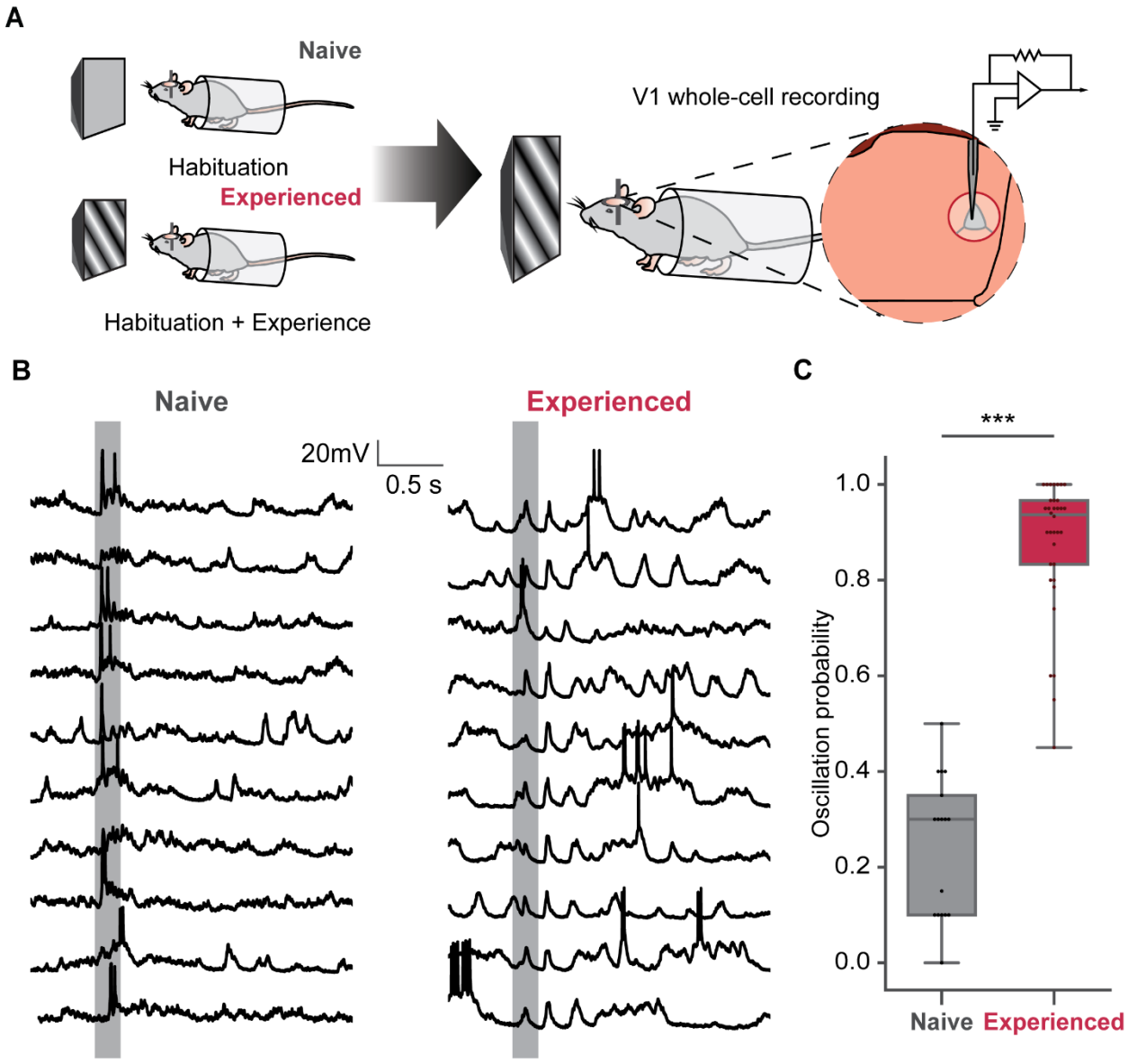

Figure 2.1 5 Hz oscillations evoked by familiar visual stimulus. A. Experimental setup and passive visual experience paradigm. After two days of habituation, mice were either presented with the sinusoidal grating stimulus or habituated for 4 more days. In vivo whole-cell recordings were performed on awake mice. B. Representative traces of cells responding to the stimulus in naive and experienced mice. Grey rectangles represent the visual stimuli duration. C. Box plot and swarm plot of oscillation probabilities of cells recorded in naive and experienced mice. ***-$p<0.001$

To dissect the mechanism of visual familiarity evoked 5-Hz oscillations, we performed whole-cell patch-clamp recordings in L2/3 of V1 in awake mice. Age-matched mice were divided into two groups. After 2 d of habituation, one group (naive) was habituated with gray screen for four more days; the other group (experienced) was familiarized with a sinusoidal grating stimulus (200 ms, 0.04 cycle/°, 2 Hz, 200 repeats/d, 4 d) via passive viewing (Figure 2.1A). The visual responses of L2/3 neurons to the same grating stimulus were recorded from both groups. The stimulus was novel to the naive mice that only habituated with the gray screen but was familiar to the experienced mice that passively viewed it for 4 d. The mice were awake during the recordings. We successfully recorded cells from nine naive and 16 experienced mice. A total of 17 cells recorded from the naive mice and 34 cells recorded from the experienced mice had subthreshold visually evoked responses on Vm. Among these cells, three cells in naive mice and six cells in experienced mice had no superthreshold responses. They were discarded in the superthreshold analysis. While the Vm oscillations can also be found in some trials in the naive mice (Figure 2.1C), the ratio of oscillation trials greatly increased in the experienced mice (Mann–Whitney U test, $U = 1.0$, $p =$

$4.06 \times 10{-}9$). In some cells from experienced mice, the 5-Hz oscillations occurred in all trials following the visual stimulus onset (Figure 2.1B, C). In naive mice, neurons responded to the novel visual stimulus with a strong peak of firing, followed by a smaller second peak (Figure 2.2C). Consistent with our previous work (Kissinger et al., 2018), the visual stimulus-evoked oscillatory APs responses extended beyond the stimulus in experienced mice (Figure 2.2A, lower, C). Most cells preferred to fire at the second and the third cycles of the oscillation. Meanwhile, firing during the first cycle of oscillation was significantly reduced. We computed the baseline-subtracted firing rate of all cells, using 0.05–0.25 s after the stimulus onset as the visual response time window and 2.5–4.7 s after the onset as the baseline. The decreased firing rate of the visual response in experienced ($n = 14$ cells) mice was significant compared with naive ($n = 28$ cells) mice ($U = 347.0$, $p = 5.9 \times 10{-}5$; Figure 2.2H).

In addition to the APs' oscillatory activity, the subthreshold Vm oscillations were also prominent in the responses of experienced mice (Figure 2.2B, lower). The visually evoked oscillations in the Vm lasted for three to four cycles in most neurons following the stimulus (Figure 2.2B, lower, D) in experienced mice. In naive mice, Vm had no oscillations, but rather a broad depolarization following the visual stimulus (Figure 2.2B, upper). The power spectra of Vm

(Figure 2.2E) showed a significant increase in power around 5 Hz. The magnitude of 4- to 7-Hz band Vm significantly increased in experienced mice compared with naive mice (naive, n = 17 cells; experienced, n = 34 cells; Mann–Whitney U test, U = 148.0, p = 0.0050; Figure 2.2F). No significant changes happened in the 8- to 12-Hz (U = 201.0, p = 0.080) and 13- to 30-Hz (U = 224.0, p = 0.20) oscillations. We took the times of the first three cycles of 5-Hz Vm oscillation in experienced mice, and defined three time windows (I, 0.05–0.25 s; II, 0.25–0.45 s; III, 0.45–0.65 s after stimulus) to quantify the Vm peaks for each cycle. The average Vm of 2.5–4.7 s after the stimulus onset was subtracted from the Vm peaks. The baseline subtracted peak Vm (ΔVm) was compared with the averaged maximum ΔVm within the same time windows in naive mice (Figure 2.2G). The membrane oscillation strongly suppressed Vm during the visual stimulus. The peak ΔVm of the first cycle in experienced mice was lower than the peak ΔVm of the same time window in naive mice (U = 450.0, p = 0.0013). Meanwhile, there was no significant difference in ΔVm at the time window of the second (U = 368.0, p = 0.12) and third cycle (U = 212.0, p = 0.13) between the two groups (Figure 2.2G).

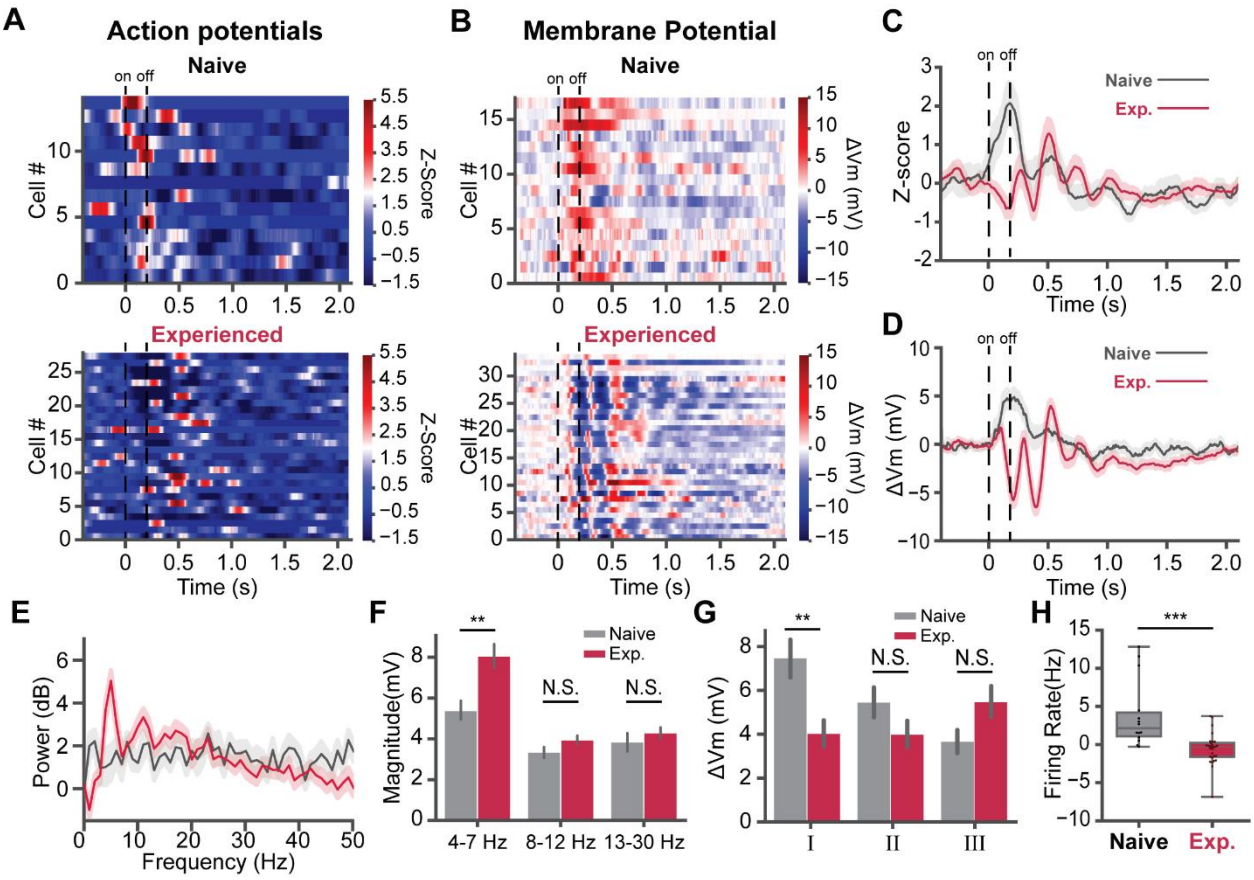

Figure 2.2 5 Hz oscillations correlate with the decreased firing rate of neural responses. A. Z-scored firing rate of cells in naive (top, 14 cells) and experienced mice (bottom, 28 cells). Dashed lines indicate the stimulus onset/offset. B. Baseline-subtracted Vm (Δ Vm) of responses in naive (top, 17 cells) and experienced mice (bottom, 34 cells). C. Average Z-scored firing rate of neurons in naive (grey, 14 cells) and experienced (crimson, 28 cells) mice. The shaded area represents the SEM. D. The averaged ΔVm of cells in naive (grey, 17 cells) and experienced (crimson, 34 cells) mice. E. Cell averaged power spectra of Vm subthreshold responses for naive (grey, 17 cells) and experienced mice (crimson, 34 cells). F. Vm powers in several frequencies bands. The average magnitude of 4-7 Hz, 8 - 12 Hz and 13-30 Hz bands were computed(naive, 17 cells; experienced, 34 cells). G. Peaks of baseline subtracted membrane potential (ΔVm) from the first (I), second (II) and third (III) time windows. Each window corresponds to a cycle of the 5 Hz oscillation in experienced mice. H. The average firing rate of cells in naive (14 cells) and experienced mice (28 cells). The baseline firing rate was subtracted from each cell. *- $p<0.05$, **- $p<0.01$, ***- $p<0.001$, N.S.- not significant. Error bars indicate mean ±SEM.

2.4.2 Visual experience improves the orientation and direction selectivities of V1 neurons

Our results showed that visual experience led to the emergence of the 5-Hz oscillations and a decreased population-averaged firing rate during the visual stimulus. However, the reduced firing rate could result in a decreased feature selectivity because of the reduced visual responsiveness; or it could result in an increased feature selectivity by increasing the preferred/non-preferred response ratio. In previous studies, enhanced selectivity of V1 neurons has been found in conjunction with perceptual learning and reward training with visual cues (Schoups et al., 2001; Poort et al., 2015; Khan et al., 2018). To determine whether the feature selectivity of L2/3 neurons was enhanced after the visual experience, we next recorded responses to 12 directions of drifting sinusoidal gratings in awake mice. Age-matched mice were separated into two groups, habituated and familiarized to the specific visual stimulus as described in the previous experiment. Sinusoidal grating stimuli of a 500-ms duration with the same spatial (0.04 cycle/°) and temporal frequency (2 Hz) of 12 drifting directions (30° between each direction) were used for orientation and direction tuning recordings (Figure 2.3A). Stimuli of 12 different directions were presented in a pseudorandom sequence with 3.5 s intervals. We were able to record 14 cells from 11 naive mice and 15 cells from 12 experienced mice. Surprisingly, the Vm oscillations occurred in responses to visual stimuli of all directions in the experienced mice (Figure 2.3C, 4D), not only to the familiar direction used in passive viewing (60° to horizontal). To quantify the superthreshold visual response, 0.05–0.55 s after visual stimuli onset was used as the visual response time window for APs. The 2.5–3.5 s after the onset was used as the baseline and subtracted from each trial. The baseline-subtracted firing rates of preferred, opposite, and orthogonal directions in experienced mice were significantly lower compared with naive mice ($U = 1354.0$, $p = 0.00052$), No interaction between the direction and visual experience was found (naive, $n = 14$ cells; experienced, $n = 15$ cells; two-way ANOVA, $F = 0.091$, $p = 91.33$; Figure 2.3F,G). To determine whether the DS and OS of V1 neurons were changed, we computed the OSI and DSI of recorded neurons (Figure 2.3H). OSI increased in the experienced mice that were familiarized with the stimulus ($U = 49.0$, $p = 0.015$). The DSI also increased in the experienced mice ($U = 42.0$, $p = 0.0064$).

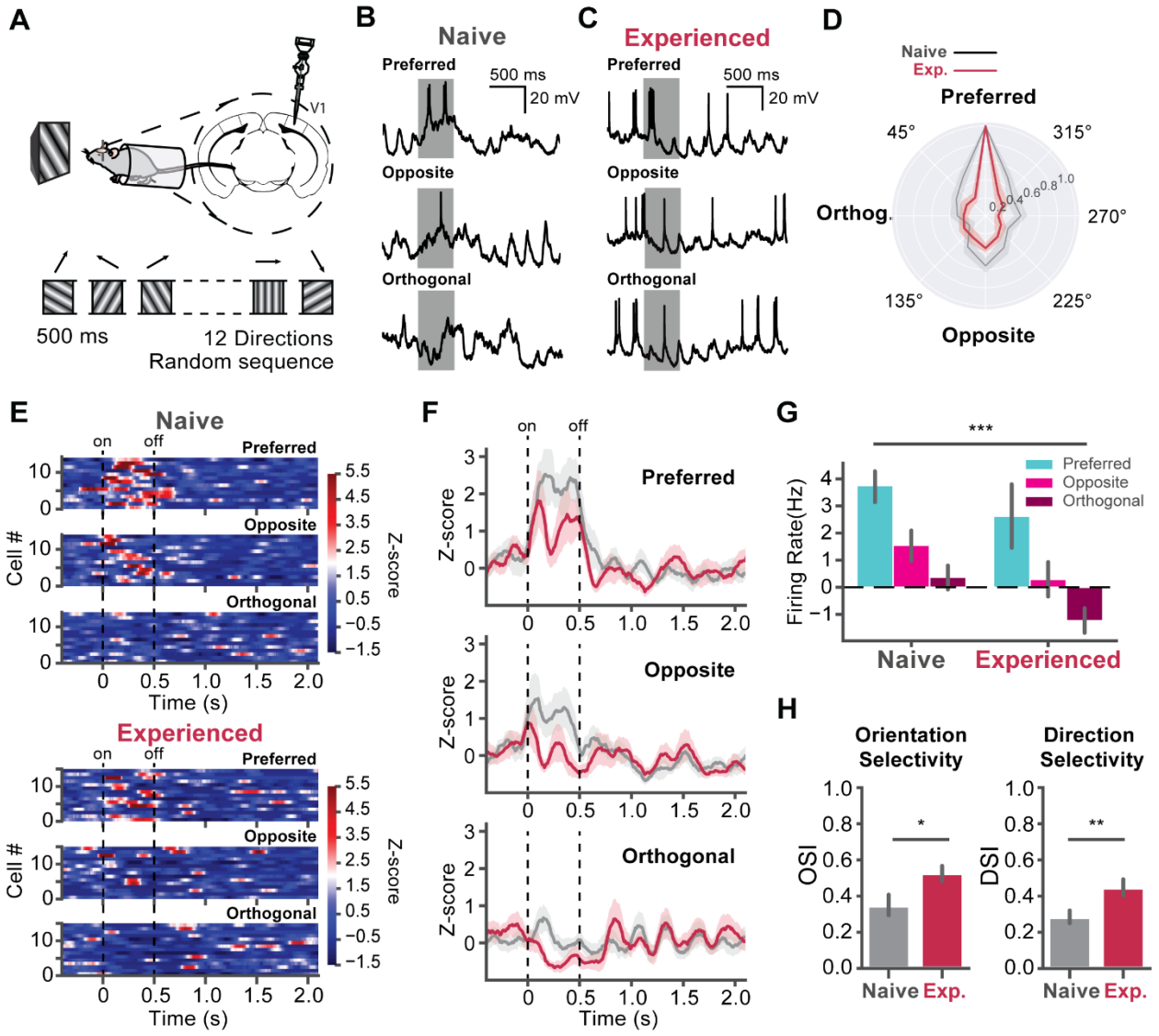

Figure 2.3 Visual experience improves the direction selectivity in V1. A. Experimental design for direction tuning in V1. The naive and experienced mice were recorded with 500 ms sinusoidal grating stimuli with 12 directions in pseudorandom sequences. B. Example traces of a cell responding to the preferred, opposite and orthogonal visual stimuli. C. Same as B, but for a cell in an experienced mouse. D. Normalized responses of cells in naive (grey, 14 cells) and experienced (crimson, 15 cells) mice for 12 directions. The shaded areas represent SEM of the responses. E. Heatmaps of Z-scored firing rates of cells in naive and cells in experienced mice. The color bar shows the z-score scale. F. The time courses of averaged z-scored firing rates of V1 cells in naive and experienced mice. G. The average firing rate during visual stimulus of the naive and experienced mice. The baseline firing rate was subtracted. The firing rate significantly decrased in the experienced compared to naive mice. H. Left, the bar plots of the OSI. The OSI of cells in the naive (grey) and experienced mice (crimson). Right, the bar plot of DSI. *- $p<0.05$, **- $p<0.01$, ***- $p<0.001$, N.S. - not significant. Error bars indicate mean ±SEM.

We then performed time-frequency analysis on Vm (Figure 2.4A), and extracted the powers of the 4- to 7-, 8- to 12-, and 13- to 30-Hz bands for the preferred, opposite, and orthogonal directions. We also computed the averaged power spectrum of Vm in the visual response time window (Figure 2.4C) and the band magnitudes by bandpass filtering Vm. For all three directions, the 4- to 7-Hz amplitude significantly increased in the experienced mice compared with naive mice ($U = 54.0$, $p = 0.028$; Figure 2.4D, top). No interaction between the directions and visual experience was found (two-way ANOVA, $F = 0.0813$, $p = 0.92$). The visual experience did not affect the 8- to 12-Hz band ($F = 0.336$, $p = 0.567$) and 13- to 30-Hz band ($F = 0.0192$, $p = 0.89$). We also computed the intertrial phase coherence (ITPC) of the Vm visual responses (Figure 2.4B). The 4- to 7-Hz ITPC increased in the experienced mice ($U = 31.0$, $p = 0.0013$; Figure 2.4E, top), while no interaction between directions and visual experience was found ($F = 1.464$, $p = 0.24$). The cell averaged ITPC reached ~0.7 in experienced mice. Such strong coherence suggests the oscillation was strongly time-locked to the visual stimuli. The coherence of 8- to 12-Hz band also increased in the experienced mice when the orthogonal stimulus was present (two-way ANOVA, $F = 2.06$, $p = 0.012$, pair-wise U test, $U = 38.0$, $p = 0.011$; Figure 2.4E, middle), and was unchanged for preferred ($U = 62.0$, $p = 0.095$) and opposite direction ($U = 89.0$, $p = 0.50$). The ITPC of 13- to 30-Hz band remained low and unchanged in naive and experienced mice ($F = 0.195$, $p = 0.66$; Figure 2.4E, bottom).

To quantify the phase-locking activity of APs, we filtered the Vm traces to extract the 4- to 7-Hz Vm and transferred the filtered signals to analytical signals using Hilbert transform. The phase angle of APs was extracted. The APs shifted toward the rising phase of the Vm oscillation for the preferred direction in the experienced mice (two-way ANOVA, $F = 8.078$, $p = 0.00032$; pair-wise U test, $U = 79{,}427.0$, $p = 0.027$; Figure 2.5A), while the APs shifted toward the falling phase of the Vm oscillation for the opposite direction ($U = 18{,}591.0$, $p = 0.00011$; Figure 2.5B). The APs phase angles were not shifted for the orthogonal direction ($U = 9143.0$, $p = 0.85$; Figure 2.5C).

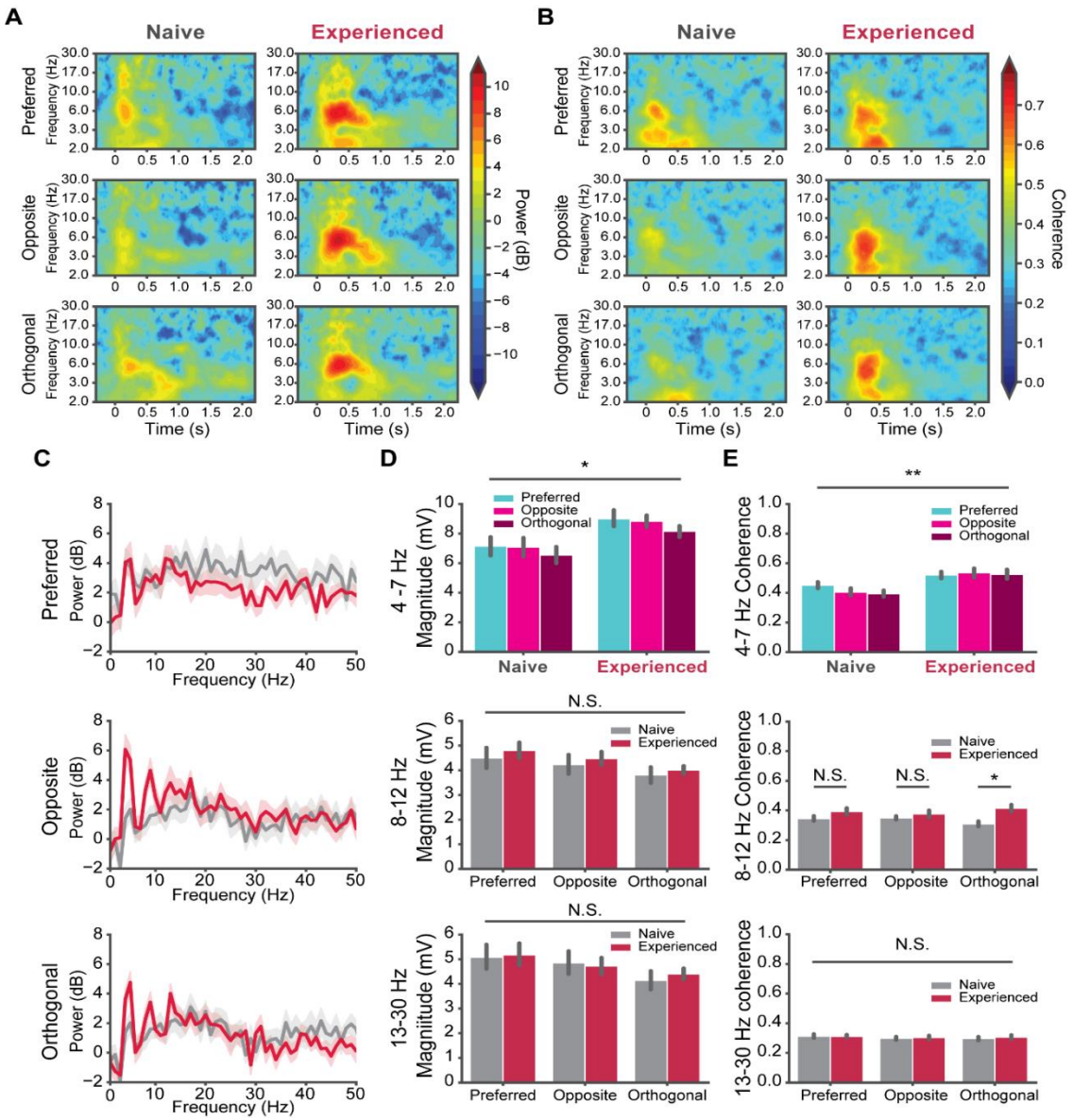

Figure 2.4 Membrane potential oscillations during V1 direction tuning. A. Time-frequency spectrograms of the V_m responses to visual stimuli. The V_m of each cell responding to preferred, opposite, and orthogonal direction were converted to the time and frequency domain by wavelet transform. The heat in each spectrogram represents the baseline normalized power in dB. Left column, naive mice; right, experienced mice. B. The inter-trial phase coherence (ITPC) of V_m responses to the preferred, opposite, and orthogonal directions. Left column, naive mice; right column, experienced mice. The heat represents the ITPC. C. Average power spectra of V_m responses to the preferred, opposite, and orthogonal direction naive (grey) and experienced mice (red). D. Top, the 4 - 7 Hz magnitude of cells in naive and experienced mice for the preferred, opposite and orthogonal directions. Middle, same as the top, but for the alpha band (8-12Hz). Bottom, same as top but for the beta band (18-30 Hz). E. The averaged ITPC of V_m during the visual stimuli in naive and experienced mice. Top, 4 - 7 Hz ITPC; middle, alpha band ITPC; bottom, beta band ITPC. *- $p<0.05$, **- $p<0.01$, ***- $p<0.001$, N.S. - not significant. Error bars indicate mean ±SEM.

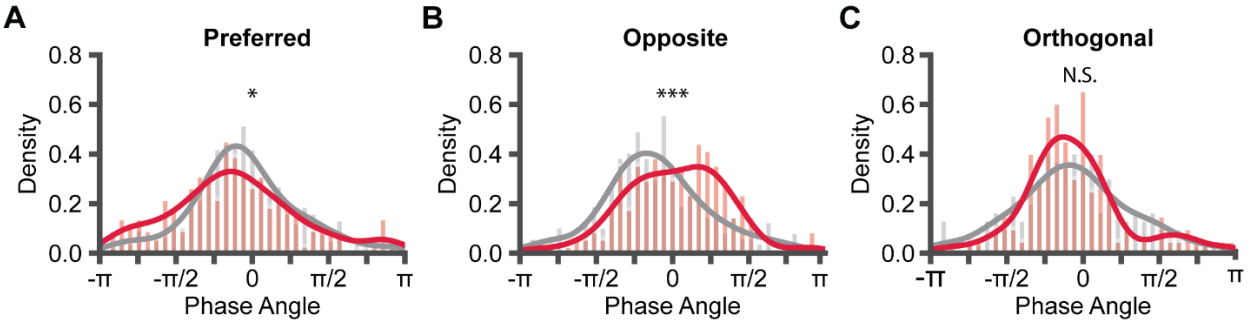

Figure 2.5 AP phase distributions during membrane potential oscillations. A. Density histograms of APs 4 – 7 Hz phase angle distribution. '0' phase angle represents the peak of 4 – 7 Hz V_m. Negative phase angles represent the rising phase, and positive phase angles represent the falling phase. B and C. Same as A, but for the opposite and orthogonal directions. *- $p<0.05$, ***- $p<0.001$. N.S. - not significant.

2.4.3 Synaptic strengthening of L5 projections after the visual experience

To dissect the synaptic plasticity mechanisms underlying the emergence of the 5 Hz oscillation and the enhanced selectivity, we searched for synaptic changes that were induced by visual experience. One possibility was that the synaptic strength of L5 projections, which carry feedback information from recurrent circuits in V1 and higher visual areas, was changed. To test this hypothesis, we measured postsynaptic responses in vivo with photoactivation of channelrhodopsin 2(ChR2)-positive synaptic terminals formed by L5 neurons. We used Thy-1-ChR2-YFP mice, where ChR2 is sparsely expressed in L5 pyramidal cells in V1 (Arenkiel et al., 2007). To improve the success rate and stability of the patches, we anesthetized mice with ketamine/xylazine. To optogenetically activate the ChR2-positive presynaptic terminals formed onto the patched cells, we used a specialized pipette holder with a port for the optical fiber, optopatcher (Katz et al., 2013). Blue laser light (wavelength 473nm) was delivered through the tip of the recording pipette so that the intensity of light used for each cell was the same regardless of the depth (Figure 2.6A).

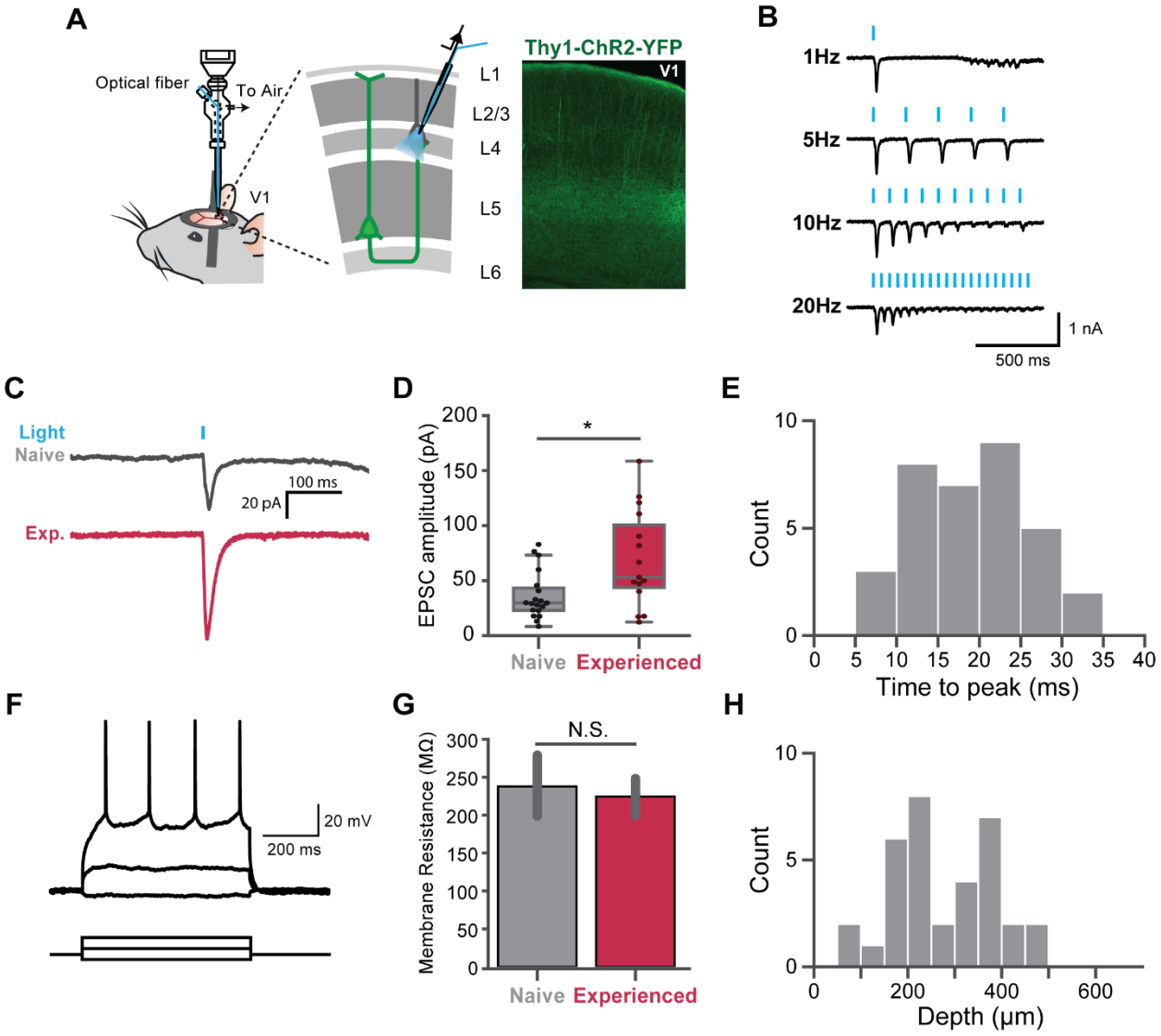

Figure 2.6. Synaptic strengthening of L5 projections by visual experience. A. Left, recording schematic. Whole-cell recordings were made on random pyramidal cells in L 2/3 and Layer 4 (L4). Right, a V1 brain slice of Thy1-ChR2-YFP transgenic mice. Channelrhodopsin-2 was sparsely expressed in V1 in these mice. Intra- and inter-cortical projections from L5 ChR2 expressing cells were activated with 473 nm laser pulses. Light-induced EPSCs were recorded in voltage-clamp mode. B. An example of 1, 5, 10 and 20 Hz light pulses inducing presynaptic short-term depression in a patched neuron. C. Examples of light-induced EPSC traces from single cells in a naive (top, grey) and an experienced mouse (bottom, red). D. Averaged EPSC amplitudes of cells in naive (grey, 19 cells) and experienced mice (crimson, 15 cells). The EPSC amplitudes in experienced mice was significantly higher than naive mice. E. The average time interval from the stimulus onset to the peak of the EPSC of all cells (34 cells). F. Representative traces of step current injections in current-clamp mode. 10 nA increments were used for step current injection. Three steps are shown here. G. The membrane resistance of cells in naive and experienced mice showed no significant difference. H. The depth distribution of the responsive cells. *- $p<0.05$, N.S.- not significant. Error bars indicate mean ±SEM.

2.4.4 Thalamocortical synapses are weakened by visual experience

We observed the decrease in the firing rate of visual responses, especially in the first peak of oscillation. This may result from decreased thalamocortical projection strength. To test if the strength of thalamocortical projections was changed, we measured the postsynaptic responses in vivo with photoactivation of ChR2-positive thalamocortical terminals. To achieve the specific activation of thalamocortical projections, we used the VGlut2-ChR2-YFP mice, which express ChR2 specifically in the visual thalamus. In the VGluT2-ChR2 transgenic mouse line, ChR2 is expressed under the vesicular glutamate transporter 2 (VGluT2) promoter (Hagglund et al., 2010). VGluT2 has been shown to be specifically expressed in the thalamus, but not in the primary visual cortex (Coleman et al., 2010). The axons which formed connections onto patched neurons were activated by 5 ms light pulses (Figure 2.7B). EPSCs of 10 trials were recorded for each cell. 17 out of 23 cells recorded in naive mice and 15 out of 26 cells recorded in experienced mice had monosynaptic responses (Figure 2.7C). The average EPSC amplitudes were lower in experienced mice compared to naive mice (Mann-Whitney test, $U=64.0$, $p=0.0141$). We also measured the membrane resistance of these cells, but discovered no difference between the two groups ($U= 72.0$, $p = 0.60$, Figure 2.7F).

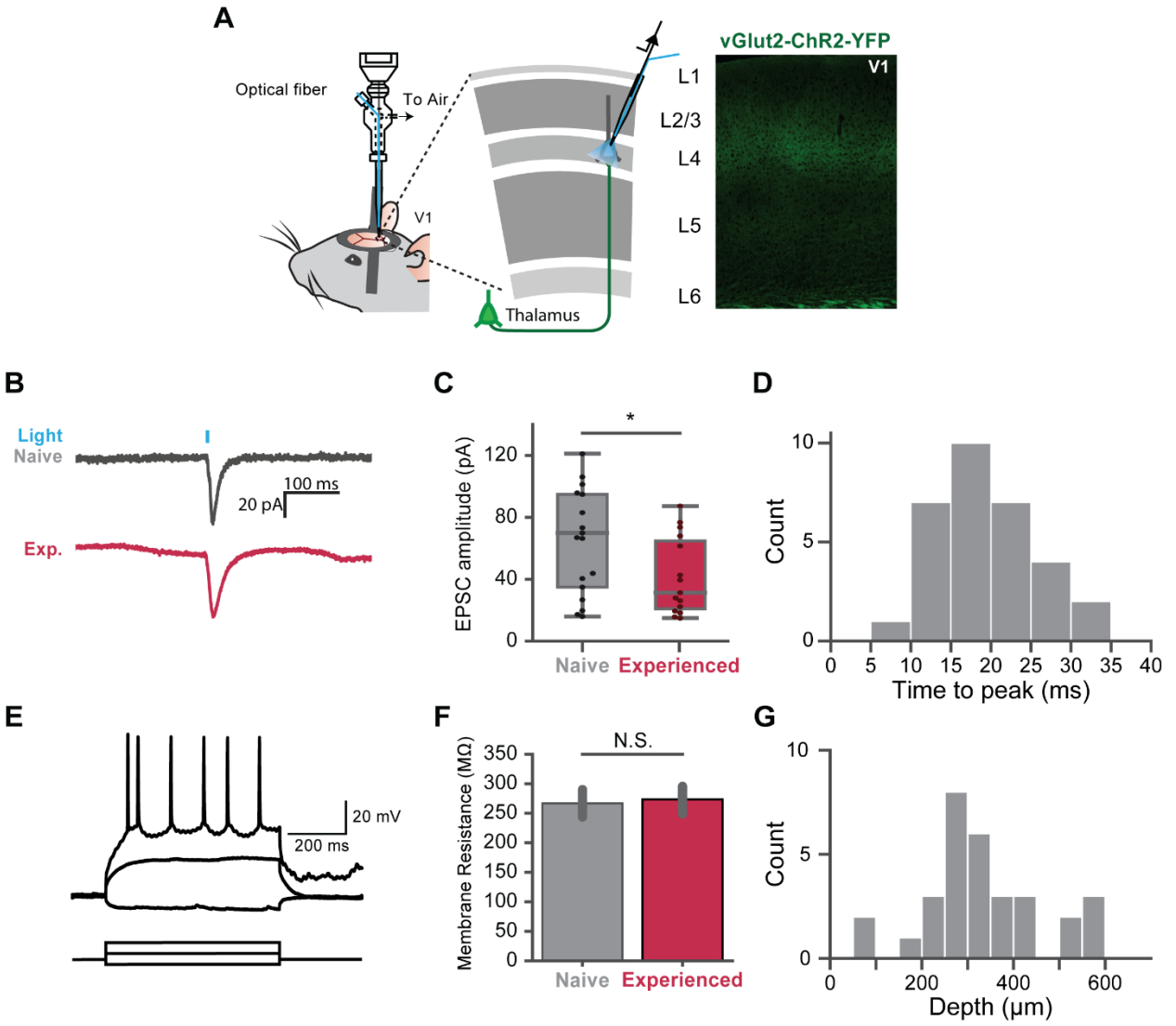

Figure 2.7. Thalamocortical synaptic strength is reduced by visual experience. A. Left, whole-cell recordings were made on random neurons in L2/3 and L4. Right, V1 brain slice of VGlut2-ChR2-YFP transgenic mice. Channelrhodopsin-2 was expressed in the thalamocortical projections. Light-induced EPSC were recorded in voltage clamp mode. B. Examples of light-induced EPSC traces from single cells in a naive (top, grey) and experienced mouse (bottom, red). C. Averaged EPSC amplitudes of cells in naive (grey, 16 cells) and experienced (crimson, 15 cells) mice. The EPSC amplitudes in experienced mice was lower than naive mice. D. The average time interval from the stimulus onset to the peak of the EPSC of all cells (31 cells). E. Representative traces of step current injections in current-clamp mode. 10 nA increments were used for the step current injection. Three traces are shown here. F. The membrane resistance of cells in naive and experienced mice showed no significant difference. G. The depth distribution of the responsive cells. *- $p<0.05$, N.S.- not significant. Error bars indicate mean ±SEM.

2.4.5 Network mechanism underlying 5 Hz oscillations following visual experience

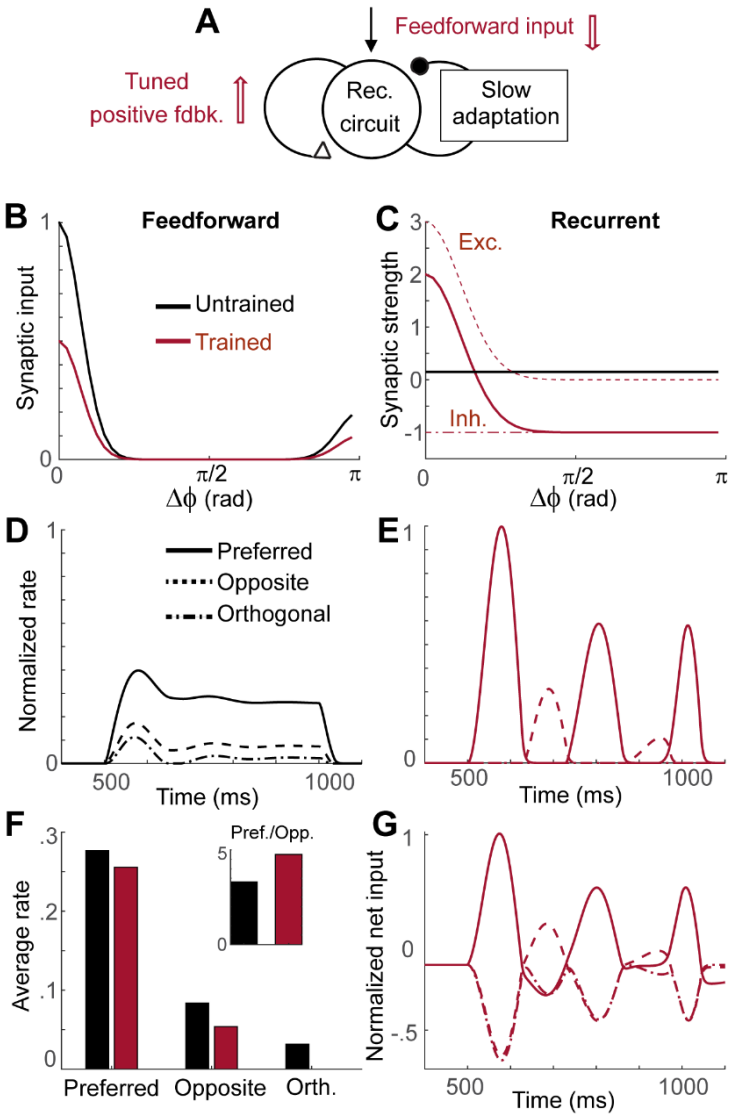

Figure 2.8. Network model with synaptic plasticity and slow adaptation reproduces the effects of visual experience. A-C. Synaptic plasticity induced by learning. In the network with a ring structure and slow adaptation, feedforward and recurrent synapses undergo synaptic plasticity in the opposite directions (red arrows in A), that is, a decrease of the feedforward inputs (B) and more structured and stronger connections of recurrent inputs (C). Here, Δφ represents difference between the preferred directions of neurons. D, E. Network activities before (D) and after learning (E). The stimulus is presented between 500 ms and 1000 ms, and all activities are normalized by the maximum firing rates after learning. Note the activity for orthogonal stimuli is zero due to thresholding. F. Changes in average activities during the stimulus presentation with learning and the ratio of the activities in the preferred direction to that in the opposite direction (inset). G. Net input normalized by its maximum after learning.

To obtain the mechanistic understanding of the effects of visual experience observed in V1, we considered a recurrent network model where activities of neurons are described by their firing rates (Figure 2.8A). Previously, interactions between synaptic plasticity of recurrent connections and slow negative feedback such as spike frequency adaptation were proposed to account for similar effects of the visual experience observed in monkey inferotemporal cortex (Lim, 2019). We modified this model so that the network is organized in a one-dimensional ring structure where each unit represents a population of neurons having similar directional selectivity (Ben-Yishai et al., 1995; Ermentrout, 1998). We assumed that visual experience induces changes in both recurrent and feedforward inputs, as observed experimentally (Figure 2.6 and 7). Before learning,

the network receives uniform recurrent input and asymmetric feedforward inputs with strong input at the stimulus direction and relatively weak but non-zero input in the opposite direction (black in Figure 2.8B, C). The latter is a simplification of the experimental observation that thalamic inputs provide a primordial bias for directional selectivity in V1 (Lien and Scanziani, 2018). After learning, the feedforward inputs scale down uniformly, while recurrent inputs become structured with local excitation and global inhibition (red in Figure 2.8B, C). Such changes in recurrent connections were inspired by the experimental observation of the reorganization of recurrent connections during the development (Ko et al., 2011) and biologically realistic models suggesting direction-based connectivity rules in recurrent synaptic strengths (Billeh et al., 2020). Note that we assumed that the emergence of oscillation after learning is intrinsic to V1 circuits with no oscillation in the feedforward or feedback inputs from other areas, similarly to the previous modeling works (Lien and Scanziani, 2018; Billeh et al., 2020).

The model reproduced the main effects of visual experience, enhanced directional selectivity, and low-frequency oscillations with a decrease in overall firing rates. Before learning, the network shows little oscillations but shows direction selectivity inherited by the feedforward input (Figure 2.8D, F). After learning, strong low-frequency oscillation emerges in both preferred and opposite directions (Figure 2.8E) because enhanced recurrent connections in the neurons with similar preferred directions lead to stronger positive feedback and its interaction with slow adaptation generates oscillation (Figure 2.8A). The anti-phase oscillation in the opposite direction is led by net inhibitory inputs from neurons at the preferred directions, and the activity for the orthogonal directions is suppressed below the threshold (Figure 2.8E). However, the net input shows the increased oscillation across all directions as an enhanced oscillation in voltage observed experimentally (Figure 2.8G). Recurrent synaptic plasticity also leads to enhanced directional selectivity as the ratio of the average firing rate at the preferred direction to that of the opposite increased, while overall firing rates decrease due to depression in the feedforward inputs (Figure 2.8F). Note that instead of uniform depression in the feedforward inputs, more structured changes of them can also contribute to the enhanced directional selectivity, yet feedforward synaptic plasticity alone is not sufficient to reproduce changes in response dynamics. Thus, both recurrent and feedforward synaptic plasticity is required, as observed experimentally.

2.5 Discussion

Here, we demonstrated that a familiar visual stimulus could reliably evoke a 5 Hz oscillation in V1 of single cells in awake mice, confirming previous studies (Einstein et al., 2017; Kissinger et al., 2018). The oscillations were observed as both oscillatory fluctuations in membrane potential and firing rate and were accompanied by reduced firing at the visual stimulus onset. They were also strongly time-locked to the visual stimuli. They closely followed the stimuli and were highly coherent across trials. A similar observation was made in a previous study, where spontaneous 3-5 Hz Vm oscillations in V1 had a suppressive effect on visual responses (Einstein et al., 2017). We found that the oscillations were also not specific to the direction of the visual stimulus used for familiarization but could be recruited by all directions of visual stimuli in experienced mice. This observation confirmed a previous finding that the oscillation was more sensitive to the spatial frequency content rather than the direction of stimuli (Kissinger et al., 2018).

V1 has long been known to have specialized cell assemblies that extract specific features from visual stimuli (Hubel and Wiesel, 1959, 1962). The selectivity of these neurons can be changed not only in the developing brain but also in adults during learning. Previous studies have demonstrated that the selectivity of V1 can be modulated by perceptual learning (Schoups et al., 2001), classical conditioning (Goltstein et al., 2013), and reinforcement learning (Poort et al., 2015). In our study, we observed improved direction selectivity following the visual experience, which was accompanied by increased 5 Hz oscillation. The 4-7 Hz power of Vm was increased, and the firing rates of the visual responses decreased in experienced mice regardless of the direction of the stimuli. Although this reduction was not direction-specific, the responses to the opposite and orthogonal directions demonstrated a larger proportion decrease than the preferred direction. Such changes led to the increased direction and orientation selectivities. On the other hand, the selectivity of V1 neurons was improved while the neurons fired fewer APs, implying the encoding of visual stimuli in V1 could become more efficient. A very similar scenario of enhanced selectivity of V1 neurons had been demonstrated by non-specific activation of interneurons with optogenetics (Lee et al., 2012). The changes in visual responses and selectivity in this study were very similar to what we observed here after visual experience. The enhanced selectivity we observed could partially result from the experience-dependent recruitment of interneurons.

Reinforcement learning with a visual cue has been demonstrated to induce experience-dependent plasticity in adult V1, where the timing of the expected reward was reported by neural

activity (Shuler and Bear, 2006; Chubykin et al., 2013). Noticeably, neural oscillations at a similar frequency range in V1 were also observed in rats undergoing reward training, and their duration reported the timing of the reward (Zold and Hussain Shuler, 2015; Levy et al., 2017). In our study, we also sought to find the synaptic strength changes associated with the 5 Hz oscillation. With optogenetically evoked EPSC measurements, we found that the L5 to superficial layers projection strength was increased, while the thalamocortical projection strength was decreased. The decreased thalamocortical projection strength could at least partially explain the reduction in firing rates at the onset of visual stimulation. These changes in synaptic strength may, at least in part, promote the emergence of oscillation and allow for enhanced selectivity. The synaptic changes we discovered were relatively large. We cannot determine if such changes were uniform or were specific to the certain features of the visual stimulus from our results. However, since 5 Hz oscillations were found to be entrained by a wide range of visual stimuli yet were specific to the spatial frequency of the stimulus (Kissinger et al., 2018), the synaptic changes induced by experience could be structured with feature specificities. Meanwhile, the stimulus we used for the visual experience was also fairly strong compared to the natural visual input mice experience in their home cage. Our stimuli were 100% contrast, with a high number of repeats presented within a relatively short time period. These factors could contribute to the relatively large synaptic changes. Synaptic changes induced by the natural visual experience need to be further explored in the future.

Previous studies have suggested the brain state is correlated with the low-frequency activities in cortical areas (Harris and Thiele, 2011). Low-frequency Vm fluctuation of V1 neurons was stronger during the quiet wakefulness than the highly aroused state and was strongly correlated with pupil size (Reimer et al., 2014). Such low-frequency activities are mostly spontaneous and not temporally associated with visual stimuli. The increased low-frequency activity during quiet wakefulness was also accompanied by decreased high-frequency power in the gamma range (Niell and Stryker, 2010). However, in our study, the 5 Hz oscillation was robustly evoked and strongly time-locked to the visual stimuli. Contrary to the low-frequency oscillations that happened during quiet wakefulness, the 5 Hz oscillation induced by visual experience was accompanied by increased gamma range oscillation (Kissinger et al., 2018; Kissinger et al., 2020). Furthermore, although the magnitude of the visually evoked 5 Hz oscillation was higher in immobile mice, the oscillations were also strong during the mobile periods (Kissinger et al., 2020). Additionally, 3 - 5

Hz Vm oscillation was also found to happen in both high and low arousal states with similar likelihoods (Einstein et al., 2017). Thus, whereas the 5 Hz oscillations may be modified by the brain state, they are primarily triggered by the familiar stimulus.

Interestingly, the improvement of selectivity to familiar visual stimuli was also found in the primate inferior temporal cortex (ITC) (Kobatake et al., 1998; Freedman et al., 2006). Similar to what we report here, the improvement of selectivity of ITC neurons was also achieved by temporally sharpened visual responses and decreased average firing rates (Freedman et al., 2006; Woloszyn and Sheinberg, 2012; Lim et al., 2015). Bursts of firing in a similar frequency range were also reported in ITC in response to the familiar stimuli. For familiar stimuli, three peaks of clustered APs firing were found in ITC neurons, while novel stimuli elicited only one peak. (Freedman et al., 2006); Alternating familiar stimuli could also evoke periodic responses of ITC neurons, while novel stimuli did not (Meyer et al., 2014).

In our study, the Vm 8-12 Hz band demonstrated a trend toward an increase in magnitude following visual experience, which didn't reach significance. However, the 8-12 Hz band ITPC was significantly increased for the orthogonal direction stimulus in experienced mice. Previous studies also observed elevated 8-12 Hz band power coincident with the rise of 4- 8 Hz power in LFP recordings (Kissinger et al., 2018). Unlike the 5 Hz oscillation, the 8-12 Hz band likely only synchronizes a smaller ensemble of cells rather than the whole local cortical network. Otherwise, one would expect a similar elevation of 8-12 Hz ITPC in response to all directions rather than only the orthogonal direction. Although the 8-12 Hz band activity had been shown to convey feedback processing, especially in primates (van Kerkoerle et al., 2014; Michalareas et al., 2016), the significance of the increased 8-12 Hz band we observed remains to be explored in the future studies.

Neural oscillations have been proposed to provide well-controlled Vm fluctuations and time windows for synaptic plasticity in V1. The bidirectional outcome can strengthen the inputs that arrive at the peak of the oscillation and weaken the inputs that are out of phase (Buzsáki, 2002; Buzsaki and Draguhn, 2004). In our study, we found that the APs shifted toward the rising phase of the oscillation when the stimulus of preferred direction was presented. When the stimulus of the opposite direction was presented, the APs shifted toward the falling phase of the oscillation. The high ITPC in the experienced mice also showed strong phase-locking of single cell Vm. These changes in temporally organized firing activity could promote spike-time dependent plasticity in V1, contributing to further improvements in orientation and direction selectivities and the

reduction of randomness while potentially increasing the encoding precision. More research is required in the future to explore this possibility.

Recent modeling studies basing on primate ITC responses to novel and familiar visual stimuli agree with our findings (Lim et al., 2015; Lim, 2019). Based on the similar effects of visual learning observed in monkey ITC, different roles of synaptic plasticity at the feedforward and recurrent connections have been proposed. The feedforward and recurrent synaptic plasticity together enabled more efficient coding of the stimuli after learning as depression in the feedforward connections led to a decrease in overall activity, while Hebbian-type recurrent synaptic plasticity led to enhanced stimulus selectivity. On the other hand, potentiation in recurrent synapses was required so that stronger positive feedback through potentiation interacts with slow negative feedback such as adaptation and shapes the response dynamics. We modified this model according to the features of a V1 network and used it to reproduce our experimental data. One notable difference from the previous work was an overall increase of low-frequency oscillations across all directions in V1, while the strength of oscillations after learning depends on the preference to the object stimuli in ITC. This difference may arise from the properties of the stimuli and corresponding network architecture such that the response to the preferred and opposite stimuli was correlated through a ring-like network architecture compared to the response to two different object stimuli, and thus, the oscillations were spread across all directional stimuli.

The 5 Hz oscillations we observed in V1 extended for ~500ms to 1s after the stimulus offset. Although the sustained oscillation could be explained by hysteresis in the recurrent dynamics of the local circuits, it is likely other mechanisms are involved as well. The rebound spiking activity caused by Hyperpolarization-activated cyclic nucleotide-gated (HCN) channels could contribute to the excitation required for the oscillation. The feedback connections from higher cortical areas could also be involved in this process. Also, although we assumed that thalamic inputs are not oscillatory, previous experimental works described low-frequency dependent top-down modulation through thalamocortical loops, in particular, in tasks requiring more attention (Fiebelkorn et al., 2019). These possibilities could be explored in future experiments and addressed in a future extension of the model.

2.6 Acknowledgments

We thank Samuel T. Kissinger, Alex Pak, Yu Tang, and Michael Zimmerman for the comments on the manuscript. This work was funded by the National Institute of Mental Health (R01 MH116500). S. Lim was supported by Research Fund for International Young Scientists at the National Natural Science Foundation of China, 31650110468, and S. Lim acknowledges the support of the NYU-ECNU Institute of Brain and Cognitive Science at NYU Shanghai.

2.7 Author contributions

M.G. and A.A.C. designed the study, M.G. performed the experiments and analyzed the data, S.L. developed the computational model, M.G., S.L., and A.A.C. wrote the manuscript.

2.8 Reference

Arenkiel BR, Peca J, Davison IG, Feliciano C, Deisseroth K, Augustine GJ, Ehlers MD, Feng GP (2007) In vivo light-induced activation of neural circuitry in transgenic mice expressing channelrhodopsin-2. Neuron 54:205-218.

Ben-Yishai R, Bar-Or RL, Sompolinsky H (1995) Theory of orientation tuning in visual cortex. Proc Natl Acad Sci U S A 92:3844-3848.

Billeh YN, Cai B, Gratiy SL, Dai K, Iyer R, Gouwens NW, Abbasi-Asl R, Jia XX, Siegle JH, Olsen SR, Koch C, Mihalas S, Arkhipov A (2020) Systematic Integration of Structural and Functional Data into Multi-scale Models of Mouse Primary Visual Cortex. Neuron 106:388-+.

Boudkkazi S, Carlier E, Ankri N, Caillard O, Giraud P, Fronzaroli-Molinieres L, Debanne D (2007) Release-dependent variations in synaptic latency: A putative code for short- and long-term synaptic dynamics. Neuron 56:1048-1060.

Boyden ES, Zhang F, Bamberg E, Nagel G, Deisseroth K (2005) Millisecond-timescale, genetically targeted optical control of neural activity. Nature Neuroscience 8:1263-1268.

Buzsaki G, Draguhn A (2004) Neuronal oscillations in cortical networks. Science 304:1926-1929.

Buzsáki G (2002) Theta Oscillations in the Hippocampus. Neuron 33:325-340.

Chubykin AA, Roach EB, Bear MF, Shuler MG (2013) A cholinergic mechanism for reward timing within primary visual cortex. Neuron 77:723-735.

Cohen MX (2014) Analyzing Neural Time Series Data: Theory and Practice. Iss Clin Cogn Neurop:1-578.

Coleman JE, Nahmani M, Gavornik JP, Haslinger R, Heynen AJ, Erisir A, Bear MF (2010) Rapid structural remodeling of thalamocortical synapses parallels experience-dependent functional plasticity in mouse primary visual cortex. The Journal of neuroscience : the official journal of the Society for Neuroscience 30:9670-9682.

Einstein MC, Polack PO, Tran DT, Golshani P (2017) Visually Evoked 3-5 Hz Membrane Potential Oscillations Reduce the Responsiveness of Visual Cortex Neurons in Awake Behaving Mice. J Neurosci 37:5084-5098.

Ermentrout B (1998) Neural networks as spatio-temporal pattern-forming systems. Rep Prog Phys 61:353-430.
Fiebelkorn IC, Pinsk MA, Kastner S (2019) The mediodorsal pulvinar coordinates the macaque fronto-parietal network during rhythmic spatial attention. Nature Communications 10.
Freedman DJ, Riesenhuber M, Poggio T, Miller EK (2006) Experience-dependent sharpening of visual shape selectivity in inferior temporal cortex. Cereb Cortex 16:1631-1644.
Fuentemilla L, Barnes GR, Duzel E, Levine B (2014) Theta oscillations orchestrate medial temporal lobe and neocortex in remembering autobiographical memories. Neuroimage 85 Pt 2:730-737.
Goltstein PM, Coffey EBJ, Roelfsema PR, Pennartz CMA (2013) In vivo two-photon Ca2+ imaging reveals selective reward effects on stimulus-specific assemblies in mouse visual cortex. The Journal of neuroscience : the official journal of the Society for Neuroscience 33:11540-11555.
Hagglund M, Borgius L, Dougherty KJ, Kiehn O (2010) Activation of groups of excitatory neurons in the mammalian spinal cord or hindbrain evokes locomotion. Nature neuroscience 13:246-252.
Harris KD, Thiele A (2011) Cortical state and attention. Nat Rev Neurosci 12:509-523.
Hubel DH, Wiesel TN (1959) Receptive fields of single neurones in the cat's striate cortex. The Journal of physiology 148:574-591.
Hubel DH, Wiesel TN (1962) Receptive fields, binocular interaction and functional architecture in the cat's visual cortex. The Journal of physiology 160:106-154.
Katz Y, Yizhar O, Staiger J, Lampl I (2013) Optopatcher—An electrode holder for simultaneous intracellular patch-clamp recording and optical manipulation. Journal of Neuroscience Methods 214:113-117.
Khan AG, Poort J, Chadwick A, Blot A, Sahani M, Mrsic-Flogel TD, Hofer SB (2018) Distinct learning-induced changes in stimulus selectivity and interactions of GABAergic interneuron classes in visual cortex. Nat Neurosci 21:851-859.
Kissinger ST, Pak A, Tang Y, Masmanidis SC, Chubykin AA (2018) Oscillatory Encoding of Visual Stimulus Familiarity. The Journal of Neuroscience 38:6223-6240.
Kissinger ST, Wu QY, Quinn CJ, Anderson AK, Pak A, Chubykin AA (2020) Visual Experience-Dependent Oscillations and Underlying Circuit Connectivity Changes Are Impaired in Fmr1 KO Mice. Cell Rep 31.
Ko H, Hofer SB, Pichler B, Buchanan KA, Sjostrom PJ, Mrsic-Flogel TD (2011) Functional specificity of local synaptic connections in neocortical networks. Nature 473:87-91.
Kobatake E, Wang G, Tanaka K (1998) Effects of shape-discrimination training on the selectivity of inferotemporal cells in adult monkeys. J Neurophysiol 80:324-330.
Lee H, Simpson GV, Logothetis NK, Rainer G (2005) Phase locking of single neuron activity to theta oscillations during working memory in monkey extrastriate visual cortex. Neuron 45:147-156.
Lee SH, Kwan AC, Zhang S, Phoumthipphavong V, Flannery JG, Masmanidis SC, Taniguchi H, Huang ZJ, Zhang F, Boyden ES, Deisseroth K, Dan Y (2012) Activation of specific interneurons improves V1 feature selectivity and visual perception. Nature 488:379-383.
Levy JM, Zold CL, Namboodiri VMK, Hussain Shuler MG (2017) The Timing of Reward-Seeking Action Tracks Visually Cued Theta Oscillations in Primary Visual Cortex. J Neurosci 37:10408-10420.

Liebe S, Hoerzer GM, Logothetis NK, Rainer G (2012) Theta coupling between V4 and prefrontal cortex predicts visual short-term memory performance. Nat Neurosci 15:456-462, S451-452.
Lien AD, Scanziani M (2018) Cortical direction selectivity emerges at convergence of thalamic synapses. Nature 558:80-+.
Lim S (2019) Mechanisms underlying sharpening of visual response dynamics with familiarity. Elife 8.
Lim S, McKee JL, Woloszyn L, Amit Y, Freedman DJ, Sheinberg DL, Brunel N (2015) Inferring learning rules from distributions of firing rates in cortical neurons. Nat Neurosci 18:1804-1810.
Luo H, Poeppel D (2007) Phase Patterns of Neuronal Responses Reliably Discriminate Speech in Human Auditory Cortex. Neuron 54:1001-1010.
Meyer T, Walker C, Cho RY, Olson CR (2014) Image familiarization sharpens response dynamics of neurons in inferotemporal cortex. Nat Neurosci 17:1388-1394.
Michalareas G, Vezoli J, van Pelt S, Schoffelen JM, Kennedy H, Fries P (2016) Alpha-Beta and Gamma Rhythms Subserve Feedback and Feedforward Influences among Human Visual Cortical Areas. Neuron 89:384-397.
Niell CM, Stryker MP (2010) Modulation of Visual Responses by Behavioral State in Mouse Visual Cortex. Neuron 65:472-479.
Peelle JE, Gross J, Davis MH (2013) Phase-locked responses to speech in human auditory cortex are enhanced during comprehension. Cereb Cortex 23:1378-1387.
Poort J, Khan AG, Pachitariu M, Nemri A, Orsolic I, Krupic J, Bauza M, Sahani M, Keller GB, Mrsic-Flogel TD, Hofer SB (2015) Learning Enhances Sensory and Multiple Non-sensory Representations in Primary Visual Cortex. Neuron 86:1478-1490.
Reimer J, Froudarakis E, Cadwell CR, Yatsenko D, Denfield GH, Tolias AS (2014) Pupil Fluctuations Track Fast Switching of Cortical States during Quiet Wakefulness. Neuron 84:355-362.
Sauseng P, Klimesch W, Heise KF, Gruber WR, Holz E, Karim AA, Glennon M, Gerloff C, Birbaumer N, Hummel FC (2009) Brain oscillatory substrates of visual short-term memory capacity. Curr Biol 19:1846-1852.
Schoups A, Vogels R, Qian N, Orban G (2001) Practising orientation identification improves orientation coding in V1 neurons. Nature 412:549-553.
Shuler MG, Bear MF (2006) Reward timing in the primary visual cortex. Science 311:1606-1609.
van Kerkoerle T, Self MW, Dagnino B, Gariel-Mathis MA, Poort J, van der Togt C, Roelfsema PR (2014) Alpha and gamma oscillations characterize feedback and feedforward processing in monkey visual cortex. Proc Natl Acad Sci U S A 111:14332-14341.
Woloszyn L, Sheinberg DL (2012) Effects of long-term visual experience on responses of distinct classes of single units in inferior temporal cortex. Neuron 74:193-205.
Wu Q, Chubykin AA (2017) Application of Automated Image-guided Patch Clamp for the Study of Neurons in Brain Slices. J Vis Exp.
Wu Q, Kolb I, Callahan BM, Su Z, Stoy W, Kodandaramaiah SB, Neve R, Zeng H, Boyden ES, Forest CR, Chubykin AA (2016) Integration of autopatching with automated pipette and cell detection in vitro. J Neurophysiol 116:1564-1578.
Zold CL, Hussain Shuler MG (2015) Theta Oscillations in Visual Cortex Emerge with Experience to Convey Expected Reward Time and Experienced Reward Rate. J Neurosci 35:9603-9614.

CHAPTER 3. RESTORATION OF VISUAL FUNCTION AND CORTICAL CONNECTIVITY AFTER ISCHEMIC INJURY THROUGH NEUROD1-MEDIATED GENE THERAPY

Adopted from: Tang Y[†], Wu Q[†], Gao M[†], Ryu E, Pei Z, Kissinger ST, Chen Y, Rao AK, Xiang Z, Wang T, Li W, Chen G, Chubykin AA. Restoration of Visual Function and Cortical Connectivity After Ischemic Injury Through NeuroD1-Mediated Gene Therapy. Front Cell Dev Biol. 2021 Aug 18;9:720078. doi: 10.3389/fcell.2021.720078. PMID: 34490268; PMCID: PMC8416524.

[†]These authors share first authorship.

3.1 Abstract

Neural circuits underlying brain functions are vulnerable to damage, including ischemic injury, leading to neuronal loss and gliosis. Recent technology of direct conversion of endogenous astrocytes into neurons in situ can simultaneously replenish the neuronal population and reverse the glial scar. However, whether these newly reprogrammed neurons undergo normal development, integrate into the existing neuronal circuit, and acquire functional properties specific for this circuit is not known. We investigated the effect of NeuroD1-mediated in vivo direct reprogramming on visual cortical circuit integration and functional recovery in a mouse model of ischemic injury. After performing electrophysiological extracellular recordings and two-photon calcium imaging of reprogrammed cells in vivo and mapping the synaptic connections formed onto these cells ex vivo, we discovered that NeuroD1 reprogrammed neurons were integrated into the cortical microcircuit and acquired direct visual responses. Furthermore, following visual experience, the reprogrammed neurons demonstrated maturation of orientation selectivity and functional connectivity. Our results show that NeuroD1-reprogrammed neurons can successfully develop and integrate into the visual cortical circuit leading to vision recovery after ischemic injury.

3.2 Introduction

Functional circuit impairment associated with neuronal loss is commonly seen in patients with brain injuries, such as ischemia. However, the adult brain has a limited capacity to generate neurons, and it remains a challenge to functionally incorporate neurons into the local circuits. Several strategies have shown the capability to induce neurogenesis and lead to some behavioral recovery. One promising approach is to transplant stem cell-derived neurons or neural progenitor

cells (Tornero et al., 2013;Michelsen et al., 2015;Falkner et al., 2016;Somaa et al., 2017). Yet, there are concerns about graft rejection and tumorigenicity of the transplanted cells (Erdo et al., 2003;Marei et al., 2018). Meanwhile, progress has been made in reprogramming non-neuronal cells, such as fibroblast and glial cells, into neurons directly by expressing transcription factors (Marro et al., 2011;Yang et al., 2011;Grande et al., 2013;Niu et al., 2013;Blanchard et al., 2014;Heinrich et al., 2014;Torper et al., 2015;Mattugini et al., 2019;Nolbrant et al., 2020). Brain injuries, including ischemic injury, trigger re-activation and proliferation of astrocytes around the injury site. Although the initial stage of gliosis may be beneficial to confining the injury, glial scarring in the later stage is detrimental to axonal regeneration, neural circuit rewiring, and functional recovery (Fitch and Silver, 2008;Kawano et al., 2012). One transcription factor NeuroD1, which has been demonstrated to convert human ESCs and iPSCs into neurons in vitro (Zhang et al., 2013), also showed great efficacy in converting astrocytes to neurons in situ, bypassing the pluripotent and proliferating stem cell stage (Guo et al., 2014;Chen et al., 2015;Li and Chen, 2016;Brulet et al., 2017;Chen et al., 2020), and a recent study confirmed that the converted cells originated from astrocytes using lineage tracing labeling (Xiang et al., 2021). It has been shown that NeuroD1-mediated astrocyte-to-neuron conversion supported behavioral function recovery following ischemic injury in the motor cortex and the converted neurons form structural connections with thalamic neurons (Chen et al., 2020;Ge et al., 2020). Despite the demonstration of the behavior recovery, whether the newly transformed neurons integrate into the local circuits and perform appropriate functions is less clear.

Several questions remain unanswered: do the reprogrammed cells become integrated into the functional circuit in brain regions that have complex circuit structures, like cortices? Do they gain the functional properties of a typical neuron and become part of the specific circuit? Do the reprogrammed cells undergo a classical developmental path of regular neurons, or is their developmental trajectory different? Finally, how safe is this process of converting a non-neuronal cell into a neuron? Do these cells stay neurons, or do they gain other potentially aberrant cellular properties?

Answering these questions is critical for the development of new regenerative therapies for brain injuries. We have decided to answer some of these questions using the mouse primary visual cortex, which provides unique advantages as a model system. It is easily accessible for in vivo electrophysiological recordings and calcium imaging in awake mice. It is responsive to visual

stimulation, providing an opportunity to characterize cortical cells' functional properties using quantitative visual tests and various stimuli.

To examine the functional recovery of the visual cortex after ischemic injury, we directly measured neuronal activity and response selectivity in the NeuroD1-treated visual cortex in awake mice and mapped the connectivity of the individual newly reprogrammed neurons in ex vivo brain slices. Visual response and circuit connectivity strength were characterized longitudinally after reprogramming, revealing local circuitry remodeling and visual response recovery. Furthermore, the reprogrammed cells' orientation selectivity improved over time as assayed by two-photon calcium imaging and extracellular recordings at different developmental stages following reprogramming. These findings suggest that NeuroD1-mediated reprogramming of astrocytes into neurons leads to neuronal regeneration and functional recovery of vision after ischemic injury.

3.3 Materials and Methods

3.3.1 Animals

Wild type male and female C57BL/6 mice (Jackson Laboratory and Purdue University Transgenic Mouse Core Facility, postnatal day 34-90) were used for in vivo extracellular recording experiments. Thy1-ChR2-YFP line 18 (B6.Cg-Tg(Thy1-COP4/EYFP)18Gfng/J, JAX stock #007612) was used for ex vivo cortical slices preparation and whole cell patch-clamp experiments. All animals were housed in 12-hr light/dark cycle with ad libitum access to rodent chow food and water. All experimental animal use was approved by the Purdue University animal care and use committee and followed guidance issued by the National Institutes of Health.

3.3.2 Surgery, ischemic injury induction, viral injections, and cranial window

Mice were anesthetized during all surgical procedures with inhaled isoflurane (5% for initial induction and 1.5% for maintaining anesthesia, carrier gas was room air, SomnoSuite system). Deep anesthesia was confirmed by no response to toe/tail pinch. The skin over the skull was removed, and the skull over the cortices was exposed. The craniotomy was made first by thinning a small area of the skull about 0.5mm diameter at the injection site with a drill. Then, a tiny gap at the center of the hole for inserting the micro-injection pipette was opened using a sterile needle. To induce focal ischemia, a total volume of 1µl of 4µg/µl endothelin-1 (ET-1, Sigma) was injected

into V1. ET-1 was dissolved in filter-sterilized pure water to make a stock solution which was stored at -80°C and diluted to the final concentration with filter-sterilized artificial cerebral spinal fluid (ACSF) before each injection. ET-1 solution was injected at two depths, 700μm and 300μm below the brain surface, 500nl per depth at 100nl/min rate using a microinjector (NanoJect II or NanoJect III, Drummond Scientific). For sham injections, 1μl of ACSF was injected at the same speed and depths. For mice used in extracellular recording experiments, a head post (or head plate for 2 photon imaging) was adhered to the skull at 4mm anterior to bregma, and a gold-plated grounding pin (Parkell) was installed 1mm anterior to bregma by inserting the sharp end through the skull into the midline space (but not in the brain tissue). Following the procedures, acrylic dental cement (Metabond, C&B) was applied to the exposed skull to create a protective hard cap and to secure the head post and the grounding pin. Ground pin installation were omitted for animals for *ex vivo* brain slice preparation and 2 photon calcium imaging. 8 to 10 days after ET-1 injections, two adeno-associated viruses (AAV9), one carrying FLEX-NeuroD1-mCherry and the second carrying GFAP::Cre were injected together (10:1 ratio, 1ul total volume, injected at the same depths and speed as ET-1 injection) through the same craniotomy. Coordinates used for primary visual cortices injections were (relative to lambda): 0.8 mm anterior, ±3.0 mm lateral for animals used in extracellular recordings; or 0.8mm anterior, ±2.8 mm lateral for animals used in *ex vivo* slice recordings. For the 2 photon calcium imaging and optotagging experiments, ET-1 was injected in both hemispheres as described earlier. 8-10 days after ET-1 injection, AAV9-CAG::GFAP-Cre, AAV9-CAG::FLEX-NeuroD1-mCherry, and AAV9-CAG::FLEX-GCaMP6s (for 2 photon calcium imaging, Addgene, 100842) or AAV5-DIO-ChR2-eYFP (for optotagging, Addgene, 20298) were injected together (2:10:10 ratio) into both hemispheres at 700um and 300um below the brain surface (500nl per depth, speed 1nl/s). AAV9-syn-jGCaMP7s (Addgene, 104487) was injected alone into healthy mouse V1 as the healthy control for calcium imaging experiments. Carprofen (5mg/kg) and enrofloxacin (5mg/kg) was subcutaneously injected into mice daily after the viral injection to minimize inflammatory responses. Three days after the viral injection, a 2mm diameter cranial window was made at the injection site using a fine dental drill. The window was then filled with sterile ACSF and covered by a 5mm diameter glass cover. Metabond was used to seal the glass window.

3.3.3 In vivo extracellular recording preparation

Mice were habituated to the head-fixed recording setup for at least 4 days, 90 minutes per day, prior to recordings. Mice were head-fixed, and their bodies were loosely restrained in a tube on a platform. A monitor (21.5" ViewSonic VX2252MH, or 25" Alienware AW2518Hf) was positioned 16.5cm in front of the platform showing a gray screen during habituation sessions. On recording days, small cranial windows (~1mm2) were made at the injection sites while mice were anesthetized by isoflurane inhalation. Mice were placed on the head-fixed setup after craniotomies, and a silicon probe was inserted into the cranial window. For optotagging experiments, an optical fiber (Thorlabs, 0.39NA TECS hard-clad, multimode, step-index fibers, FT200EMT) connected to a blue light laser (OEM laser, 100mW 473nm DPSS laser system) was positioned right above the brain surface as adjacent to the recording probe insertion site as possible. Recordings started 30 minutes after probe insertion to allow for recovery from anesthesia and tissue settling. Filter-sterilized ACSF was added on top of the exposed brain surface to prevent desiccation from dehydration.

3.3.4 Visual stimulation and in vivo optogenetic stimulation

All visual stimuli were generated using PsychoPy (Peirce, 2007). The full-field gray screen was used for habituation (mean luminance 73 cd/m2). In one stimulus recordings, sinusoidal drifting gratings (0.04 cycles per degree, drifting at 2Hz, oriented 30 degrees to the vertical direction) were presented for 20 trials. In each trial, the stimulus was presented for 0.2s, preceded by 0.5 s gray screen, followed by 5-6s gray screen inter-trial interval (Fig. 2A). For direction tuning recordings, sinusoidal drifting gratings (0.04 cycles per degree, drifting at 1 Hz, oriented 0, 30, 60, 90, 120, and 150 degrees) were pseudo-randomly presented for 60 trials. Within each trial, the stimulus was presented for 1s, preceded by 0.5 s gray screen, followed by 5-6s inter-trial interval (Fig. 3A). For optogenetics experiments, light stimulation was applied after all visual stimulation experiments to identify cells that co-express NeuroD1 and ChR2. 500ms light pulses (5-10mW measured at the fiber tip) were applied for 20 trials.

3.3.5 Extracellular recording data acquisition and analysis

64-channel silicon probes (Shobe et al., 2015) were used for all recordings. Raw data were digitized at 30kHz and acquired through an OpenEphys acquisition board (Siegle et al., 2017). Local field potentials were obtained by band-pass filtering the raw data between 0 and 300Hz with an additional 60-Hz notch filter to attenuate electrical noise. The channels within the depth range of layer 4 (300 to 500μm below the brain surface) that showed the first strongest negative response to visual stimulation were used for visually evoked potential (VEP) analysis. The most negative value within the visual stimulation time window was used as the VEP amplitude. Time-frequency analysis of LFP was performed by using a series of complex wavelets to extract power and phase at each sample point. Band powers were calculated by averaging powers within 500ms after the visual stimulation onset.

Spikes were clustered into units using Kilosort (Pachitariu et al., 2016a). Units were then manually inspected in Phy (Rossant et al., 2016) template graphical user interface (GUI) to remove units that have noise-like waveforms (artifact-like or have no clear refractory period). Single units were classified as regular-spiking (RS), fast-spiking (FS), and unclassified (UN) units, based on their averaged template waveforms. Units that have averaged template waveform with trough-to-peak duration less than 0.45ms and spike width less than 1ms were classified as putative FS units. Units that had template waveform with trough-to-peak duration more than 0.45ms and spike width more than 1ms were classified as RS units. Units that did not satisfy either criterion were classified as UN units. Spike width was calculated by inverse peak frequency of the spike spectrum (Stark et al., 2013). Peri-stimulus time histograms (PSTHs) of single unit activities were computed using 10ms bins and smoothed with a Gaussian Kernel (width=100ms). Z-scores of single unit firing rate (FR) were calculated by normalizing FR to the mean FR across the duration of each trial (z = (FR-mean FR)/standard deviation of FR). Mean FR within the visual stimulation time window was used as the response to each direction. FR at each orientation was obtained by averaging the FR at the same orientation of two directions. Tuning curves for each group were obtained by fitting unit averaged FR at 6 orientation to Gaussian functions or by interpolating a cubic function. One minus direction circular variance (1-DCV) was calculated using $\left|\frac{\sum_k R(\theta_k)\exp(i\theta_k)}{\sum_k R(\theta_k)}\right|$, and one minus orientation circular variance (1-CV) was calculated using $\left|\frac{\sum_k R(\theta_k)\exp(2i\theta_k)}{\sum_k R(\theta_k)}\right|$, where θ_k was the

direction k (0-2π) or orientation k (0-π) in radians, and R(θ_k) was the mean firing rate within the stimulus time window (Mazurek et al., 2014).

3.3.6 Two photon calcium imaging data acquisition and analysis

Two photon calcium imaging was performed using a Nikon A1R-MP-HD multiphoton microscope with a 16× 0.8 NA water-dipping objective lens (Nikon LWD 16X W) and dual Coherent IR lasers (Chameleon Discovery). Awake mice were head fixed under the microscope, and the image was acquired through the cranial window. The imaged area was around 350 μmx350 μm, and the images were acquired at 512x512 pixels. The GCaMP6s signals were excited at 890 nm, and were acquired by a 4-channel episcopic GaAsP Non-Descanned Detector with a resonant mode at 30 fps. During the time series image acquisition, sinusoidal drifting gratings of 12 directions (5s for each direction, interleaved by 10s gray screens at the same luminance as the stimuli) were presented for 12 trials. After the calcium imaging, the NeuroD1-mCherry signal of the same image plane was acquired with galvanometer mode.

Time series calcium data were processed using Suite2P (Pachitariu et al., 2016b) with non-rigid mode allowing for 10% X-Y axial movements. ROIs were first extracted automatically and then were manually inspected to remove non-cell-like ROIs. To minimize signal contamination by surrounding cells and neuropil, 0.7 times of the spatially averaged neuropil's signal was subtracted from the ROI (Chen et al., 2013). The slow fluctuation was removed by subtracting means of 100s running windows from the signal. The relative calcium signal change was calculated as the ratio of fluorescence change to 2s baseline fluorescence (Δf/f0). The response latency was measured as the duration between the stimulus onset to the time point when Δf/f0 was higher than 1.675 times of baseline standard deviation. To take astrocyte visual response into account, two response time windows were defined. One is 5s duration from the stimulus onset (for neurons), and the other is 5s duration from 3s post- stimulus onset (for astrocytes). Temporally averaged Δf/f0 within these two time windows that were significantly higher than baseline (Wilcoxon signed-rank test, $p<0.05$) and has a response latency that was less than 8s were considered as visual responses. Cells that respond to at least one direction were used for further analyses. Visually evoked response latency of a cell was defined as the minimal latency among latencies of all directions. The circular orientation-selective index (1-CV) and the circular direction-selective index (1-DCV) were calculated as described earlier.

3.3.7 Acute brain slices preparation

Mice were anesthetized with an intraperitoneal (IP) injection of a cocktail of ketamine (100mg/kg body weight) and xylazine (16mg/kg body weight) diluted in sterile saline. Deep anesthesia was confirmed with no reflex to toe/tail pinch. For animals that were at the age of 55 days or younger, trans-cardiac perfusion was conducted using ice-cold High Sucrose Dissection Buffer (HSDB) containing (in mM) 75 sucrose, 10 glucose, 87 NaCl, 2.5 KCl, 1.25 NaH2PO4, 25 NaHCO3, 0.5 CaCl2, 7 MgCl2, and 1.3 ascorbic acid. Following perfusion, the brain was quickly dissected out of the skull, and the visual cortex was cut on a vibratome (VT1000, Leica) into slices at 300µm thickness in ice-cold HSDB. Brain slices were then carefully transferred into normal Artificial Cerebral Spinal Fluid (ACSF) containing (in mM) 124 NaCl, 3.5 KCl, 1 CaCl2, 0.8 MgCl2, 1.23 NaH2PO4, 26 NaHCO3, and 10 glucose. The slices were first incubated at 32°C in ACSF for 30min then at room temperature (around 25°C) for 1 to 6 hours before recording. For animals that were older than 55 days, trans-cardiac perfusion was conducted using ice-cold N-methyl-D-glucamine (NMDG) ACSF containing (in mM) 92 mM NMDG, 2.5 mM KCl, 1.25 mM NaH2PO4, 30 mM NaHCO3, 20 mM HEPES, 25 mM glucose, 2 mM thiourea, 5 mM Na-ascorbate, 3 mM Na-pyruvate, 0.5 mM CaCl2 and 10 mM MgCl2. Dissection and slicing were conducted in the same manner as for young animals but in ice-cold NMDG ACSF. Brain slices were then recovered in NMDG ACSF at 32°C for 4 to 7 min depending on the animal age, then in HEPES ACSF containing (in mM) 92 mM NaCl, 2.5 mM KCl, 1.25 mM NaH2PO4, 30 mM NaHCO3, 20 mM HEPES, 25 mM glucose, 2 mM thiourea, 5 mM Na-ascorbate, 3 mM Na-pyruvate, 2 mM CaCl2 and 2 mM MgCl2 at room temperature for at least 2h before recording. All physiological solutions were continuously aerated with carbogen gas (95% O2 5% CO2) to maintain pH (7.3-7.4) and oxygen saturation. Brain slices were kept alive for up to 7h after cutting and each recorded slice was used for up to 1.5h.

3.3.8 Whole-cell patch clamp recordings

Patch-clamp recordings were conducted using a commercial slice physiology rig (SliceScope Pro 1000, Scientifica). Patch pipettes were pulled using a standard Flaming-Brown type puller (Sutter Instruments P97) from filamented borosilicate glass capillaries (BF150-86-10, Sutter Instruments). The pipette internal solution contained (in mM) 20 KCl, 100 K-gluconate, 10

HEPES, 4 MgATP, 0.3 Na2GTP, and 7 phosphocreatine, with pH adjusted to 7.4 and osmolarity adjusted to 300 mOsm. In some experiments, a small amount of 4% w/v Alexa FluorTM 647 Hydrazide (A20502, ThermoFisher Scientific) dissolved in internal solution was back-loaded to the glass pipette through capillary force before loading the regular internal solution to label the patched cell. Pipette impedance was in the range of 3.5 to 7.9MΩ when filled with internal solution and submerged in ACSF. Brain slices were placed in a recording chamber continuously perfused with oxygenated ACSF and heated to 30-32°C. Cells were visualized with infrared illumination through differential interface contrast (DIC) optics and recorded with a charge-coupled device (CCD) camera. Signals were amplified using a Multiclamp 700B amplifier (Molecular Devices) and digitized using Digidata 1550A (Molecular Devices) at 20kHz and low-pass filtered at 10kHz. Recorded data were analyzed using custom-written Python scripts (detailed statistical tests see "Experimental design and statistical analysis"). For experiments during where cells were filled with fluorescent dyes, the slices were fixed with 4% paraformaldehyde (PFA) for 30min-1h and mounted onto glass slides for imaging.

3.3.9 Channelrhodopsin-assisted circuit mapping (CRACM)

We used Thy1-ChR2-YFP line 18 (B6.Cg-Tg(Thy1-COP4/EYFP)18Gfng/J, JAX stock #007612) which expressed Channelrhodopsin-2 (ChR2) sparsely in layer 5 pyramidal cells in the cortex (Arenkiel et al., 2007). To control for intrinsic synaptic strength difference in different projections, only layer 4 neurons were patched, only L5 to L4 projections were compared. L4 cells were identified by the morphology and relative location in the brain slice (mid-point from pia to white matter). Light stimulation was generated with an LED light source (High-Power LED Collimator Source, 470nm, 50W, Mightex) and delivered through a patterned illuminator (Polygon 400, Mightex) (Avants et al., 2015). A 10 by 10 grid covering a 670µm by 670µm square area was superimposed on the primary visual cortical slice, which spans the top border of L2/3 to the lower border of L5 under 10x objective. Each pixel was stimulated for 10ms, following a pseudo-random sequence with 2s inter-stimulus interval. Cells were held at -70mV in voltage-clamp mode during CRACM recordings. The LED and patterned illuminator were controlled by the manufacturer's software, and stimulation and recording were synchronized by the Digidata. CRACM heatmaps were plotted from light-induced EPSC amplitudes at each pixel.

3.3.10 Histology and immunohistochemistry (IHC)

Mice were anesthetized with 100mg/kg ketamine and 16mg/kg xylazine through IP injection before trans-cardiac perfusion. Deep anesthesia was confirmed with no reflex to toe/tail pinch. The thorax and abdomen were opened. A needle was inserted into the left ventricle of the heart, and a small incision was made in the right atrium. Mice were first perfused with 1x phosphate-buffered saline (PBS, 15 to 20ml) until the liver cleared, then with 4% paraformaldehyde (PFA, 10 to 15ml) for fixation. Mouse brains were post-fixed in 4% PFA for an additional 12-36hr before histology. Fixed brain tissue was sliced using a vibrating microtome (1000 Plus, TPI Vibratome) at 50μm thickness. When IHC staining was unnecessary, slides were made directly by mounting the slices with anti-fade mounting medium containing 0.2% n-propyl gallate. When IHC is necessary, the 50μm slices were stained free-floating in 24-well tissue culture plates. They were first blocked and membrane permeabilized in 5% bovine serum albumin (BSA) and 0.1%-2% Triton X 100 (TX 100, Sigma) in PBS at room temperature for 0.5-1 hour. Then, the slices were incubated with the primary antibody in 0.1% TX 100 for 36 to 48h at 4°C followed by the secondary antibody for 1 to 2h at room temperature. Slices are washed in PBS in between antibody incubations. Slices were counterstained with DAPI when necessary. For Ctip2 and Satb2 staining, slices were treated in 80°C sodium citritate buffer for 20 minutes before blocking. The slices were mounted using the same method described above. Antibodies used are: Anti-Glial Fibrillary Acidic Protein Antibody (AB5541, Millipore Sigma), Anti-NeuN Antibody (ABN78, Millipore Sigma), Anti-Satb2 Antibody (ab51502, abcam), Anti-GABA Antibody (A2052, Sigma), Anti-Cux1 Antibody (11733-1-AP, proteintech), Anti-Ctip2 Antibody (ab18465, Abcam), Anti-Tbr1 (AB10554, Millipore Sigma), Alexa Fluor® 488 AffiniPure Donkey Anti-Rabbit IgG (H+L) (Code: 711-545-152, Jackson ImmunoResearch), Alexa Fluor® 647 AffiniPure Donkey Anti-Rat IgG (H+L) (Code: 712-605-150, Jackson ImmunoResearch), and Alexa Fluor® 647 AffiniPure Goat Anti-Chicken IgY (IgG) (H+L) (Code: 103-605-155, Jackson ImmunoResearch). Brain slices were imaged under a confocal microscope (Zeiss LSM710). Neurite tracing and reconstruction was conducted using Fiji/ImageJ. For quantification of marker positive reprogrammed cells, ROIs were identified on the mCherry channel, and the intensities of the markers were measured within ROI. Normalized intensity above threshold (1.5 times of median intensity of each slice for) is considered as positive marker cell.

3.3.11 Experimental Design and Statistical Analysis

Experimental groups and controls are described in detail with the results. Data were analyzed using custom-written scripts in Python. Data normality was tested using the Shapiro-Wilk normality test and statistically tested using the Scipy, Statsmodels, or Pingouin (Vallat, 2018) statistical packages. For normally distributed data, a Student's t-test was used for pair-wise comparisons, or ANOVA was used for comparison among multiple groups. For non-normally distributed data, non-parametric tests were used. Mann-Whitney U test was used for comparing two distributions with similar shape; Kruskal-Wallis H-test was used for comparing multiple distributions with similar shape, and the Kolmogorov-Smirnov test was used for comparing two distributions with different shapes. Group distributions of VEP amplitudes, LFP frequency band powers, unit firing rate z-scores, EPSCs amplitude were compared using non-parametric Mann-Whitney U test with effect size reported. Unit counts were compared using Kruskal-Wallis H-test. 1-DCV and 1-CV cumulative distributions were compared using the two-sample Kolmogorov-Smirnov test. When comparing multiple normal distributions or converted normal distributions of EPSCs amplitude, one-way or two-way ANOVA was conducted, followed by Tukey's post-hoc multiple comparisons test. For averaged EPSCs data, either Box-Cox or log transformation was applied to get normal distributions (Young 3 weeks: Box-Cox, lambda=-0.245; Young 6 weeks: Box-Cox, lambda=-0.836; Old 6 weeks: log10 transformation). See the results section for the specific test used in each case and the test statistic values.

3.4 Results

3.4.1 NeuroD1 efficiently converted astrocytes into neurons that acquired cortical neuron identity in the visual cortex

To demonstrate the effects of in vivo direct reprogramming on visual function following cortical ischemic injury, we assessed visual responses using in vivo extracellular recordings in awake mice. To measure how newly converted neurons integrated into the local cortical circuits, we used ex vivo channelrhodopsin-assisted circuit mapping (CRACM) in acute brain slices (Figure 3.1A). At nine days after endothelin-1 (ET-1) injection, robust gliosis and neuronal loss were confirmed by astrocyte marker GFAP and neuronal marker NeuN staining, which showed a significant increase in astrocyte/neuron ratio (Figure 3.1B and C). The induced glial scar did not

resolve if no treatment was applied (Figure 3.2 A middle). After the glial scar was formed, we delivered the Cre-dependent reprogramming gene NeuroD1 (CAG::FLEX-NeuroD1-mCherry) along with the Cre-recombinase gene under the GFAP promoter (GFAP::Cre) targeting astrocytes using adeno-associated virus (AAV9). The astrocytes underwent a transition to neurons, where they temporarily expressed both GFAP and NeuN (Figure 3.1D, Figure 3.2B middle). The fully reprogrammed neurons only expressed NeuN, but not GFAP, which was detected as early as ten days after the viral injection (Figure 3.1E yellow arrows). Three weeks after the viral injection, more than 50% of NeuroD1-mCherry positive (NeuroD1-mCherry+) cells expressed only NeuN but not GFAP (Figure 3.1F left). The exogenous NeuroD1 expression was significantly higher compared to the endogenous expression (Figure 3.3). The majority of NeuroD1-mCherry+ expressed excitatory neuronal marker Satb2, and a small percentage expressed GABAergic cell marker (Figure 3.1F right). Furthermore, we tested whether the reprogrammed neurons acquired cortical neuron identity and whether they formed layer structure by immunostaining a cortical neuronal marker Tbr1, a superficial layer marker Cux1, and a deep layer marker Ctip2. At both 3 and 6 weeks after the viral injection, more than 50% of NeuroD1-mCherry+ cells expressed Tbr1 (Figure 3.4A and C), indicating their cortical neuron identity. The NeuroD1-mCherry+ cells within the superficial and deep layers were immunopositive for Cux1 and Ctip2, respectively. The percentage of Cux1+/NeuroD1+ cells was higher in the superficial layers, lower in the deep layers, compared to Ctip2+/NeuroD1+ cells (Figure 3.4D-I). These results demonstrate that NeuroD1 efficiently converts astrocytes to neurons, which acquire cortical neuron identities and form cortical layer structure, allowing for functional circuit integration.

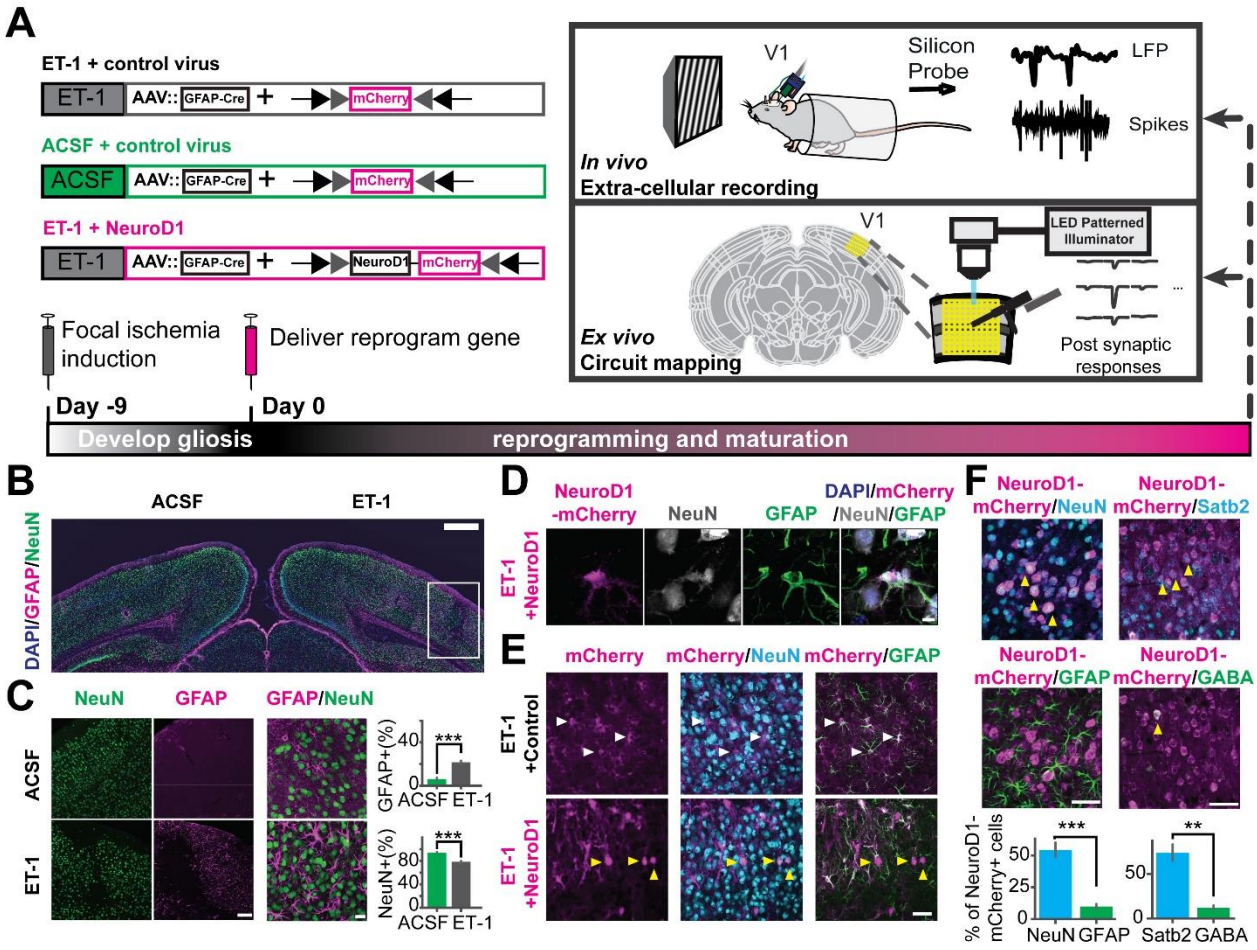

Figure 3.1 Focal ischemic injury model and in vivo direct reprogramming in the primary visual cortex. A. The schedule to induce focal ischemia by endothelin-1 (ET-1) injection and to reprogram astrocytes into neurons by injection of AAV-GFAP::Cre with AAV-FLEX-NeuroD1-mCherry (or with AAV-FLEX-mCherry as control). Following reprogramming, visual responses and local circuit connectivity of the primary visual cortex (V1) were assessed by in vivo extracellular recordings and ex vivo Channelrhodopsin-Assisted Circuit Mapping (CRACM). B, Gliosis (GFAP, magenta) and neuronal loss (NeuN, green) at 9 days after 4ug/ul ET-1 injection in the visual cortex. The box indicates injury site with gliosis and neuronal loss. Scale: 500µm .C, Localized neuronal loss and gliosis at 9 days after 4ug/ul ET-1 injection. Scaleleft: 50µm. Scaleright: 20µm. Right: Quantification of the percentages of GFAP-positive cells (top) and NeuN-positive cells (bottom). NACSF=NET-1= 3 mice, 9 slices. p=4.12x10-4, Mann-Whitney U test. D, An example of NeuroD1-mCherry-positive cell undergoing a transition stage at 10 days after NeuroD1 delivery, expressing both GFAP and NeuN. Scale: 5µm. E, mCherry positive cells co-stained¬ with NeuN and GFAP at 10 days after viral injection. White arrows pointing to GFAP positive and NeuN negative cells. Yellow arrows pointing to GFAP negative and NeuN positive cells. Scale: 50µm. F, NeuroD1-positive cells stained with NeuN, GFAP, Satb2, and GABA at 3 weeks after NeuroD1 delivery. Scale: 50µm. Bottom: Quantification of the ratios of marker positive cells. NNeuN/GFAP= 3 mice, 9 slices. p=9.01x10-4, Mann-Whitney U test. NSatb2/GABA= 2 mice, 6 slices. p=5.08x10-3, Mann-Whitney U test.**-p<0.01, ***-p<0.001. Data are represented as mean ± SEM.

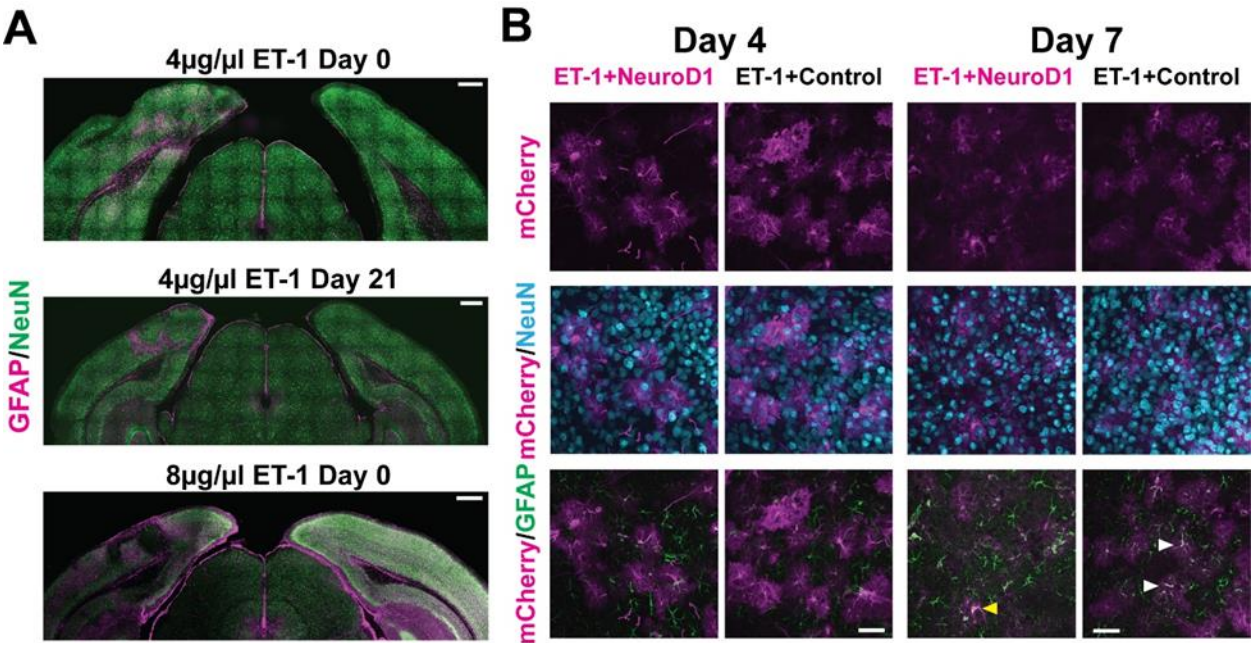

Figure 3.2 Gliosis and neuronal loss in ET-1 injected visual cortex and cell conversion following in vivo direct reprogramming in the primary visual cortex. A. Gliosis (GFAP, magenta) and neuronal loss (NeuN, green) at 9 days after 4ug/ul ET-1 injection (top left hemisphere). Persisted gliosis after 4 weeks (middle left hemisphere). Larger tissue damage induced by 8ug/ul ET-1 (bottom left hemisphere). ACSF injected control (right hemispheres). Scale: 500µm. B. mCherry positive cells co-stained with NeuN in the reprogrammed group and GFAP in control at 4 and 7 days after viral injection. Arrows pointing to double positive cells. Scale: 50µm.

Figure 3.3 Comparison of endogenous NeuroD1 expression level versus AAV overexpressed NeuroD1 after astrocyte-to-neuron conversion. A and B. Representative images illustrating that in the control mCherry group, the endogenous neurons (labeled by NeuN) rarely showed detectable level of NeuroD1 expression in the mouse cortex. Scale bar for panel A, 100 mm. Panel B shows the enlarged box area in panel A. Scale bar for panel B, 20 mm. C-D. Representative images showing that in the NeuroD1 group, after astrocyte-to-neuron conversion (30 days post AAV NeuroD1 infection), NeuroD1 immunostaining (green) detected clear NeuroD1 signal in the NeuroD1-mCherry-converted neurons (red). Scale bar for panel C, 100 mm. Panel D shows the enlarged box area in panel C. Scale bar for panel D, 20 mm. E. Quantitative analysis showing that the exogenous NeuroD1 expression level in NeuroD1-mCherry-converted neurons was significantly higher than the endogenous NeuroD1 expression level. **$P < 0.01$, Student's t-test ($n = 3$ animals for each group).

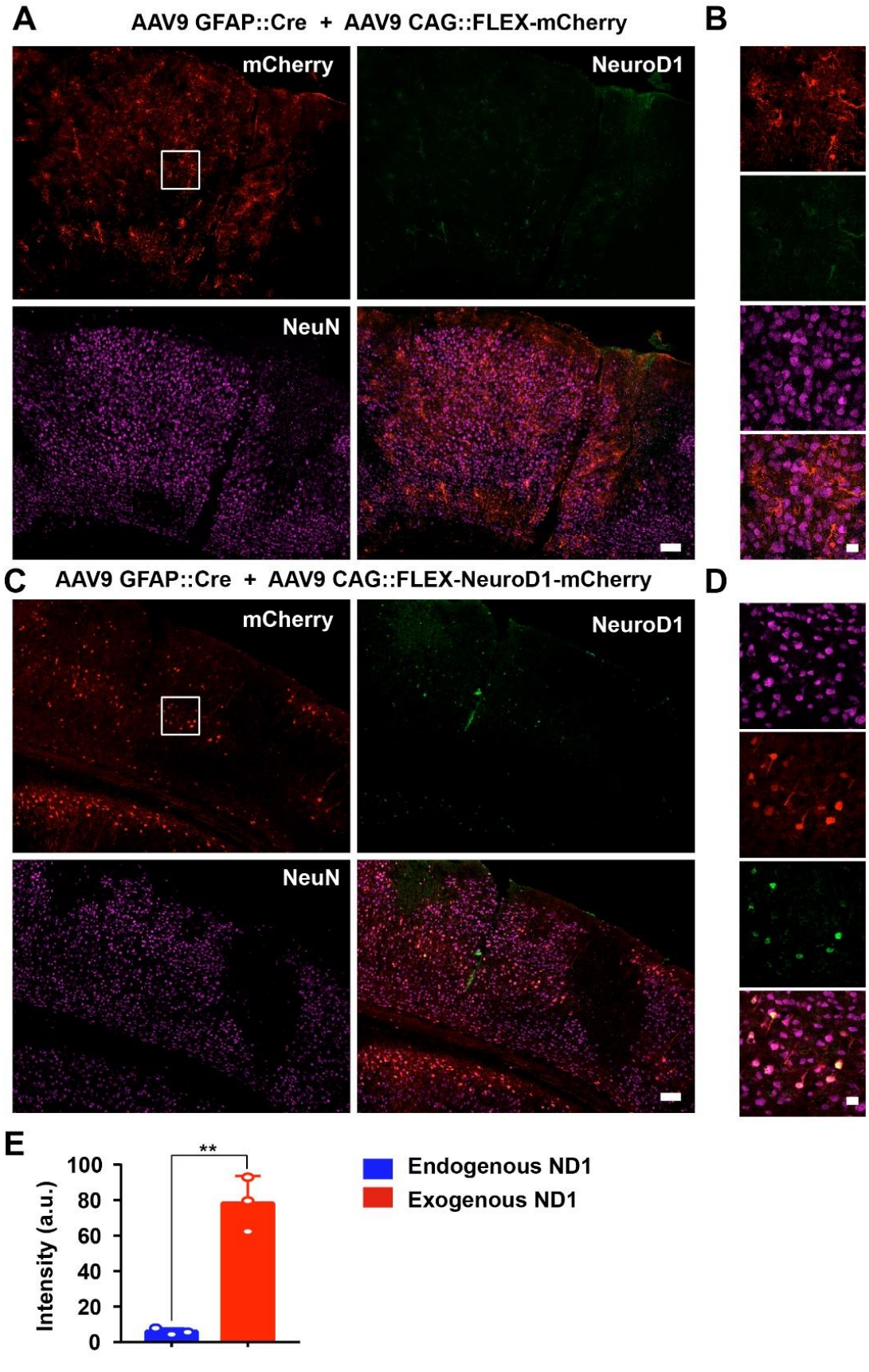
A
AAV9 GFAP::Cre + AAV9 CAG::FLEX-mCherry
mCherry
NeuroD1
NeuN
B
C
AAV9 GFAP::Cre + AAV9 CAG::FLEX-NeuroD1-mCherry
mCherry
NeuroD1
NeuN
D
E
Intensity (a.u.)
100
80
60
40
20
0
**
Endogenous ND1
Exogenous ND1

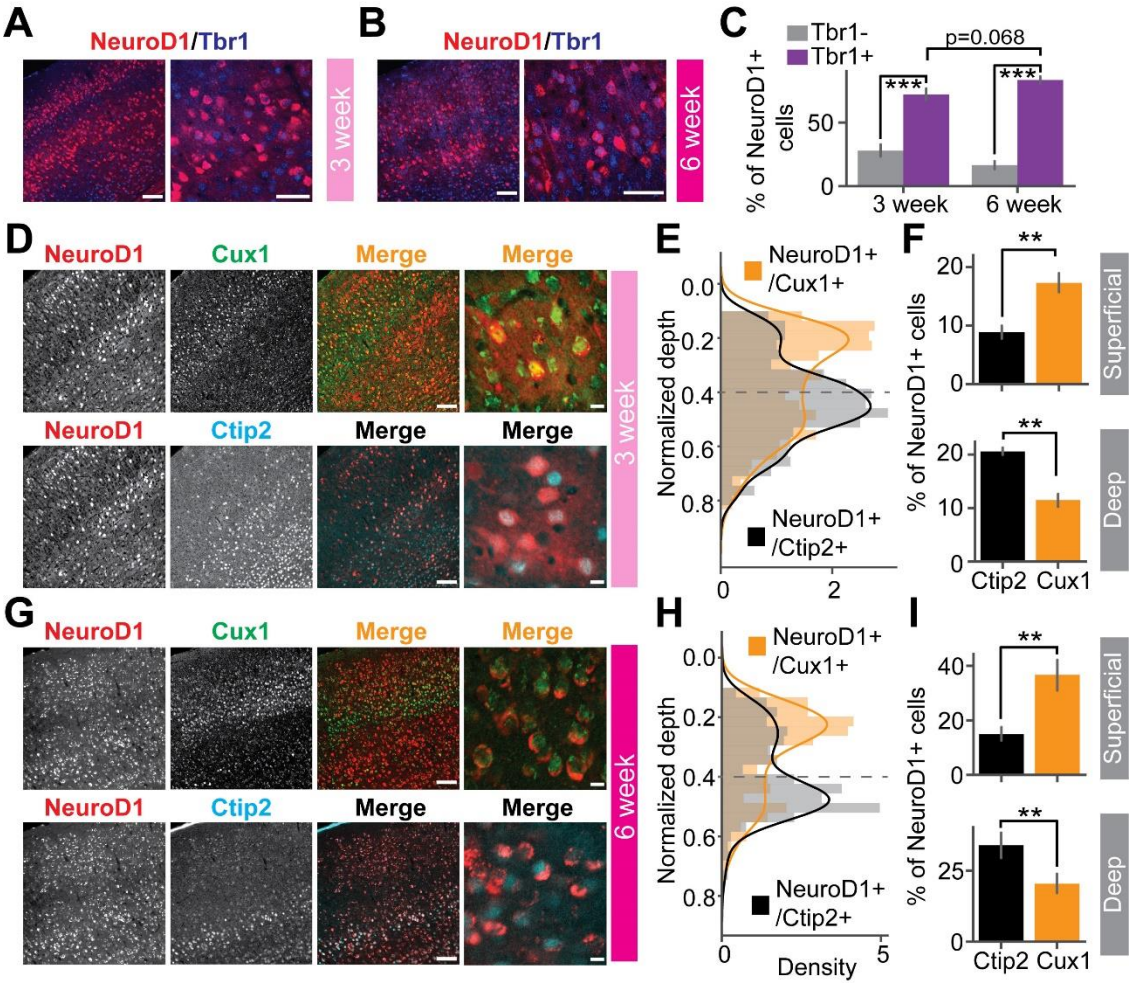

Figure 3.4 Reprogrammed cells acquire superficial and deep cortical layer identities. A. NeuroD1 positive cells stained with cortical neuron marker Tbr1 at 3 weeks after the viral injection. $Scale_{left}$: 100μm, $Scale_{right}$: 50μm. B. Same as A but at 6 weeks after the viral injection. C. Quantification of Tbr1 positive cells out of NeuroD1 positive cells. Tbr1- vs. Tbr1+: N_{3week}= 2 mice, 12 slices, $p=1.23\times10^{-4}$; N_{6week}= 4 mice, 23 slices, $p=1.51\times10^{-8}$. 3 week vs. 6 week: p=0.068. Mann-Whitney U test with Bonferroni correction. D. A representative slice showed that NeuroD1 positive cells co-stained with superficial layer marker Cux1 (top row), deep-layer marker Ctip2 (bottom row) at 3 weeks after the viral injection. The NeuroD1 image at the top and bottom row is the same. $Scale_{left}$: 100μm, $Scale_{right}$: 10μm. E. Probability density of counts of NeuroD1+/Cux1+ cells and NeuroD1+/Ctip2+ cells across normalized cortical depths at 3 weeks after the viral injection. 0 indicates the brain surface. The dashed line indicates superficial and deep layer separation. F. Percentages of Cux1+/NeuroD1+ and Ctip2+/NeuroD1+ cells in the superficial layers (top) and the deep layers (bottom) at 3 weeks after the viral injection. $N_{superficial}$= 2 mice, 4 slices, $p=3.06\times10^{-3}$. N_{deep}= 2 mice, 4 slices, $p=2.54\times10^{-3}$. Mann-Whitney U test with Bonferroni correction. G. Same as D but at 6 weeks after the viral injection. H. Same as E but at 6 weeks after the viral injection. I. Same as F but at 6 weeks after the viral injection. $N_{superficial}$= 3 mice, 7 slices, $p=3.06\times10^{-3}$. N_{deep}= 3 mice, 7 slices, $p=2.33\times10^{-3}$. Mann-Whitney U test with Bonferroni correction.**-p<0.05, ***-p<0.001. Data are represented as mean ± SEM.

3.4.2 In vivo direct reprogramming recovered visually evoked potentials (VEPs) and single-unit responses

To assess functional recovery of V1 after reprogramming, we recorded visually evoked potentials (VEPs) and single-unit spikes in awake head-fixed mice using extracellular recording technique. Mice were separated into two groups (Figure 3.5A). In one group, ET-1 ischemia was induced in both hemispheres, followed by reprogramming (FLEX-NeuroD1-mCherry) in one hemisphere and the other hemisphere injected with a control virus (FLEX-mCherry) ("ET-1+NeuroD1 vs. ET-1+Control"). In the other group, ischemia was induced in only one hemisphere followed by reprogramming (FLEX-NeuroD1-mCherry), and the other hemisphere was sham-injected (ACSF) and treated with the control virus ("ET-1+NeuroD1 vs. ACSF+Control"). Mice were habituated to the head-fixation setup prior to experiments. Three weeks after viral injections, visual response to sinusoidal drifting gratings was recorded with a silicon probe (recording site validated with histology, Figure 3.5B and C). VEPs were compared between the two hemispheres within the same mouse to control for individual variability across animals. To validate visual function impairment by ET-1 induced ischemia, we added a group of mice, which were given only ET-1/ACSF injection. VEP amplitudes were significantly smaller in the ET-1 injected hemispheres compared to the ACSF injected hemispheres (Figure 3.5D). Next, we tested "ET-1+NeuroD1 vs. ET-1+Control" mice. VEP amplitudes were significantly larger in the ET-1+NeuroD1 hemispheres than the ET-1+Control hemispheres (Figure 3.5E). In contrast, for the "ET-1+NeuroD1 vs. ACSF+Control" group, VEP amplitudes were not significantly different between the two hemispheres (Figure 3.5F). In addition to the synchronized population activity, we also examined the single unit visual responses. Considering the heterogeneity of cortical neurons, we split the units into putative regular-spiking (RS) and fast-spiking (FS) units, based on trough-to-peak latencies and waveform latencies of their averaged template waveforms (Figure 3.5G). Based on both intracellular and extracellular studies, excitatory pyramidal neurons show regular-spiking waveforms, while inhibitory interneurons show fast-spiking waveforms (Connors and Gutnick, 1990;Henze et al., 2000;Trainito et al., 2019). To account for different baseline activity across units, we calculated the z-scores of firing rate over time for each unit. Z-scores of the visually evoked responses of all recorded units are shown in heatmaps (Figure 3.5H). In the "ET-1+NeuroD1 vs. ET-1+Control" group, RS units in the ET-1+NeuroD1 hemispheres showed

Figure 3.5 In vivo direct reprogramming recovers visually evoked potentials (VEPs) and single unit visual responses. A. The injection scheme for in vivo experiments. B. The in vivo awake extracellular recording setup. C. Histology showing the probe track (green) within the reprogramming site. NeuroD1: orange, DAPI: blue. The brain atlas is adapted from Allen adult mouse brain coronal atlas, image 90. Scale: 500µm (top and botom). D. Averaged VEPs of ET-1 and ACSF hemispheres. Quantification of VEP amplitudes on the right in each panel. N1=N2=27 recording sites, 9 mice, p=3.07x10-4, Mann-Whitney U test. E. Same as D but for ET-1+Control and ET-1+NeuroD1 hemispheres. N1=N2=33 recording sites, 11 mice, p= 1.30x10-5, Mann-Whitney U test. F. Same as D but for ACSF+Control and ET-1+NeuroD1 hemispheres. N1=N2=30 recording sites, 10 mice, p= 0.559, Mann-Whitney U test. G. Units classified into regular-spiking (RS), fast-spiking (FS), and unclassified (UN) units. Scatter plot showing trough-to-peak latency and waveform width of the units. The averaged template waveforms shown in the inset. H. Firing rate z-scores of all units in heatmaps for "ET-1+Control vs. ET-1+NeuroD1" and "ACSF+Control vs. ET-1+NeuroD1" groups. The numbers of RS, FS, and UN units are shown on the left for each heatmap. I. Left: Firing rate z-scores of RS units in the "ET-1+Control vs. ET-1+NeuroD1" group. The shaded area: visual stimulation. Bar graph showing peak z-scores within the visual stimulation window. NET-1+Control=161 units, 11 mice, NET-1+NeuroD1=198 units, 11 mice, p=1.56x10-3, Mann-Whitney U Test. Right: Same as the left but for FS units. NET-1+Control=48 units, 11 mice, NET-1+NeuroD1=63 units, 11 mice, p=0.084, Mann-Whitney U Test. J.Left: Firing rate z-scores of RS units in the "ACSF+Control vs. ET-1+NeuroD1" group. The shaded area: visual stimulation. Bar graph showing peak z-scores within the visual stimulation window. NACSF+Control =237 units, 10 mice, NET-1+NeuroD1=334 units, 10 mice, p=0.238, Mann-Whitney U Test. Right: Same as the left but for FS units. NACSF+Control =58 units, 10 mice, NET-1+NeuroD1=74 units, 10 mice, p=0.0058, Mann-Whitney U Test. *-$p<0.05$, **-$p<0.01$, ***-$p<0.001$, n.s.-not significant. Data are represented as mean ± SEM.

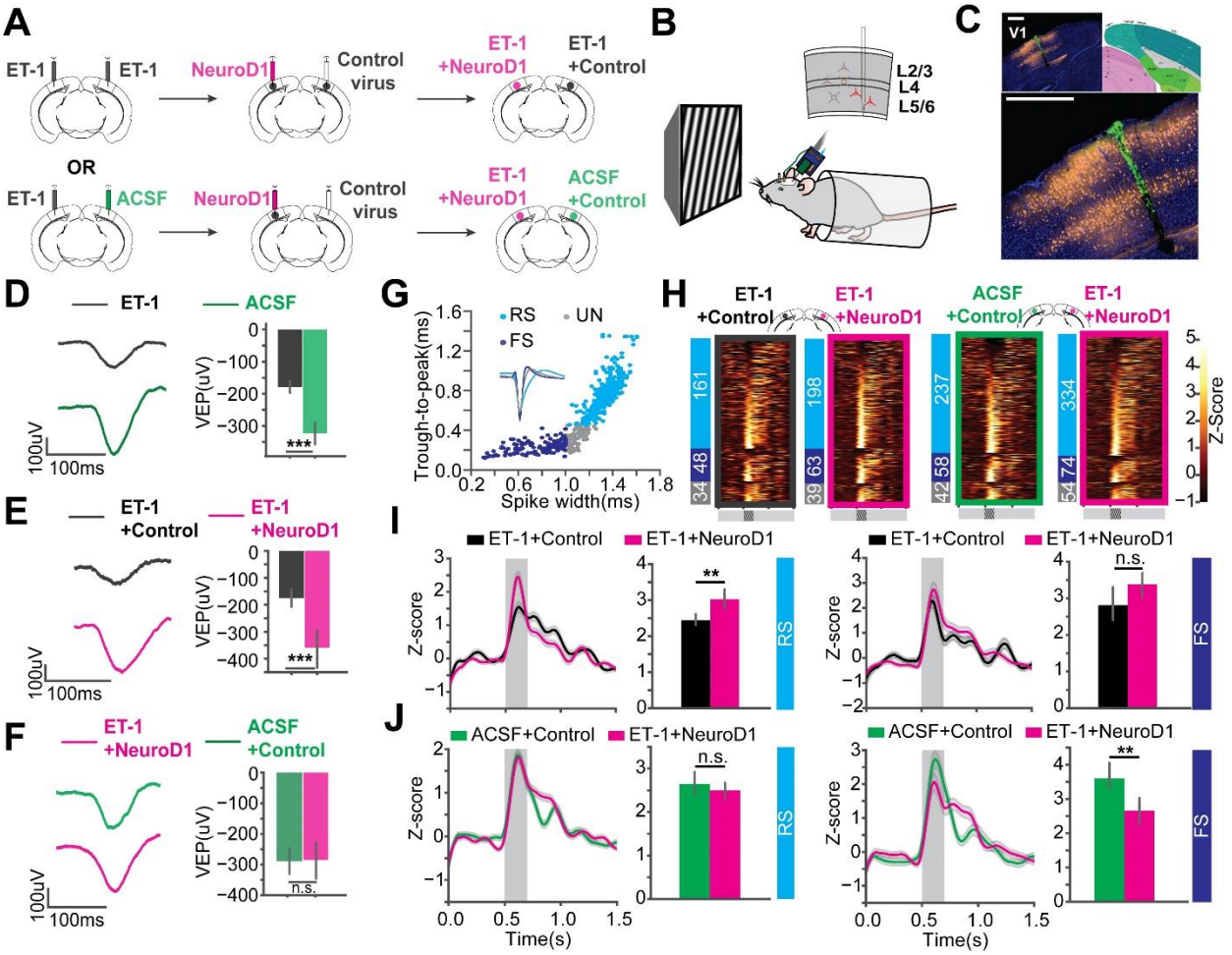
A
ET-1
ET-1
NeuroD1
Control virus
ET-1 +NeuroD1
ET-1 +Control
OR
ET-1
ACSF
NeuroD1
Control virus
ET-1 +NeuroD1
ACSF +Control
B
L2/3
L4
L5/6
C
V1
D
ET-1
ACSF
100uV
100ms
VEP(uV)
***
E
ET-1 +Control
ET-1 +NeuroD1
100uV
100ms
VEP(uV)
***
F
ET-1 +NeuroD1
ACSF +Control
100uV
100ms
VEP(uV)
n.s.
G
RS
UN
FS
Trough-to-peak(ms)
Spike width(ms)
H
ET-1 +Control
ET-1 +NeuroD1
ACSF +Control
ET-1 +NeuroD1
161
48
34
198
63
39
237
58
42
334
74
54
Z-Score
I
ET-1+Control
ET-1+NeuroD1
Z-score
**
RS
n.s.
FS
J
ACSF+Control
ET-1+NeuroD1
Z-score
n.s.
RS
**
FS
Time(s)
Time(s)

significantly higher peak firing rate z-scores compared to the ET-1+Control hemispheres (Figure 3.5I left). In the same group, FS units in the ET-1+NeuroD1 hemispheres showed similar peak firing rate z-scores compared to the ET-1+Control hemispheres (Figure 3.5I right). In the "ET-1+NeuroD1 vs. ACSF+Control" group, RS units in the ET-1+NeuroD1 hemispheres showed comparable peak firing rate z-scores to the ACSF+Control hemispheres (Figure 3.5J left). Interestingly, FS units in the ET-1+NeuroD1 hemispheres showed lower peak firing rate z-scores than the ACSF+Control hemispheres (Figure 3.5J right). These results demonstrate that ET-1 induced ischemia significantly impairs visual response in V1, and in vivo direct reprogramming restores the visual responses, to a comparable level as in the sham condition. The single-unit activity suggests that there may be a differential recovery of visual responses in RS and FS cells. At 3 weeks post-infection, RS cells have regained normal levels of visual responsiveness, while FS cells have not.

3.4.3 Reprogrammed neurons were integrated into the local circuit and hyper-connected at an early stage

Paired recordings are used to measure the strength of the connection between neighboring neurons. However, the probability of finding a connected pair decreases drastically with increasing distance, making it unsuitable for any specific interlaminar or long-range synaptic connections. Channelrhodopsin-assisted circuit mapping (CRACM) can measure the strength of the specific genetically labeled long-range and interlaminar connections (Petreanu et al., 2007;Yamawaki and Shepherd, 2015). To directly measure the circuit connectivity of newly reprogrammed neurons, we used CRACM in ex vivo acute slices. We used heterozygous Thy1-ChR2-YFP mice that have a sparse distribution of ChR2-eYFP positive cells among the layer 5 pyramidal cells in V1 (Arenkiel et al., 2007). Focal ischemia induction and reprogramming viral injection procedures were the same as for mice used for in vivo recordings (Figure 3.6A). Age-matched mice were randomly assigned to three groups: Healthy control (ACSF+Control), Untreated control (ET-1+Control), and reprogrammed (ET-1+NeuroD1). For each mouse, both hemispheres received the same treatment. We further divided neurons in the reprogrammed group into mCherry-positive reprogrammed cells and mCherry-negative surviving neighbors. We then performed whole-cell patch-clamp recordings using differential interference contrast (DIC) microscopy and fluorescent image-guided targeting (Figure 3.6B). Basic electrophysiological properties were characterized by

recording the membrane potential changes following a series of step currents for each cell (Figure 3.6C). Then, CRACM maps were collected in the presence of TTX and 4-AP to isolate mono-synaptic connections (Figure 3.6D). For some mCherry-positive reprogrammed cells, a fluorescent dye was included in the patching pipette, and extra time was allowed after recording for the dye to diffuse into the cell processes (Figure 3.6E). Morphological reconstructions showed that all examined cells had extensive neurites that resembled cortical neurons (Figure 3.6F). All mCherry-positive cells in the reprogrammed group showed robust light-induced excitatory post-synaptic currents (EPSCs) (Figure 3.6G). Surviving neighbors also received considerable excitatory inputs (Figure 3.6H) qualitatively similar to that of healthy controls (Figure 3.6J). On the contrary, there were minimal EPSCs in cells in the untreated ischemia group (Figure 4I). The maximal EPSC profile along tangential (Figure 3.6K) and vertical (Figure 3.6L) directions averaged across cells for each group revealed no shift in the overall shape of the EPSCs spatial distribution. We then compared the distributions of averaged EPSC amplitudes among the four groups of cells. The reprogrammed cells had significantly larger responses than all the other groups, as shown in the cumulative density curve. To compare the relative connection strength between groups, we transformed the absolute values of EPSC amplitudes to normal distributions using Box-Cox transformation (details see "Methods"). The transformed EPSCs were normally distributed in all four groups. The reprogrammed group had the largest mean of transformed EPSC values, while the untreated ischemia group had the smallest (Figure 3.6M inset). The CRACM experiment at 3 weeks post-infection directly demonstrated that functional synaptic inputs from the layer 5 pyramidal neurons of the pre-existing local circuits were formed onto the newly reprogrammed neurons. The relative strength of these projections was stronger than projections onto neurons in the same cortical area without ischemic insult. Surviving endogenous neurons following the ischemic injury in the reprogrammed group had stronger synaptic connections with the circuit than surviving neurons in the untreated ischemia condition.

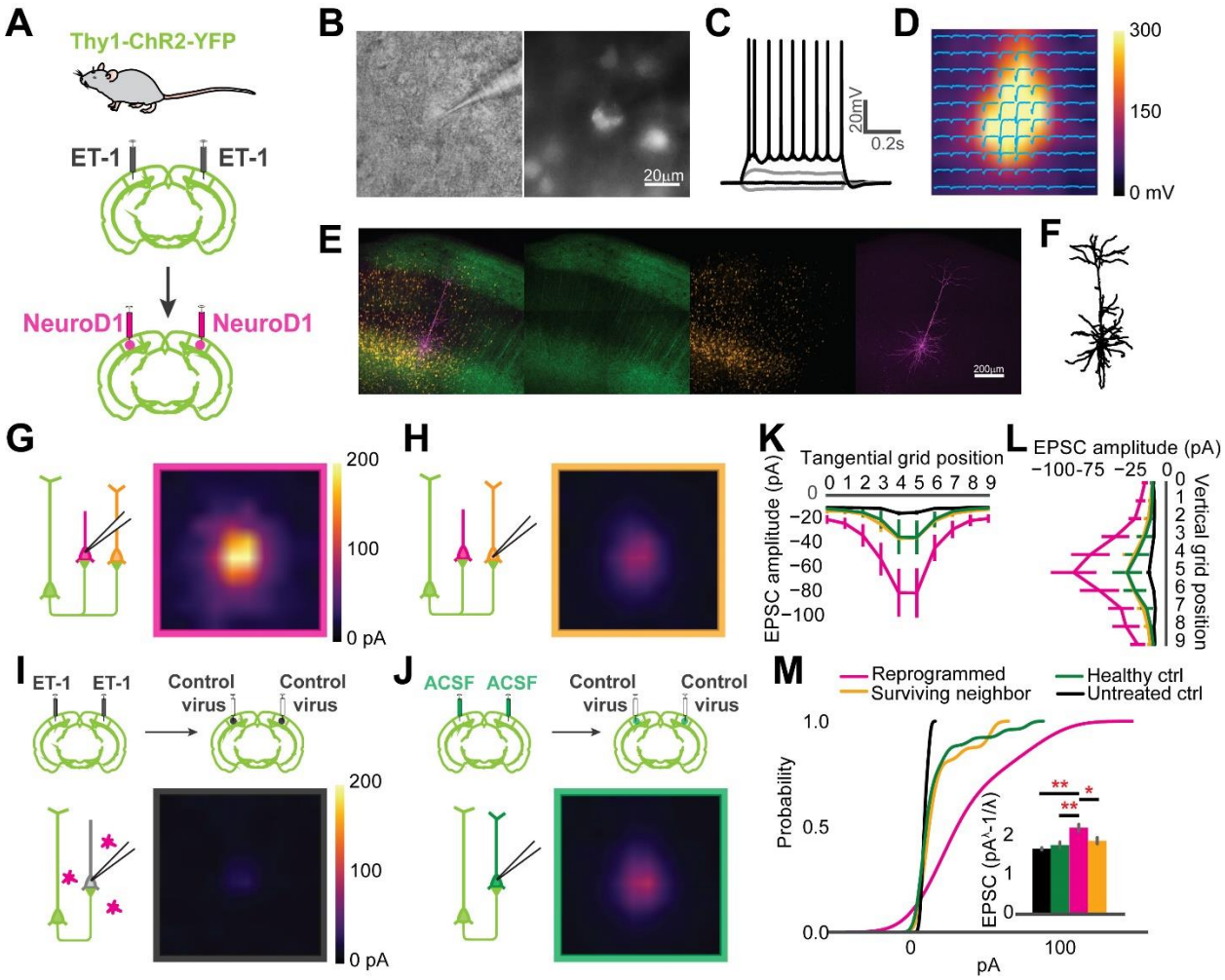

Figure 3.6 Reprogrammed neurons are integrated into the local circuit and hyper-connected at an early stage. A. Thy1-ChR2-YFP mice used for Channelrhodopsin-Assisted Circuit Mapping (CRACM) experiments. B. An example whole-cell patch in Differential Interface Contrast (DIC) image (left) and epifluorescence image (right), showing a mCherry positive cell. C. The cell in B showing evoked action potentials after step-current injection. D. EPSC amplitudes of the cell in B shown in a CRACM heatmap overlaid with EPSC traces at each stimulation point. E. Confocal images of showing a layer 5 neurons expressing ChR2-YFP (green) and reprogrammed cells expressing mCherry (orange). The patched cell filled with dye (magenta). Scale: 200μm. F. Morphology of the cell processes from images in E. G. Averaged CRACM heat map of mCherry positive reprogrammed cells (N=21 cells from 6 mice). H. Same as G but for mCherry negative survived neighbors (N=16 cells from 6 mice). I. Averaged CRACM heat maps of untreated ischemia control (I, N=19 cells from 4 mice). J. Same as I but for healthy control (N=26 cells from 5 mice). K. Averaged maximal EPSC ± SEM by grid position in the tangential direction (parallel to the brain surface). L. Averaged maximal EPSC ± SEM by grid position in the vertical direction (perpendicular to the brain surface). M. Cumulative density of EPSCs from each group. The inset bar graph showing Box-Cox-transformed EPSCs amplitude comparison among groups. Reprogrammed vs. Untreated: p=0.001; Reprogrammed vs. Healthy: p=0.001; Reprogrammed vs. Surviving: p=0.0178, One-way ANOVA followed by Tukey post-hoc tests. **-p<0.01, **-p<0.05, from Tukey's HSD. Data are represented as mean ± SEM.

3.4.4 Correction of the circuit hyperconnectivity and fast-spiking unit responses six weeks after in vivo direct reprogramming

Circuit connectivity and visual responses improved after the NeuroD1-based gene therapy treatment. However, differences were observed between the reprogrammed and the healthy control groups in both visual responses and circuit connectivity three weeks after viral infection. To examine the effect of additional maturation of the reprogrammed neurons on their integration into the local circuits, we further measured circuit connectivity and visual responses six weeks after viral injections in mice receiving visual experience in their housing cages. We conducted CRACM on visual cortex slices ex vivo to compare the connectivity profile of the newly reprogrammed cells, their surviving neighbors, surviving cells in the untreated ischemia controls, and cells in the healthy controls. The acute brain slices were prepared using the NMDG recovery method (Ting et al., 2018) due to the age of the mice (2.5 months at the time of CRACM, see methods for details). Reprogrammed cells were well connected to local circuits (Figure 3.7A, top left) as well as their surviving neighbors (Figure 3.7A, top right). The average connectivity maps of reprogrammed cells and surviving neighbors were comparable to that of the healthy control group (Figure 3.7A, bottom right) and were more prominent than the untreated ischemia control (Figure 3.7A, bottom left). The maximal EPSC profile along tangential (Figure 3.7B) and vertical (Figure 3.7C) directions averaged across cells for each group revealed no shift in the overall shape of the EPSCs spatial distribution. When comparing the EPSC amplitude, interestingly, the hyper-connectivity to the local circuits in the reprogrammed group was much less prominent compared to the three weeks post-infection results. When counting the number of hot spots that had larger than 30pA EPSC amplitudes, the reprogrammed cells received inputs at less hot spots at 6 weeks post-infection, compared to 3 weeks post-infection (Figure 3.8). The reprogrammed group received significantly stronger projections than the untreated ischemia control group and received equally strong projections than the healthy control group (Figure 3.7D inset). In addition, their surviving neighbors received projections that were not significantly different from a healthy control.

Ischemic injury prevalence increases with age (Johnston et al., 2003; Ovbiagele and Nguyen-Huynh, 2011). Therefore, we conducted similar experiments in older adults to test whether the positive effect of reprogramming in treating ischemic injury also applies to old mice over three months old. In older adults, the averaged CRACM maps showed the same trend as in young adults that newly converted neurons received robust projections, as well as their surviving neighbors, at

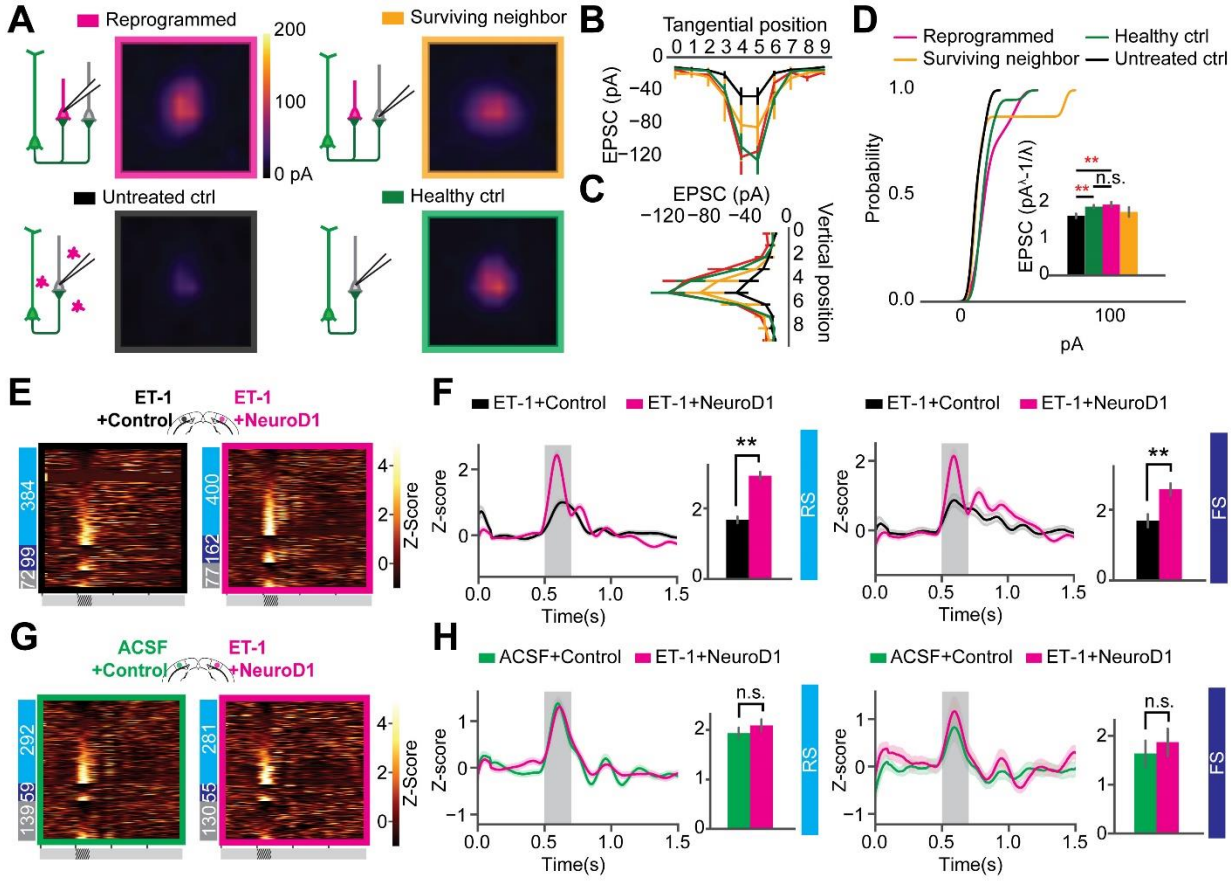

Figure 3.7 Correction of circuit hyperconnectivity and fast-spiking unit responses at 6 weeks after in vivo direct reprogramming. A. Averaged CRACM heat map of reprogrammed cells (N=12 cells from 9 mice), surrounding neighbors (N=8 cells from 9 mice), untreated control (N=16 cells from 6 mice), and healthy control (N=22 cells from 4 mice), measured at 6 weeks after viral infection. B. Averaged maximal EPSC ± SEM by grid position in the tangential direction (parallel to the brain surface). C. Averaged maximal EPSC ± SEM by grid position in the vertical direction (perpendicular to the brain surface). D. The cumulative density curve showing the distribution of pooled EPSCs amplitude in C. The inset bar graph showing Box-Cox-transformed EPSCs amplitude comparison among groups. Reprogrammed vs. Untreated: p=0.00995; Reprogrammed vs. Healthy: p=0.900; Surviving vs. Healthy: p=0.312. One-way ANOVA followed by Tukey post-hoc tests. E. Firing rate z-scores of all units in heatmaps for "ET-1+Control vs. ET-1+NeuroD1" group. The numbers of RS, FS, and UN units are shown on the left. F. Firing rate z-scores of RS (left) and FS (right) units in the "ET-1+Control vs. ET-1+NeuroD1" group. RS units: NET-1+Control=384 units, NET-1+NeuroD1=400 units, p=4.09x10-3. FS units: NET-1+Control=99 units, NET-1+NeuroD1=162 units, p=0.0065. 14 recordings. Mann-Whitney U test with Bonferroni correction. G. Same as E but for "ACSF+Control vs. ET-1+NeuroD1" group. H. Same as F but for the "ACSF+Control vs. ET-1+NeuroD1" group. The shaded area represents visual stimulation. Peak z-scores within the visual stimulation window were quantified. RS units: NACSF+Control=292 units, NET-1+NeuroD1=281 units, p=0.499. FS units: NACSF+Control=59 units, NET-1+NeuroD1=55 units, p=0.540. 9 recordings. Mann-Whitney U test with Bonferroni correction. **-p<0.01. Data are represented as mean ± SEM.

a comparable level as in healthy control, and the projections were much more prominent than in untreated ischemia control (Figure 3.9A and B). To account for the overall cortical connectivity change and the concomitant Channelrhodopsin-2 expression level changes over time, we normalized logEPSC values of each group against the healthy control of the same time point. The reprogrammed cells had very prominent hyper-connectivity at three weeks after viral infection (Figure 3.9C), the magnitude of which largely decreased six weeks post-infection in both young and old adults. The connection strength of the surviving neighbor cells in the reprogrammed mice matched the healthy control at six weeks post-infection. In addition, we analyzed input resistance based on membrane potential changes upon current injections for each patched cell. The newly converted cells at 3 weeks after a viral infection had significantly lower input resistance compared to the other groups (Figure 3.9D). This input resistance difference diminished six weeks post-infection in both young and old adults, suggesting intrinsic properties of the reprogrammed cells change over time.

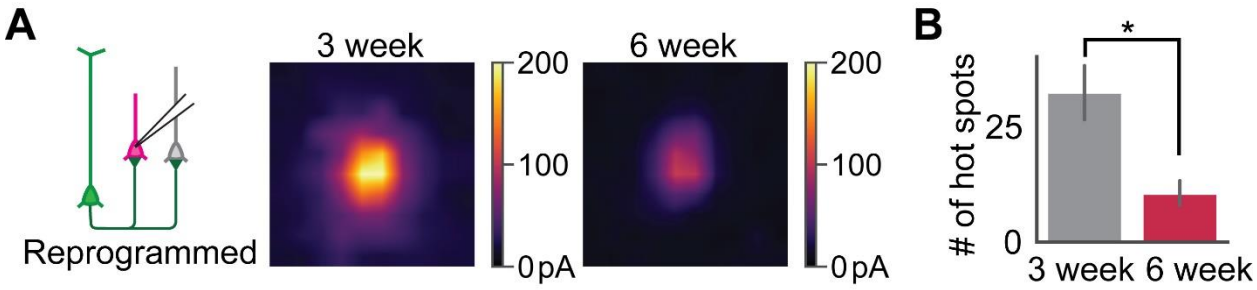

Figure 3.8 The reprogrammed cells received less synaptic inputs at 6 weeks compared to 3 weeks post-injection. A. Averaged CRACM maps of reprogrammed cells at 3 weeks and 6 weeks post-injection. B. Quantification of the numbers of CRACM heatmap hot spots that had larger than 30pA EPSC amplitude. N3week=21 cells from 6 mice, N3week=12 cells from 9 mice. Mann-Whitney U test. *-$p<0.05$. Data are represented as mean ± SEM.

Visual responses in the NeuroD1 treated mice also showed continued improvement. In the "ET-1+Control vs. ET-1+NeuroD1" group, not only RS unit firing, but also FS unit firing was significantly higher in the ET-1+NeuroD1 hemispheres than the ET-1+Control hemispheres (Figure 3.7F). In the "ET-1+NeuroD1 vs. ACSF+Control" group, RS unit firing in the ET-1+NeuroD1 hemispheres was comparable to the ACSF+Control hemispheres (Figure 3.7H left). Interestingly, unlike three weeks post-infection, FS unit firing was not significantly different from the ACSF+Control hemispheres (Figure 3.7H right). This suggests that FS cells have delayed development compared to RS units.

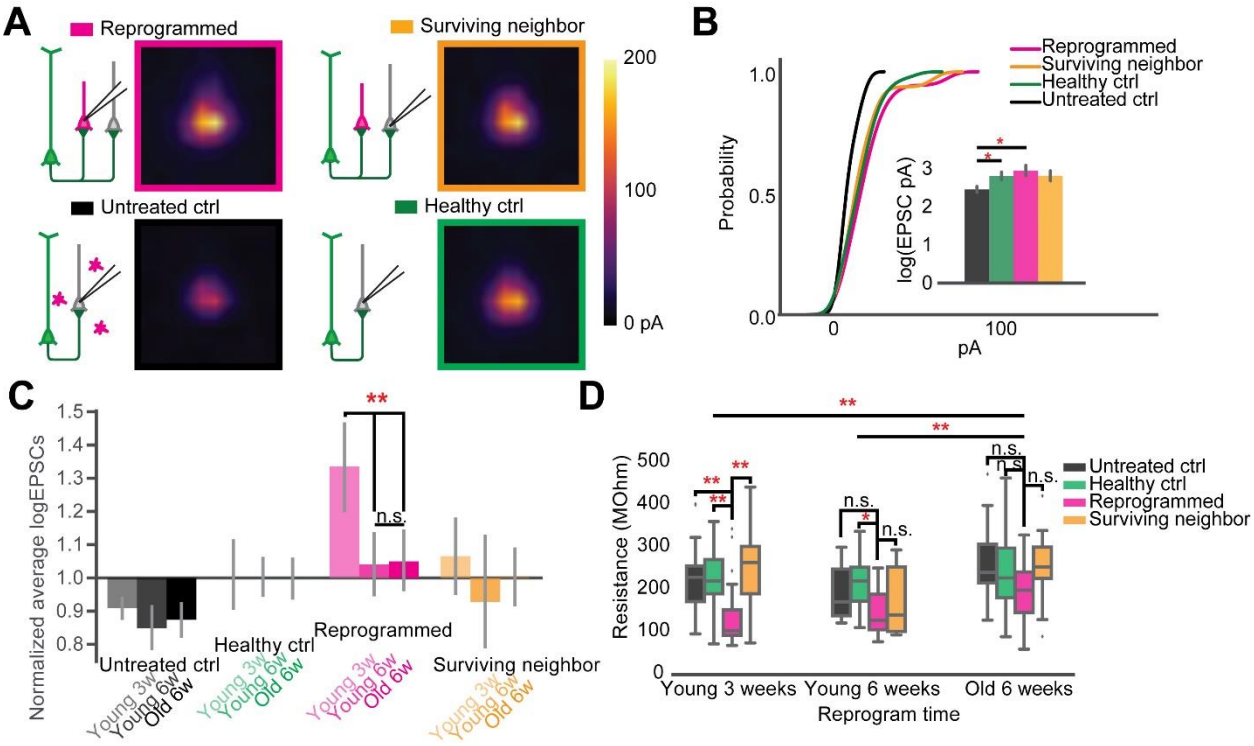

Figure 3.9 Circuit repair restoration with *in vivo* direct reprogramming after ischemic injury were consistent in older adult mice. A. Averaged CRACM heat map of reprogrammed cells (N=18 cells from 9 mice), surrounding neighbors (N=16 cells from the same cohort of 9 mice), untreated control (N=28 cells from 9 mice), and healthy control (N=34 cells from 8 mice), measured at 6 weeks after viral infection in animals older than 3 months. B. The cumulative density curve showing the distribution of pooled EPSCs amplitude in A. The inset bar graph showing comparison of the log-transformed EPSCs amplitude among all groups. Reprogrammed vs. Untreated: p=0.0135; Untreated vs. Healthy: p=0.048. One-way ANOVA followed by Tukey post-hoc tests. C. logEPSC at each time point normalized against the sham control. Two-way ANOVA, Groups: $F(3)=15.941$, $p=1.984\times10^{-9}$; Timepoints: $F(2)=5.467$, $p=4.81\times10^{-3}$; interaction: $F(6)=2.532$, $p=0.064$. Tukey's HSD test, untreated group: Young 3w vs. Old 6w p=0.603; Young 3w vs. Young 6w p=0.680; Young 6w vs. Old 6w p=0.900. Reprogrammed: Young 3w vs. Young 6w p=0.00433; Young 3w vs. Old 6w p=0.00157, Young 6w vs. Old 6w p=0.900. Surviving: Young 3w vs. Young 6w p=0.375; Young 3w vs. Old 6w p=0.711, Young 6w vs. Old 6w p=0.732. Tukey's HSD test. D. The comparison of input resistance at each time point. Two-way ANOVA, Groups: $F(3)=9.41$, $p = 7\times10^{-6}$; Timepoints: $F(2)=7.884$, p=0.000493; interaction: $F(6)=0.726$, p=0.629. Tukey's HSD test, among Groups at Young 3 weeks: Reprogram vs. Surviving p=0.00115; Reprogram vs. Untreated p=0.00562; Reprogram vs. Healthy p=0.00506; Young 6 weeks: Reprogram vs. Healthy: p=0.0187; p>0.05 for all other pairs of comparison at Young 6 weeks and Old 6 weeks. Old 6 weeks vs. Young 6 weeks: p=0.00771; Old 6 weeks vs. Young 3 weeks: p=0.00113; Young 3 weeks vs. Young 6 weeks p=0.685. Tukey post-hoc tests. *-p<0.05, **-p<0.01, ***-p<0.001, n.s.-not significant. Data are represented as mean ± SEM.

3.4.5 Orientation selectivity of the local neuronal population was improved over time

Following postnatal development and visual experience, most V1 neurons acquire preference to a specific orientation (Li et al., 2008; Nauhaus et al., 2008; Ko et al., 2011). To further assess functional recovery following reprogramming, we examined neuronal unit activity in response to sinusoidal gratings of 6 orientations (Figure 3.10A). Representative units and population firing rate z-scores to different orientations revealed selective responses of most units in each group (Figure 3.10A and B). To quantify population selectivity to orientations, we averaged firing rate across units to 6 orientations and fitted Gaussian functions for each group to estimate "population tuning curves." Three weeks (3wk) post-infection, in the "ET-1+NeuroD1 vs. ET-1+Control" group, tuning curve width (variance (σ) of the fitted function) was 20.957 degrees for the ET-1+NeuroD1 hemisphere, only slightly sharper than 21.322 degrees for the ET-1+Control hemisphere (Figure 3.10C, top). At the same time, in the "ET-1+NeuroD1 vs. ACSF+Control" group, the ET-1+NeuroD1 hemisphere tuning curve width was 20.387 degrees, broader than 17.995 degrees of the ACSF+Control hemisphere (Figure 3.10E top). However, six weeks (6wk) post-infection, in the "ET-1+NeuroD1 vs. ET-1+Control" group, the tuning curve width was 17.504 degrees for the ET-1+NeuroD1 hemisphere, sharper than 22.880 degrees for the ET-1+Control hemisphere (Figure 3.10C, bottom). In the "ET-1+NeuroD1 vs. ACSF+Control" group, the ET-1+NeuroD1 hemisphere tuning curve width was 18.228 degrees, comparable to 17.885 degrees for the ACSF+Control group (Figure 3.10E, bottom). To quantitatively compare orientation selectivity distributions between groups, we calculated the orientation selectivity index (one minus the circular variance of firing rates to 6 orientations, 1-CV) for each unit (Figure 3.10D, 6F, see method for details). In the "ET-1+NeuroD1 vs. ET-1+Control" group, the cumulative distribution of 1-CV of the ET-1+NeuroD1 hemisphere showed no difference compared to the ET-1+Control hemisphere at three weeks, and marginal difference at six weeks post-infection. While in the "ET-1+NeuroD1 vs. ACSF+Control" group, the cumulative distribution of 1-CV of the ET-1+NeuroD1 hemisphere was left-shifted compared to the ACSF+Control hemisphere at three weeks but was not different at six weeks post-infection. These results revealed that the orientation tuning of the cortical population was not completely recovered three weeks post-reprogramming but was comparable to the sham condition six weeks post-reprogramming.

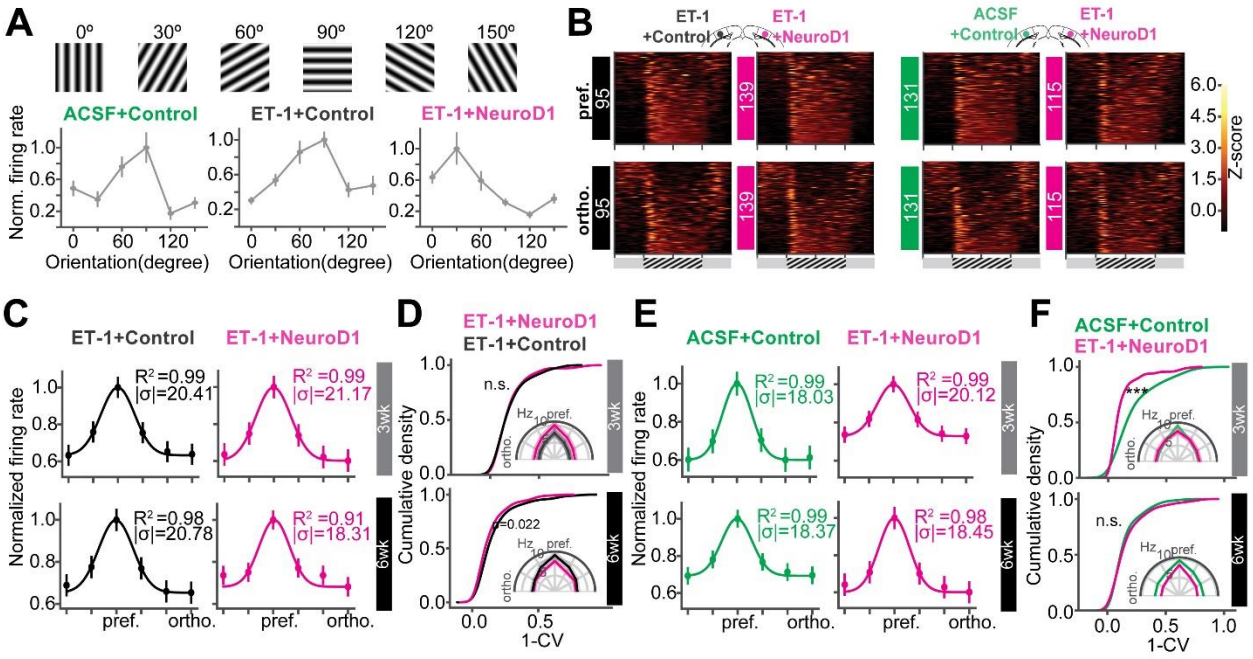

Figure 3.10 Orientation selectivity of the local neuronal population is improved over time. A. Gratings of 6 orientations used to measure orientation selectivity. Bottom: normalized firing rate of representative units for each group. B. Heatmaps of firing rate z-scores of all units in response to the preferred (pref., top) and the orthogonal (ortho., bottom) orientations for each group. C. The curves showing unit averaged firing rates to 6 orientations normalized and fitted with Gaussian functions of the "ET-1+NeuroD1 vs. ET-1+Control" group at 3 weeks (3wk) and 6 weeks (6wk) post-infection. The insets showing the coefficient of determination (R^2) and sigma of fitted functions. D. Cumulative distributions of 1-CV of units in C. Inset, unit averaged firing rates to 6 orientations. 3 weeks (3wk): $N_{ET\text{-}1+Control}$=95 units, $N_{ET\text{-}1+NeuroD1}$=139 units, from 6 mice, p= 0.954; 6 weeks (6wk): $N_{ET\text{-}1+Control}$=93 units, $N_{ET\text{-}1+NeuroD1}$=142 units, from 4 mice, p= 0.022. 2-sample Kolmogorov-Smirnov test. E. Same as C but for "ET-1+NeuroD1 vs. ACSF+Control" group. F. Same as D but for "ET-1+NeuroD1 vs. ACSF+Control" group. 3wk: $N_{ACSF+Control}$=131 units, $N_{ET\text{-}1+NeuroD1}$=115 units, from 4 mice, p= 1.659×10^{-7}; 6wk: $N_{ACSF+Control}$=183 units, $N_{ET\text{-}1+NeuroD1}$=172 units, from 8 mice, p= 0.652, 2 sample Kolmogorov-Smirnov test. ***-p<0.001, n.s.-not significant. Data are represented as mean ± SEM.

However, the orientation selectivity of the NeuroD1 group could be the result of either improvement in the reprogrammed neurons or pre-existing neurons, or both. To answer this question, we used 2-photon calcium imaging to look at the visual responses of the reprogrammed cells to drifting gratings of 12 directions, and compared to the healthy controls. The specific expression of GCaMP6s in reprogrammed neurons was achieved by injecting AAV-CAG::FLEX-GCaMP6s together with AAV-GFAP::Cre and AAV-FLEX-NeuroD1-mCherry (Figure 3.11A). Most reprogrammed cells expressed GCaMP6s, and could be identified as well-separated regions

of interest (ROIs, Figure 3.11B). The reprogrammed cells showed responses to visual stimuli at both three and six weeks after viral injection, while the response latency and selectivity to directions were further improved six weeks post-infection (Figure 3.11C). The cumulative density curve of visually evoked response latencies of the reprogrammed was left-shifted six weeks post-infection compared to the distribution three weeks post-infection (Figure 3.11D). The response latencies of the reprogrammed cells were longer than the healthy control cells at three weeks post-infection, and the difference was reduced at 6 weeks post-infection. The percentage of neurons whose response latencies were less than 3s was up to 89.6% six weeks post-infection, which suggested that most cells showed typical neuronal visual response latency. Furthermore, the distributions of orientation and direction selectivity indices (1-CV, 1-DCV) were both right-shifted six weeks post-infection compared to the distribution three weeks post-infection (Figure 3.11E and F). The orientation and direction selectivity of the reprogrammed cells were lower compared to the healthy control at 3 weeks post-infection. However, the selectivity indices of the reprogrammed cells were higher than the healthy control at 6 weeks post-infection. The percentage of cells that had orientation selectivity index (1-CV) larger than 0.4, indicative of a mature selective neuron, increased from 16.02% at 3 weeks post-infection (n=29 cells, ntotal=181 cells) to 28% at 6 weeks post-infection (n=105 cells, ntotal=375 cells), and the percentage of cells that had direction selectivity index (1-DCV) larger than 0.4 increased from 8.83% at 3 weeks post-infection (n=16 cells, ntotal=181 cells) to 14.93% at 6 weeks post-infection (n=56 cells, ntotal=375 cells). In addition to 2-photon imaging, we used optotagging to examine orientation selectivity of the reprogrammed neurons by injecting AAV-DIO-ChR2-eYFP together with AAV-GFAP::Cre and AAV-FLEX-NeuroD1-mCherry (Figure 3.12A). We identified 22 cells that reliably responded both to optogenetic and visual stimulation and found most of them were selective to orientations (Figure 3.12A-H). Both in vivo 2-photon calcium imaging at two developmental times and optotagging results suggest that the reprogrammed cells acquire orientation- and direction-selective responses over time and indicate their functional integration into the local visual cortical circuits.

Figure 3.11 Two-photon calcium imaging reveals response latency decrease and direction selectivity improvement of the reprogrammed neurons over time. A. Injection scheme for two-photon calcium imaging. ET-1 was first injected to induce a focal stroke. 7 days after ET-1 injection, AAV-GFAP::Cre, AAV-FLEX-NeuroD1-mCherry, and AAV-FLEX-GCaMP6s were injected in the same sites. Reprogrammed cell activities in awake mice were imaged by a two-photon microscope at 3 weeks and 6 weeks after viral injection (at the age of 3-3.5 months old). For the healthy control, AAV-syn-jGCaMP7s was injected into mouse V1, and cell activities were imaged at 3-4 weeks post-injection (at the age of 2.5 months old). B. NeuroD1 and GCaMP6s signals were well overlapped. Well isolated ROIs were chosen for further analysis. Scale bar represents 50 μm. C. Trial-averaged traces of representative cells showed selective responses to 12 directions. Shaded areas represent visual stimulation. D. The cumulative density of visually evoked response latencies of cells at 3 and 6 weeks after viral injection, compared with cells in healthy control mice. Quantification of latencies shown in the inset. N_{3wk}=187 ROIs from 3 mice, N_{3wk}=181 ROIs from 5 mice, N_{6wk}=375 ROIs from 5 mice. 3 week vs. 6 week: p= 0.023; 3 week vs. Healthy: p=0.001; 6 week vs. Healthy: p=0.045, One-way ANOVA followed by Tukey post-hoc tests. E. Cumulative density curves of 1-CV of the reprogrammed cells at 3 and 6 weeks after viral injection. Quantification of 1-CV shown in the inset. 3 week vs. 6 week: p= 0.001; 3 week vs. Healthy: p=0.392; 6 week vs. Healthy: p=0.005, One-way ANOVA followed by Tukey post-hoc tests. F. Same as E but for 1-DCV. Quantification of 1-DCV shown in the inset. 3 week vs. 6 week: p= 0.001; 3 week vs. Healthy: p=0.341; 6 week vs. Healthy: p=0.036, One-way ANOVA followed by Tukey post-hoc tests. *-$p<0.05$, **-$p<0.01$, n.s.-not significant. Data are represented as mean ± SEM.

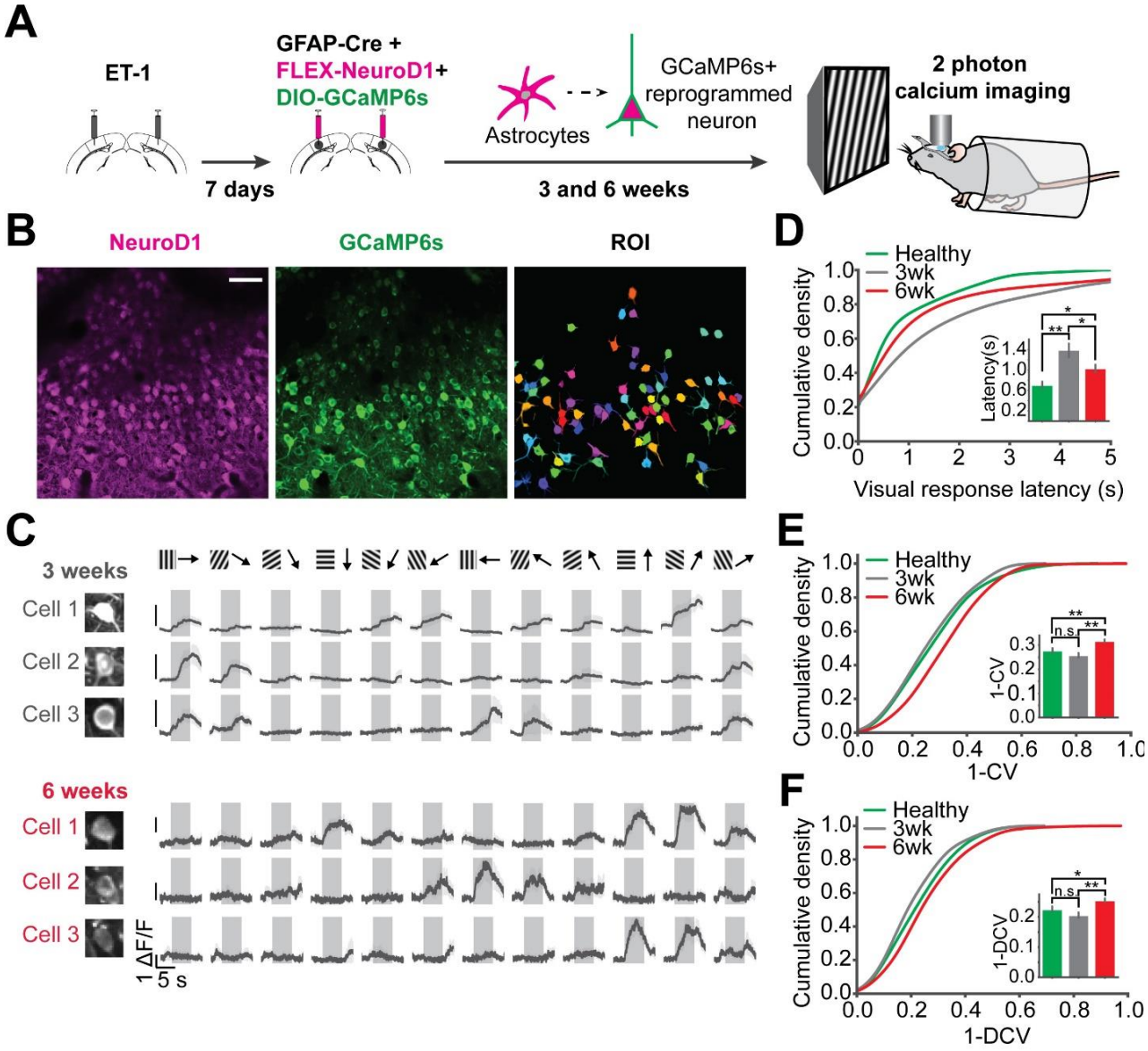
A
ET-1
7 days
GFAP-Cre +
FLEX-NeuroD1+
DIO-GCaMP6s
Astrocytes
GCaMP6s+
reprogrammed
neuron
3 and 6 weeks
2 photon
calcium imaging
B
NeuroD1
GCaMP6s
ROI
C
3 weeks
Cell 1
Cell 2
Cell 3
6 weeks
Cell 1
Cell 2
Cell 3
1 ΔF/F
5 s
D
Healthy
3wk
6wk
Cumulative density
Latency(s)
Visual response latency (s)
E
Healthy
3wk
6wk
Cumulative density
1-CV
n.s
F
Healthy
3wk
6wk
Cumulative density
1-DCV
n.s

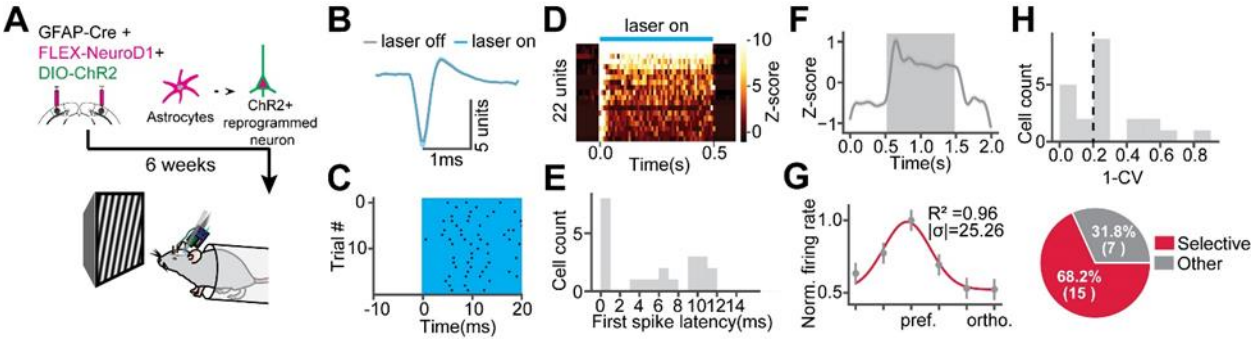

Figure 3.12 Optogenetically tagged reprogrammed cells are visually responsive and orientation selective. A. AAV-DIO-ChR2 was injected together with AAV-GFAP::Cre and AAV-FLEX-NeuroD1 to express ChR2 in the reprogrammed cells. 6 weeks after reprogramming, visual cortical activities were measured by extracellular recordings with optogenetic stimulation. B. Mean template waveforms of a representative unit during laser off and laser on. C. Raster plot of the cell in B during optogenetic stimulation. The cyan shade indicates optogenetic stimulation. D. Firing rate z-scores of units in response to optogenetic stimulation. 22 units that have trial-median first spike latencies shorter than 15ms and mean firing rate z-scores within the optogenetic time window are defined as optotagged units. E. The distribution of first spike latencies of units in D. F. Average firing rate z-scores of optotagged units in response to visual stimulation. The shaded area represents visual stimulus time window. G. Average firing rates of optotagged units in response to 6 orientation are normalized and fitted with a Gaussian function. The inset showing the coefficient of determination (R^2) and sigma of fitted functions. Data are represented as mean ± SEM.

3.5 Discussion

3.5.1 Characterization of neuronal circuit functions is a critical assessment of the therapy

We demonstrated that NeuroD1-mediated in vivo direct reprogramming of astrocytes into neurons promoted their neural circuit integration and led to the visual functional recovery after ischemic injury. Our work bridged the knowledge gap between individual cellular response recovery and animal behavioral recovery, where we characterized the functional synapses formed from specific projections and assessed neuronal response to stimuli in awake mice, which are critical functional characterization at the intermediate neural circuit level. The mouse primary visual cortex is a unique model system providing an opportunity to quantify projection specific functional connectivity and the direct visual responsiveness of the reprogrammed cells. Furthermore, the ability to record responses to different visual features such as orientation and

direction provides a unique ability to quantify how well the cells mature and whether the synapses they receive are functional.

3.5.2 Visual response recovers and selectivity to orientations sharpens following the therapy

In our model system, the visual responses were drastically reduced following ischemic injury, yet they recovered following the NeuroD1 delivery. The putative excitatory neurons started to regain their visual responses three weeks after reprogramming, while the putative inhibitory neurons progressively integrated circuit inputs and refined their activity over a longer period of time. This delayed recovery of inhibition after reprogramming is similar to the absence of matured inhibition at an early age during postnatal V1 development (Minlebaev et al., 2011; Shen and Colonnese, 2016). Furthermore, these visual responses became more specific with time, based on our two-photon calcium imaging and extracellular recording results. The NeuroD1 converted cells gradually developed to be selective to the orientations and directions of visual stimuli, which is a typical feature of the mature visual cortical neurons. Interestingly, the reprogrammed cells at 6 weeks post-infection demonstrated higher selectivity compared to the healthy controls, which could be potentially explained by the more functionally developed synaptic inputs received by the reprogrammed cells compared to the healthy controls.

3.5.3 Local functional circuits undergo refinement of synaptic inputs

At the same time, using the functional circuit mapping technique, we gained more insights into synaptic input integration during the recovery process. We observed initial functional synapse formation and even hyper-connectivity in newly reprogrammed neurons three weeks after viral injection. Initially, the reprogrammed neurons received almost twice as many synapses compared to the healthy control cells. The excessive synapse numbers decreased six weeks after reprogramming. These functional synapses represented appropriate and not aberrant synapses, characteristic for the primary visual cortex circuitry. As the reprogrammed cells assume neuronal fate and undergo synaptogenesis, more inputs drive the cell activity, leading to the pruning of excess synapses, activity refinement, and cell maturation. This process also coincides with the maturation of inhibition seen in our in vivo work. Strikingly, surviving neurons also regained synaptic connections, suggesting that removing the glial scar might help rewire the damaged brain

area (Zhang et al., 2018). This finding suggests that structural and functional synaptic plasticity may be present in the newly reprogrammed neurons, resembling neonatal neuronal development processes (Chechik et al., 1999).

3.5.4 Visual experience might play a role in activity refinement following the therapy

Visual experience in the housing cages may have led to the pruning of excess synapses, activity refinement, and cell maturation. Slower development of inhibitory responses is consistent with the delayed maturation of inhibition following visual experience in the normal developing cortex. Improved orientation selectivity of the reprogrammed neurons with additional time and visual experience may result from their integration into the local circuits and maturation of the local inhibition (Liu et al., 2011).

In our work, the demonstration of visual response and selectivity recovery provides a novel cellular and circuit characterization consistent with the previous work (Chen et al., 2020). CRACM experiments provided the quantification of the functional synaptic connectivity recovery extending the prior report of non-specific spontaneous synaptic currents developing in reprogrammed cells (Guo et al., 2014; Chen et al., 2020). We discovered, for the first time to our knowledge, that the functional maturation of the reprogrammed neurons shares similarities with the typical postnatal cortical circuit development. This finding suggests the importance of experience in the development of the reprogrammed cells and functional brain recovery after injury.

3.5.5 Conversion efficiency and functional recovery are similar to other therapies

Compared to other studies, the functional recovery achieved by NeuroD1-mediated astrocyte-to-neuron conversion in vivo was similarly efficient. The reprogrammed neurons in the visual cortex acquired the cortical layer structure, similarly to Ngn2- and Nurr1-mediated reprogramming (Mattugini et al., 2019). The local functional circuit and visual response recovery were also similar to embryonic neuronal transplantation results (Falkner et al., 2016). However, other methods such as cell transplantation may have side effects, such as immune response, which limit their therapeutic potential. Direct in vivo conversion of astrocytes into neurons removes the possibility of graft rejection and provides a viable solution for this problem.

Our findings suggest that the NeuroD1-based in vivo direct reprogramming technology may be a promising gene therapy treatment of brain injury by replenishing the lost neurons and successfully integrating them into the existing neural circuit.

3.6 Author contributions

Q.W., Y.T., M.G., G.C., and A.A.C. designed experiments. Z.P. produced viruses. Y.T., Q.W., Y.C., A.K.R., W.L., Z.X., and T.W. performed the IHC experiments. Y.T. and S.T.K. performed extracellular recordings. Q.W. performed the CRACM experiments. M.G. performed 2 photon calcium imaging. Y.T., Q.W., and E.R. performed injections. Y.T., Q.W., M.G., W.L., Z.X., and T.W. analyzed data, Y.T., Q.W., M.G., W.L., Z.X., and T.W. drafted the manuscript, Y.T., Q.W., M.G., G.C., and A.A.C edited and revised the manuscript.

3.7 References

Arenkiel, B.R., Peca, J., Davison, I.G., Feliciano, C., Deisseroth, K., Augustine, G.J., Ehlers, M.D., and Feng, G. (2007). In vivo light-induced activation of neural circuitry in transgenic mice expressing channelrhodopsin-2. *Neuron* 54**,** 205-218.

Avants, B.W., Murphy, D.B., Dapello, J.A., and Robinson, J.T. (2015). NeuroPG: open source software for optical pattern generation and data acquisition. *Front Neuroeng* 8**,** 1.

Benner, E.J., Luciano, D., Jo, R., Abdi, K., Paez-Gonzalez, P., Sheng, H., Warner, D.S., Liu, C., Eroglu, C., and Kuo, C.T. (2013). Protective astrogenesis from the SVZ niche after injury is controlled by Notch modulator Thbs4. *Nature* 497**,** 369-373.

Blanchard, J.W., Eade, K.T., Szűcs, A., Lo Sardo, V., Tsunemoto, R.K., Williams, D., Sanna, P.P., and Baldwin, K.K. (2014). Selective conversion of fibroblasts into peripheral sensory neurons. *Nature Neuroscience* 18**,** 25.

Brulet, R., Matsuda, T., Zhang, L., Miranda, C., Giacca, M., Kaspar, B.K., Nakashima, K., and Hsieh, J. (2017). NEUROD1 Instructs Neuronal Conversion in Non-Reactive Astrocytes. *Stem Cell Reports* 8**,** 1506-1515.

Chechik, G., Meilijson, I., and Ruppin, E. (1999). Neuronal Regulation: A Mechanism for Synaptic Pruning During Brain Maturation. *Neural Computation* 11**,** 2061-2080.

Chen, G., Wernig, M., Berninger, B., Nakafuku, M., Parmar, M., and Zhang, C.L. (2015). In Vivo Reprogramming for Brain and Spinal Cord Repair. *eNeuro* 2.

Chen, T.W., Wardill, T.J., Sun, Y., Pulver, S.R., Renninger, S.L., Baohan, A., Schreiter, E.R., Kerr, R.A., Orger, M.B., Jayaraman, V., Looger, L.L., Svoboda, K., and Kim, D.S. (2013). Ultrasensitive fluorescent proteins for imaging neuronal activity. *Nature* 499**,** 295-300.

Chen, Y.C., Ma, N.X., Pei, Z.F., Wu, Z., Do-Monte, F.H., Keefe, S., Yellin, E., Chen, M.S., Yin, J.C., Lee, G., Minier-Toribio, A., Hu, Y., Bai, Y.T., Lee, K., Quirk, G.J., and Chen, G. (2020). A NeuroD1 AAV-Based Gene Therapy for Functional Brain Repair after Ischemic Injury through In Vivo Astrocyte-to-Neuron Conversion. *Mol Ther* 28**,** 217-234.

Connors, B.W., and Gutnick, M.J. (1990). Intrinsic firing patterns of diverse neocortical neurons. *Trends Neurosci* 13**,** 99-104.

Erdo, F., Buhrle, C., Blunk, J., Hoehn, M., Xia, Y., Fleischmann, B., Focking, M., Kustermann, E., Kolossov, E., Hescheler, J., Hossmann, K.A., and Trapp, T. (2003). Host-dependent tumorigenesis of embryonic stem cell transplantation in experimental stroke. *J Cereb Blood Flow Metab* 23**,** 780-785.

Faiz, M., Sachewsky, N., Gascon, S., Bang, K.W., Morshead, C.M., and Nagy, A. (2015). Adult Neural Stem Cells from the Subventricular Zone Give Rise to Reactive Astrocytes in the Cortex after Stroke. *Cell Stem Cell* 17**,** 624-634.

Falkner, S., Grade, S., Dimou, L., Conzelmann, K.K., Bonhoeffer, T., Gotz, M., and Hubener, M. (2016). Transplanted embryonic neurons integrate into adult neocortical circuits. *Nature* 539**,** 248-253.

Fitch, M.T., and Silver, J. (2008). CNS injury, glial scars, and inflammation: Inhibitory extracellular matrices and regeneration failure. *Exp Neurol* 209**,** 294-301.

Ge, L.J., Yang, F.H., Li, W., Wang, T., Lin, Y., Feng, J., Chen, N.H., Jiang, M., Wang, J.H., Hu, X.T., and Chen, G. (2020). In vivo Neuroregeneration to Treat Ischemic Stroke Through NeuroD1 AAV-Based Gene Therapy in Adult Non-human Primates. *Front Cell Dev Biol* 8**,** 590008.

Grande, A., Sumiyoshi, K., Lopez-Juarez, A., Howard, J., Sakthivel, B., Aronow, B., Campbell, K., and Nakafuku, M. (2013). Environmental impact on direct neuronal reprogramming in vivo in the adult brain. *Nat Commun* 4**,** 2373.

Guo, Z., Zhang, L., Wu, Z., Chen, Y., Wang, F., and Chen, G. (2014). In vivo direct reprogramming of reactive glial cells into functional neurons after brain injury and in an Alzheimer's disease model. *Cell Stem Cell* 14**,** 188-202.

Heinrich, C., Bergami, M., Gascon, S., Lepier, A., Vigano, F., Dimou, L., Sutor, B., Berninger, B., and Gotz, M. (2014). Sox2-mediated conversion of NG2 glia into induced neurons in the injured adult cerebral cortex. *Stem Cell Reports* 3**,** 1000-1014.

Henze, D.A., Borhegyi, Z., Csicsvari, J., Mamiya, A., Harris, K.D., and Buzsaki, G. (2000). Intracellular features predicted by extracellular recordings in the hippocampus in vivo. *J Neurophysiol* 84**,** 390-400.

Johnston, S.C., Fayad, P.B., Gorelick, P.B., Hanley, D.F., Shwayder, P., Van Husen, D., and Weiskopf, T. (2003). Prevalence and knowledge of transient ischemic attack among US adults. *Neurology* 60**,** 1429-1434.

Kawano, H., Kimura-Kuroda, J., Komuta, Y., Yoshioka, N., Li, H.P., Kawamura, K., Li, Y., and Raisman, G. (2012). Role of the lesion scar in the response to damage and repair of the central nervous system. *Cell Tissue Res* 349**,** 169-180.

Ko, H., Hofer, S.B., Pichler, B., Buchanan, K.A., Sjostrom, P.J., and Mrsic-Flogel, T.D. (2011). Functional specificity of local synaptic connections in neocortical networks. *Nature* 473**,** 87-91.

Li, H., and Chen, G. (2016). In Vivo Reprogramming for CNS Repair: Regenerating Neurons from Endogenous Glial Cells. *Neuron* 91**,** 728-738.

Li, Y., Van Hooser, S.D., Mazurek, M., White, L.E., and Fitzpatrick, D. (2008). Experience with moving visual stimuli drives the early development of cortical direction selectivity. *Nature* 456**,** 952-956.

Liu, B.H., Li, Y.T., Ma, W.P., Pan, C.J., Zhang, L.I., and Tao, H.W. (2011). Broad inhibition sharpens orientation selectivity by expanding input dynamic range in mouse simple cells. *Neuron* 71**,** 542-554.

Marei, H.E., Hasan, A., Rizzi, R., Althani, A., Afifi, N., Cenciarelli, C., Caceci, T., and Shuaib, A. (2018). Potential of Stem Cell-Based Therapy for Ischemic Stroke. *Front Neurol* 9**,** 34.

Marro, S., Pang, Z.P., Yang, N., Tsai, M.C., Qu, K., Chang, H.Y., Sudhof, T.C., and Wernig, M. (2011). Direct lineage conversion of terminally differentiated hepatocytes to functional neurons. *Cell Stem Cell* 9**,** 374-382.

Mattugini, N., Bocchi, R., Scheuss, V., Russo, G.L., Torper, O., Lao, C.L., and Gotz, M. (2019). Inducing Different Neuronal Subtypes from Astrocytes in the Injured Mouse Cerebral Cortex. *Neuron* 103**,** 1086-1095 e1085.

Mazurek, M., Kager, M., and Van Hooser, S.D. (2014). Robust quantification of orientation selectivity and direction selectivity. *Front Neural Circuits* 8**,** 92.

Michelsen, K.A., Acosta-Verdugo, S., Benoit-Marand, M., Espuny-Camacho, I., Gaspard, N., Saha, B., Gaillard, A., and Vanderhaeghen, P. (2015). Area-specific reestablishment of damaged circuits in the adult cerebral cortex by cortical neurons derived from mouse embryonic stem cells. *Neuron* 85**,** 982-997.

Minlebaev, M., Colonnese, M., Tsintsadze, T., Sirota, A., and Khazipov, R. (2011). Early gamma oscillations synchronize developing thalamus and cortex. *Science* 334**,** 226-229.

Nauhaus, I., Benucci, A., Carandini, M., and Ringach, D.L. (2008). Neuronal selectivity and local map structure in visual cortex. *Neuron* 57**,** 673-679.

Niu, W., Zang, T., Zou, Y., Fang, S., Smith, D.K., Bachoo, R., and Zhang, C.L. (2013). In vivo reprogramming of astrocytes to neuroblasts in the adult brain. *Nat Cell Biol* 15**,** 1164-1175.

Nolbrant, S., Giacomoni, J., Hoban, D.B., Bruzelius, A., Birtele, M., Chandler-Militello, D., Pereira, M., Ottosson, D.R., Goldman, S.A., and Parmar, M. (2020). Direct Reprogramming of Human Fetal- and Stem Cell-Derived Glial Progenitor Cells into Midbrain Dopaminergic Neurons. *Stem Cell Reports* 15**,** 869-882.

Ovbiagele, B., and Nguyen-Huynh, M.N. (2011). Stroke epidemiology: advancing our understanding of disease mechanism and therapy. *Neurotherapeutics : the journal of the American Society for Experimental NeuroTherapeutics* 8**,** 319-329.

Pachitariu, M., Steinmetz, N., Kadir, S., Carandini, M., and Harris, K.D. (2016a). Kilosort: realtime spike-sorting for extracellular electrophysiology with hundreds of channels. *bioRxiv***,** 061481.

Pachitariu, M., Stringer, C., Schröder, S., Dipoppa, M., Rossi, L.F., Carandini, M., and Harris, K.D. (2016b). Suite2p: beyond 10,000 neurons with standard two-photon microscopy. *bioRxiv***,** 061507.

Peirce, J.W. (2007). PsychoPy--Psychophysics software in Python. *J Neurosci Methods* 162**,** 8-13.

Petreanu, L., Huber, D., Sobczyk, A., and Svoboda, K. (2007). Channelrhodopsin-2-assisted circuit mapping of long-range callosal projections. *Nat Neurosci* 10**,** 663-668.

Rossant, C., Kadir, S.N., Goodman, D.F.M., Schulman, J., Hunter, M.L.D., Saleem, A.B., Grosmark, A., Belluscio, M., Denfield, G.H., Ecker, A.S., Tolias, A.S., Solomon, S., Buzsaki, G., Carandini, M., and Harris, K.D. (2016). Spike sorting for large, dense electrode arrays. *Nat Neurosci* 19**,** 634-641.

Shen, J., and Colonnese, M.T. (2016). Development of Activity in the Mouse Visual Cortex. *J Neurosci* 36**,** 12259-12275.

Shobe, J.L., Claar, L.D., Parhami, S., Bakhurin, K.I., and Masmanidis, S.C. (2015). Brain activity mapping at multiple scales with silicon microprobes containing 1,024 electrodes. *J Neurophysiol* 114**,** 2043-2052.

Siegle, J.H., Lopez, A.C., Patel, Y.A., Abramov, K., Ohayon, S., and Voigts, J. (2017). Open Ephys: an open-source, plugin-based platform for multichannel electrophysiology. *J Neural Eng* 14**,** 045003.

Somaa, F.A., Wang, T.Y., Niclis, J.C., Bruggeman, K.F., Kauhausen, J.A., Guo, H., Mcdougall, S., Williams, R.J., Nisbet, D.R., Thompson, L.H., and Parish, C.L. (2017). Peptide-Based Scaffolds Support Human Cortical Progenitor Graft Integration to Reduce Atrophy and Promote Functional Repair in a Model of Stroke. *Cell Rep* 20**,** 1964-1977.

Stark, E., Eichler, R., Roux, L., Fujisawa, S., Rotstein, H.G., and Buzsaki, G. (2013). Inhibition-induced theta resonance in cortical circuits. *Neuron* 80**,** 1263-1276.

Ting, J.T., Lee, B.R., Chong, P., Soler-Llavina, G., Cobbs, C., Koch, C., Zeng, H., and Lein, E. (2018). Preparation of Acute Brain Slices Using an Optimized N-Methyl-D-glucamine Protective Recovery Method. *Journal of visualized experiments : JoVE***,** 53825.

Tornero, D., Wattananit, S., Gronning Madsen, M., Koch, P., Wood, J., Tatarishvili, J., Mine, Y., Ge, R., Monni, E., Devaraju, K., Hevner, R.F., Brustle, O., Lindvall, O., and Kokaia, Z. (2013). Human induced pluripotent stem cell-derived cortical neurons integrate in stroke-injured cortex and improve functional recovery. *Brain* 136**,** 3561-3577.

Torper, O., Ottosson, D.R., Pereira, M., Lau, S., Cardoso, T., Grealish, S., and Parmar, M. (2015). In Vivo Reprogramming of Striatal NG2 Glia into Functional Neurons that Integrate into Local Host Circuitry. *Cell Rep* 12**,** 474-481.

Trainito, C., Von Nicolai, C., Miller, E.K., and Siegel, M. (2019). Extracellular Spike Waveform Dissociates Four Functionally Distinct Cell Classes in Primate Cortex. *Curr Biol* 29**,** 2973-2982 e2975.

Vallat, R. (2018). Pingouin: statistics in Python. *The Journal of Open Source Software* 3**,** 1026.

Xiang, Z., Xu, L., Liu, M., Wang, Q., Li, W., Lei, W., and Chen, G. (2021). Lineage tracing of direct astrocyte-to-neuron conversion in the mouse cortex. *Neural Regen Res* 16**,** 750-756.

Yamawaki, N., and Shepherd, G.M. (2015). Synaptic circuit organization of motor corticothalamic neurons. *J Neurosci* 35**,** 2293-2307.

Yang, N., Ng, Y.H., Pang, Z.P., Südhof, T.C., and Wernig, M. (2011). Induced neuronal cells: how to make and define a neuron. *Cell stem cell* 9**,** 517-525.

Zhang, L., Lei, Z., Guo, Z., Pei, Z., Chen, Y., Zhang, F., Cai, A., Mok, Y.K., Lee, G., Swaminnathan, V., Wang, F., Bai, Y., and Chen, G. (2018). Reversing Glial Scar Back To Neural Tissue Through NeuroD1-Mediated Astrocyte-To-Neuron Conversion. *bioRxiv***,** 261438.

Zhang, Y., Pak, C., Han, Y., Ahlenius, H., Zhang, Z., Chanda, S., Marro, S., Patzke, C., Acuna, C., Covy, J., Xu, W., Yang, N., Danko, T., Chen, L., Wernig, M., and Sudhof, T.C. (2013). Rapid single-step induction of functional neurons from human pluripotent stem cells. *Neuron* 78**,** 785-798.

CHAPTER 4. PRELIMINARY DATA AND FUTURE DIRECTIONS

4.1 Visual familiarity in freely moving mice

We have demonstrated that visual familiarity induces 5 Hz oscillation in mouse V1. The inhibition recruited by the oscillations sharpens the orientation and direction selectivity of V1 neurons (Kissinger et al., 2018; Kissinger et al., 2020; Gao et al., 2021). To investigate the behavioral relevance of the experience-dependent selectivity improvement, we performed in vivo calcium imaging in freely moving mice with simultaneous behavior tracking. The following sections are the preliminary results we have acquired.

4.1.1 Methods

The adult wild-type mice were injected with AAV-syn-jGCaMP7s at a depth of 200 μm to express jGCaMP7s in the superficial layer neurons of V1. Cranial window surgeries and glass window implantation were performed 3 weeks after the injection. Aluminum adapters that fix the Miniscope on the top of the cranial window were installed on the head of the mice with dental cement. The mice were placed in a behavior chamber equipped with a monitor that displayed visual stimuli and an infrared behavior tracking camera. The mice were habituated in the chamber with the miniscope for 4 days before recording.

The imaging data were analyzed in python with an imaging analysis pipeline provided by the open-source package CaImAn, including motion correction, correlation, and signal to noise ratio thresholding, and constrained nonnegative matrix factorization (Zhou et al., 2018). The deconvolution was performed with OASIS method (Friedrich et al., 2017). Mouse position tracking was done in DeepLabCut with a ResNet model with resnet50 architecture. The head rotations were tracked by an integrated motion sensor in Miniscope.

4.1.2 Four groups of neurons that have distinct visually evoked response patterns were revealed by unsupervised machine learning.

Mice expressing jGCaMP7s in layer 2/3 neurons were imaged in a behavior chamber. We acquired simultaneous recordings of the movement, rotation, and neuronal activity. (Figure 4.1) We determined if the mice were facing the stimulus with the motion tracking data. We only used the trials in that the mice were facing the stimulus for the analysis of visual response. The cells that did not have activity changes at the onset of the visual stimulus were disregarded.

To separate the visually evoked activity and analyze the different excited and inhibited activity patterns, we performed k-mean clustering on the normalized trial averaged calcium traces. The activity of cells was separated into four groups that had distinct patterns (Figure 4.2). The four groups consist of a group that was persistently excited, a group that was first inhibited at the onset and later excited, a relatively mildly inhibited group, and a strongly inhibited group that almost did not have any calcium peaks during the stimuli (Figure 4.2 B and C). Such groups are consistent across the stimuli and the course of the visual experience.

4.1.3 Visually evoked activity shift towards inhibited response was stimulus-specific.

On the first day of recording (Day 0), the mice were recorded with two band-pass filtered pink noise visual stimuli (Figure 4.3A). The spatial frequency of stimulus A was 0.12 cycle/degree, and stimulus B was 0.03 cycle/degree. Both stimuli were temporally modulated. The mice were then experienced with stimulus A (200 repeats/day) for four days. The recordings were also acquired over the four days. The visual responses to both stimulus A and B were acquired again on day 5. The visual responses of neurons were normalized to a scale from -1 to 1, where 0 represented the baseline activity; 1 represented the maximum activity of the neuron; -1 represented the minimum activity of the neuron (Figure 4.3B-E). Before the visual experience, the proportion of cells that were excited by stimulus A was almost equal to the proportion of the cells that were inhibited. After the mice were familiarized with stimulus A, the population responded to stimulus A shifted towards inhibited response (Figure 4.3B and D). Meanwhile, the distribution of the neuronal responses to the non-familiarized visual stimulus B remained largely the same before and after the visual experience (Figure 4.3C and E), suggesting the experience-induced activity shift towards inhibition is specific to the spatial frequency of the stimulus.

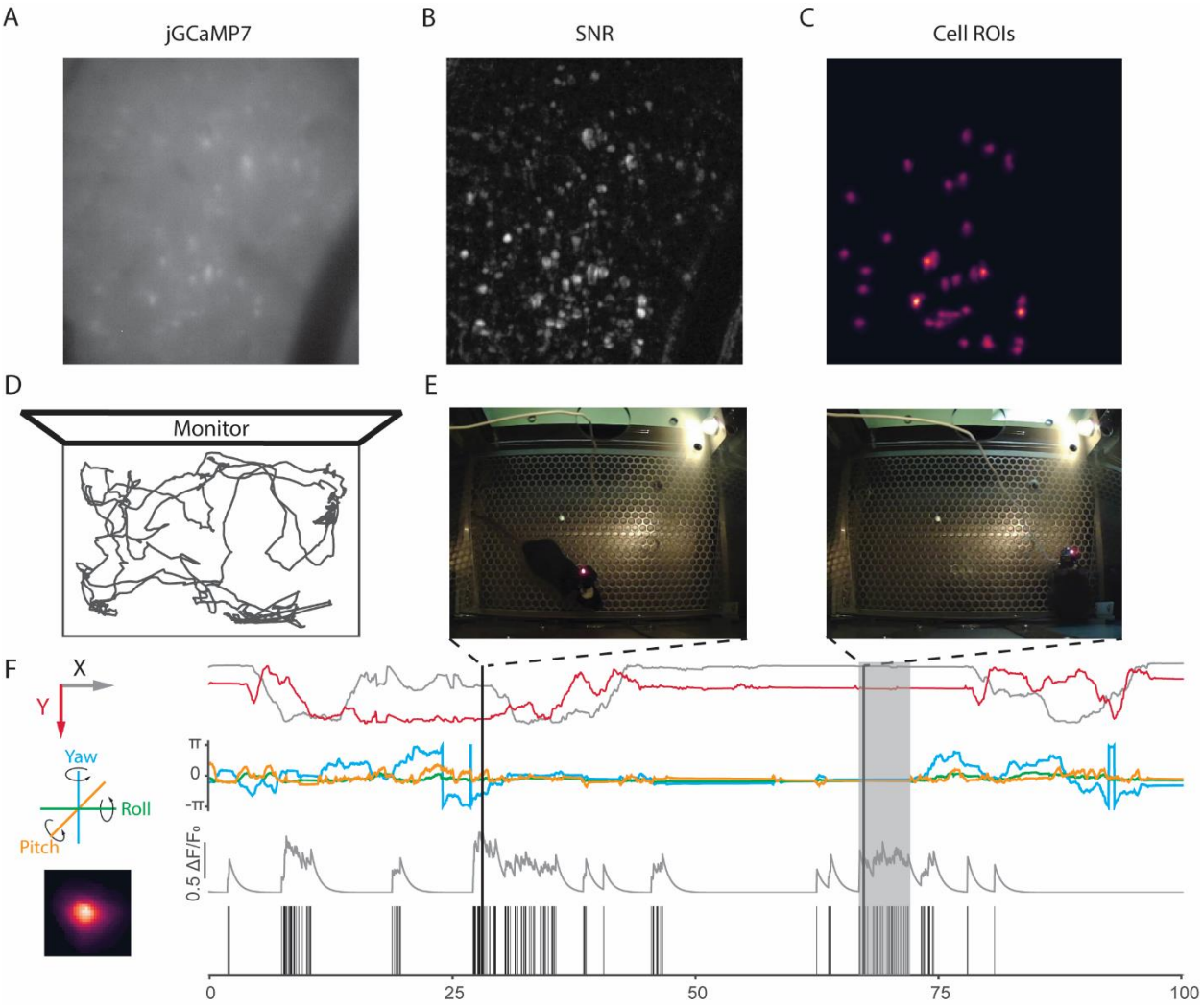

Figure 4.1 Layer 2/3 neurons calcium imaging with behavior tracking. A. A frame of a raw image acquired from a mouse expressing jGCaMP7. B. The peak signal to noise ratio (SNR) map of the image plane. C. The ROIs of cells generated by thresholding with the SNP and correlation map. D. The moving track of a mouse in the behavior chamber. E. Screenshots of a mouse facing and not facing the monitor. The white light was turned on to acquire the colored images. Behavior tracking was done with an infrared light source and camera. F. An example of the simultaneous recordings. Top, mouse location; middle, 3-D rotations of the head of the mouse; bottom, the ΔF/F0 calcium trace and the discretized calcium spike of a cell.

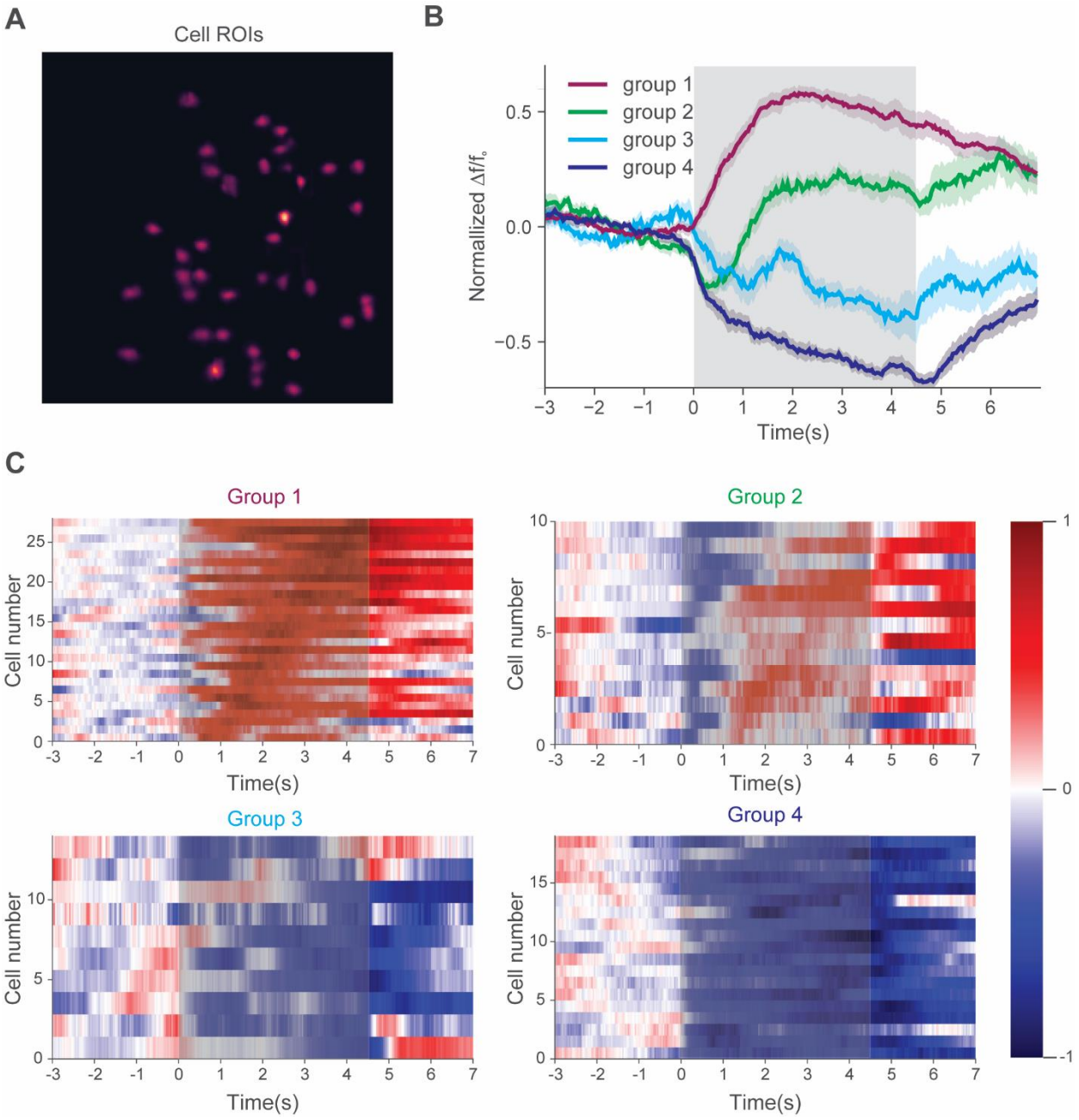

Figure 4.2 Four types of visually evoked responses were observed in L2/3. A. The average image of the cell bodies in a plane. The activity from cells in this plane is shown as an example here. B. The average normalized responses of four groups of neurons. The grey rectangle represents the duration of the visual stimulus. Average traces are represented as mean ± SEM. C. The trial averaged the response of the four groups of cells. Color represents the normalized ΔF/F0

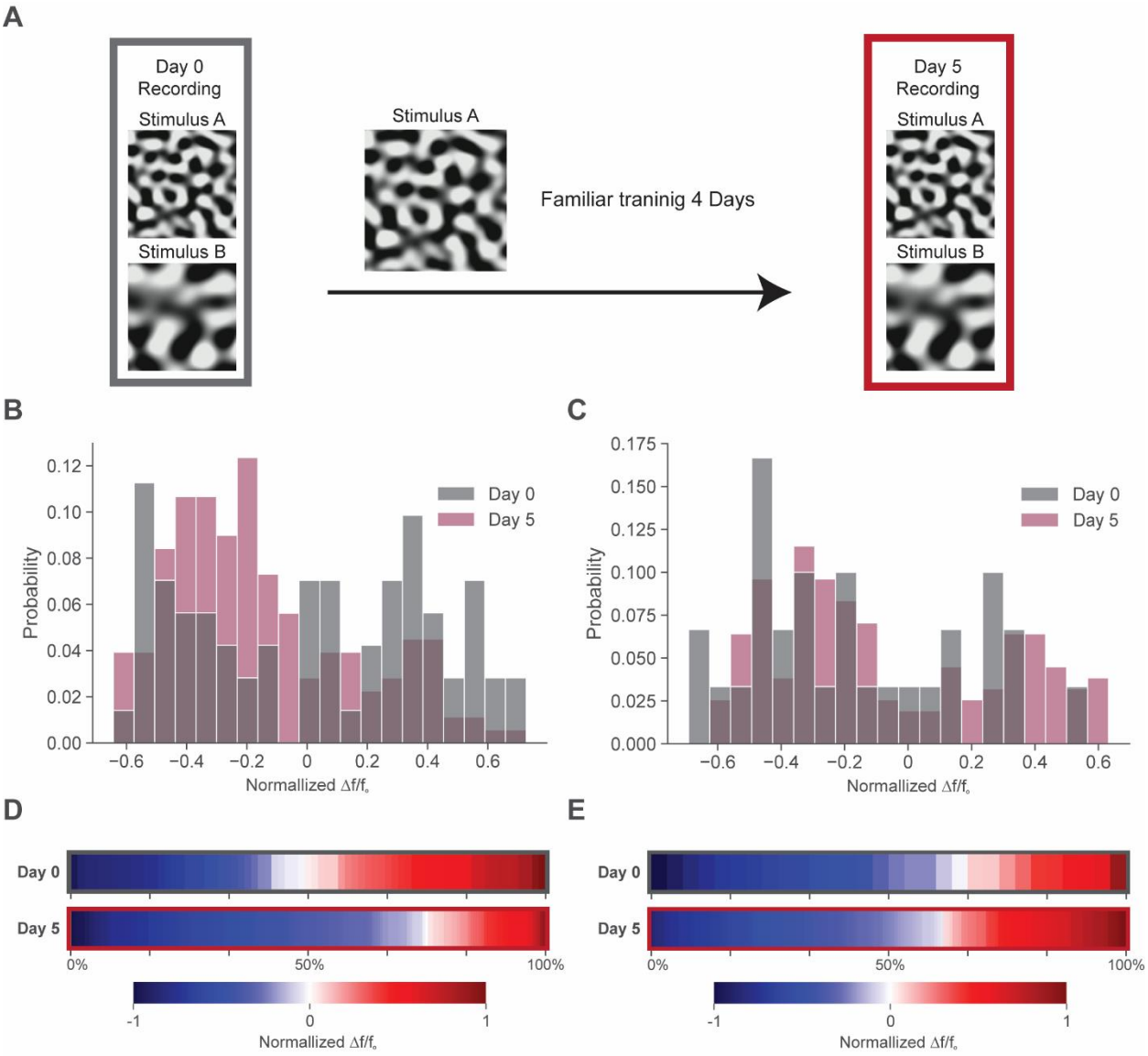

Figure 4.3 The population shift of visual responses after the visual experience. A. The schematic of the experiments. B. The distribution of the normalized visual response to stimulus A before (grey, days 0) and after (crimson, day 5) visual experience. C. Same as B, but for the unfamiliar stimulus B. D. The averaged activity during stimulus A before and after the experience. E. Same as D, but for stimulus B.

4.1.4 The visual responses of cell groups that have the same response pattern are unchanged

The shift we observed could solely result from the neurons switching their response pattern to another one, or a change in the magnitude of the response of neurons that are in certain groups could also happen at the same time. To address this possibility, we compared the averaged response of the neurons with the same response patterns (Figure 4.4). No statistically significant change was observed in any combinations of stimuli and visual experience.

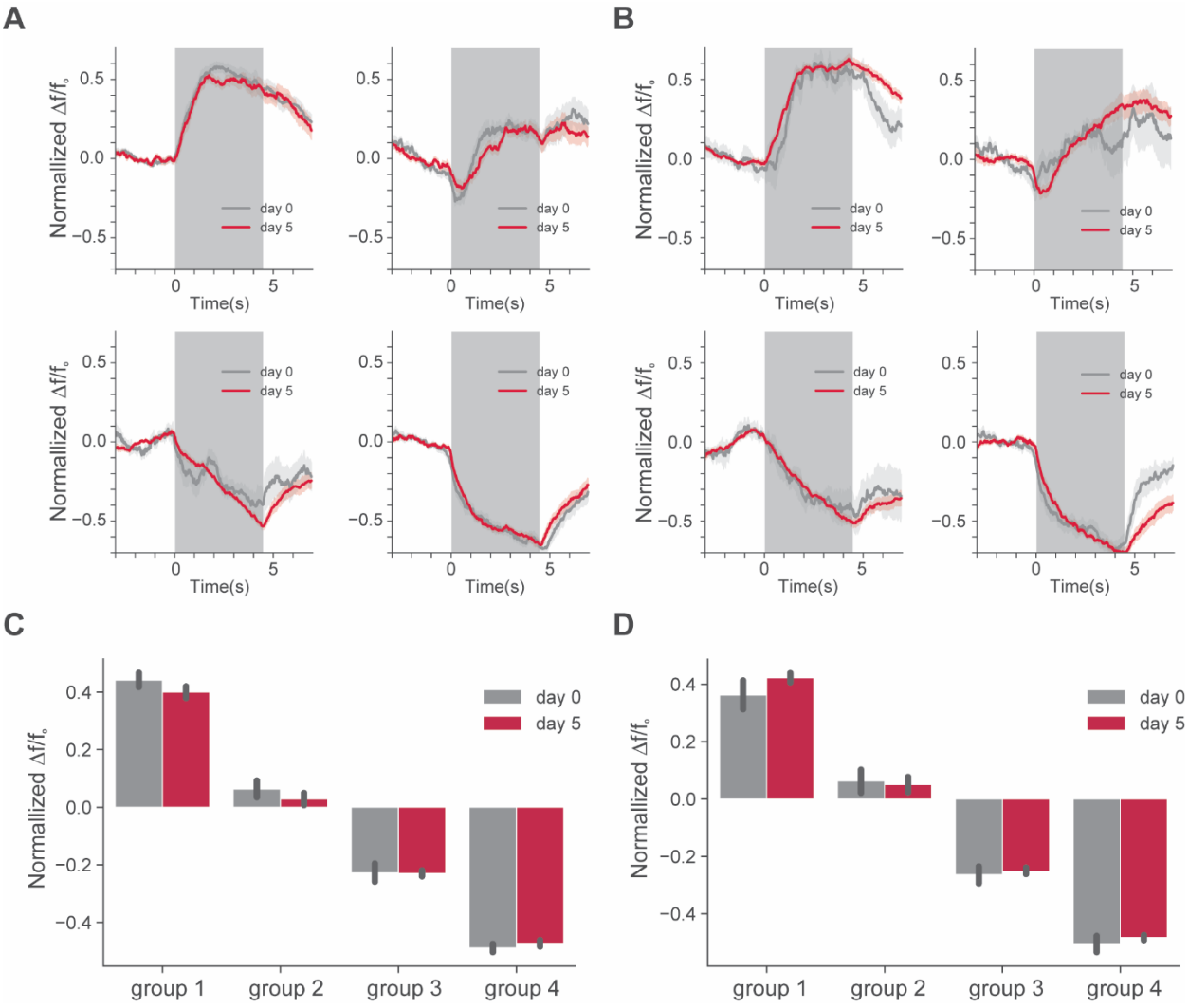

Figure 4.4 The visual responses of the four groups of neurons before and after the visual experience. A. The normalized average responses of the four groups to stimulus A. B. Same as A, but for the response to stimulus B. C. the averaged ΔF/F0 of four groups during stimulus A presentation. D. Same as C, but for stimulus B. Data were presented with mean ± SEM

4.2 Future direction

Our results suggest that the recruitment of the inhibition by a familiar visual stimulus led to a change in the response pattern. However, direct evidence of the occurrence of such an event is still needed. The imaging of the same neurons over days and comparing their activity between recording sessions would provide such evidence. We recorded the activities of layer 2/3 neurons during all visual familiarization sessions. The same neuron tracking from these recordings should provide us with the information that can either prove or disprove our hypothesis.

Another important future development is how the experience-induced changes are involved in the learning associated behavior tasks. We have already successfully achieved simultaneous recording and behavior tracking in the open field chamber. It is feasible to perform imaging within the context of visually cued reward-associated behavior tasks.

4.3 References

Friedrich J, Zhou P, Paninski L (2017) Fast online deconvolution of calcium imaging data. PLoS Comput Biol 13:e1005423.

Gao M, Lim S, Chubykin AA (2021) Visual Familiarity Induced 5-Hz Oscillations and Improved Orientation and Direction Selectivities in V1. J Neurosci 41:2656-2667.

Kissinger ST, Pak A, Tang Y, Masmanidis SC, Chubykin AA (2018) Oscillatory Encoding of Visual Stimulus Familiarity. J Neurosci 38:6223-6240.

Kissinger ST, Wu Q, Quinn CJ, Anderson AK, Pak A, Chubykin AA (2020) Visual Experience-Dependent Oscillations and Underlying Circuit Connectivity Changes Are Impaired in Fmr1 KO Mice. Cell Rep 31:107486.

Zhou P, Resendez SL, Rodriguez-Romaguera J, Jimenez JC, Neufeld SQ, Giovannucci A, Friedrich J, Pnevmatikakis EA, Stuber GD, Hen R, Kheirbek MA, Sabatini BL, Kass RE, Paninski L (2018) Efficient and accurate extraction of in vivo calcium signals from microendoscopic video data. Elife 7.

PUBLICATIONS

Mang Gao, Sukbin Lim and Alexander A. Chubykin. Visual Familiarity Induced 5-Hz Oscillations and Improved Orientation and Direction Selectivities in V1. *Journal of Neuroscience*. March 24, 2021, 41 (12) 2656-2667.

Y Tang*, Q Wu*, **M Gao***, E Ryu, Z Pei, ST Kissinger, Y Chen, A Rao, G Chen, AA Chubykin. Restoration of visual cortical connectivity and function after ischemic injury through NeuroD1-mediated gene therapy. *Frontiers in Cell and Developmental Biology*. August 18, 2021 *Co-first authors.